MEASUREMENT OF MULTIJET CROSS-SECTION RATIOS IN PROTON-PROTON COLLISIONS WITH THE CMS DETECTOR AT THE LHC

A THESIS

Submitted to the

FACULTY OF SCIENCE

PANJAB UNIVERSITY, CHANDIGARH

for the degree of

DOCTOR OF PHILOSOPHY

2018

Anterpreet Kaur

DEPARTMENT OF PHYSICS

CENTRE OF ADVANCED STUDY IN PHYSICS

PANJAB UNIVERSITY, CHANDIGARH

INDIA

Dedicated to

my Parents

Acknowledgement

I would like to take this opportunity to thank the many people who helped make this dissertation possible.

In the first and foremost place, I gratefully express my sincere gratitude to my supervisor Prof.(Mrs.) Manjit Kaur for her invaluable assistance, support, guidance and blessings. She inspired me greatly to work in this project. Her willingness to motivate me contributed tremendously to this project.

I am highly obliged to Prof. C.S. Aulakh Chairperson of the Department of Physics, Panjab University, Chandigarh, for his helping hand in providing a good environment and adequate facilities to complete this project successfully.

I feel deeply indebted to my parents for their unconditional love, understanding, support, strength, blessings and for everything.

I am greatly thankful to my wellwishers, my friends Anu, Sohail, Junaid, Mandeep and my classmates for all that they meant to me during the crucial times of the completion of my project.

I owe my very special thanks to Mr. Inderpal Singh, Mrs. Prabhdeep Kaur, Mrs. Manuk Z. Mehta, Ms. Ritu Aggarwal, Ms. Ruchi Gupta, Ms. Monika Mittal and Ms. Genius, the members of high energy physics Laboratory, Dept. of Physics, P.U. for helping me out from all kinds of problems with their constant support, suggestions and encouragement.

Finally and the most importantly, I would like to pay my greatest regards to the Almighty God for His blessings and kindness, a boundless and an endless source of inspiration for me always.

November 15, 2012 *(Anterpreet Kaur)*

Abstract

The collisions of hadrons at very high centre-of-mass energies provide a direct probe to the nature of the underlying parton-parton scattering physics. The scattering of the elementary quark and gluon constituents of the incoming hadron beams produces a high momentum partons which then fragment to spray of particles clustered in the form of jets. These jets are the final structures observed in the detector and they preserve the energy and direction of the initial partons. Hence jets can serve as a direct test of theory of strong interactions called Quantum Chromodynamics. The inclusive multijet production cross-section is an important observable which provides the details of parton distribution functions (PDF) of the colliding hadrons and the precise measurement of the strong coupling constant α_S. Instead of individual cross-sections, the cross-section ratio is a better tool to determine the value of α_S as many theoretical and experimental uncertainties cancel in the ratio.

A measurement of inclusive multijet event cross-sections and the cross-section ratio is presented using data from proton-proton collisions collected with the CMS detector at a centre-of-mass energy of 8 TeV corresponding to an integrated luminosity of 19.7 fb^{-1}. Jets are reconstructed with the anti-k$_t$ clustering algorithm for a jet size parameter R = 0.7. The inclusive 2-jet and 3-jet event cross-sections as well as the ratio of the 3-jet over 2-jet event cross-section R_{32} are measured as a function of the average transverse momenta p_{T} of the two leading jets in a phase space region ranging up to jet p_{T} of 2.0 TeV and an absolute rapidity of $|y| = 2.5$. The measurements after correcting for detector effects are well described by predictions at next-to-leading order in perturbative quantum chromodynamics and additionally are compared to several Monte Carlo event generators. The strong coupling constant at the scale of the Z boson mass is extracted from a fit of the measured R_{32} which gives $\alpha_s(M_Z) = 0.1150 \pm 0.0010\,(\mathrm{exp}) \pm 0.0013\,(\mathrm{PDF}) \pm 0.0015\,(\mathrm{NP})\,^{+0.0050}_{-0.0000}\,(\mathrm{scale})$ using MSTW2008 PDF set. The current measurement agrees well with the world average value of $\alpha_s(M_Z) = 0.1181 \pm 0.0011$ as well as previous measurements.

Contents

Chapter 1

Introduction

Particle physics deals with the study of the basic constituents of matter and the forces governing the interactions among them. The Standard Model (SM) is the most accepted theory which describes the nature and properties of the fundamental particles and their interactions. The elementary particles leptons and quarks, known as fermions, interact through the exchange of gauge bosons and acquire mass through a scalar boson called the Higgs. The four fundamental forces of interaction existing in nature are : the electromagnetic force, the strong force, the weak force and the gravitational force. Quantum Choromodynamics (QCD) is the theory of the strong interactions between the quarks mediated by the massless gluons. The partons (quarks and gluons) have a peculiar property of "color" charge. The quarks strongly binds into colorless particles called hadrons such as protons and neutrons together known as nucleons, pions etc. The structure and the properties of sub-atomic particles can be explored by first accelerating them using particle accelerators and then colliding at very high energies. The end products of these collisions get detected in the particle detectors constituting the real data. The data sets analyzed in details to reveal the structure and characteristic properties of the fundamental particles.

To investigate the very rare particles or to search for physics beyond SM, the particle accelerators have become ever bigger and more complex. The Large Hadron Collider (LHC) is one of the today's biggest and most powerful collider where the protons are accelerated and collided at extremely high center-of-mass energies to probe their internal structure described by parton distribution functions (PDFs). The PDF sets give the probability for finding a parton at an energy scale Q with a fractional momentum x of the proton. Since the proton is not elementary and is made up of partons, the proton-proton (pp) collisions are viewed as interactions between their constituent partons. The final products of the scattering are observed by Compact Muon Solenoid (CMS), one of the detectors located around the interaction points. The scattering cross-section can be defined as a sum of terms with increasing powers of the strong coupling constant α_S convoluted with PDFs. The lowest-order α_S^2 term represents the production of two partons in final states whereas terms of higher-order α_S^3, α_S^4 etc. signify the existence of multi partons in final states. The final state partons give a parton shower (PS) due to decrease in energy through emission of other quarks and gluons. The colored products of parton shower hadronize to a spray of colorless hadrons known as jets. The jets are the final structures observed in the detector. So they carry the significant information about the energy and direction of the initial partons and hence are important to study. The final partons have the probability to radiate more gluons resulting in multijets in the final state. Such events are produced in large number and are an important source for testing the predictions given by QCD. They also serve as an important background in the searches for new particles and physics beyond SM.

The inclusive multijet event cross section σ_{i-jet} given by pp $\rightarrow i\ jets + X$, where every jet counts, is proportional to α_s^i. The inclusive jet cross-section studied in terms of jet p_{T} and rapidity y is one of the important observables as it provides the essential information about the PDFs and the precise measurement of α_S. Also the ratio of cross-sections given by Eq. 1.1 is proportional to the QCD coupling α_S

and hence can be used to determine the value of α_S.

$$R_{mn} = \frac{\sigma_{m-jet}}{\sigma_{n-jet}} \propto \alpha_S^{m-n} \tag{1.1}$$

Instead of studying inclusive cross-sections, the cross-section ratio is more useful because of the partial or complete cancellation of many theoretical and experimental uncertainties between numerator and denominator. The CMS Collaboration has previously measured the ratio of the inclusive 3-jet cross-section to the inclusive 2-jet cross-section as a function of the average transverse momentum, $< p_{T1,2} >$, of the two leading jets in the event at 7 TeV [1] and lead to an extraction of $\alpha_s(M_Z)$ = 0.1148 ± 0.0055, where the dominant uncertainty stems from the estimation of higher-order corrections to the NLO prediction. In this analysis, a measurement of inclusive 2-jet and 3-jet event cross-sections as well as ratio of 3-jet event cross-section over 2-jet R_{32}, is presented using an event sample collected by the CMS experiment during 2012 at the LHC and corresponding to an integrated luminosity of $19.7\,\mathrm{fb}^{-1}$ of pp collisions at a centre-of-mass energy of 8 TeV. The event scale is chosen as before to be the average transverse momentum of the two leading jets, but will be referred to as $H_{\mathrm{T},2}/2$ in this thesis. The measurements are used to determine the value of the strong coupling constant at the scale of the Z boson mass $\alpha_s(M_Z)$ and the running of α_S with energy scale Q is studied.

This thesis is organized as :

Chapter 2 gives a brief overview of the Standard Model of particle physics and the theory of strong interactions QCD with main emphasis on the jets and jet algorithms.

Chapter 3 deals with experimental apparatus which covers the details of the CMS detector and its various sub-detectors.

Chapter 4 describes the methods of event generation using different Monte-Carlo event generators, detector geometry simulation and reconstruction of the particles in the detector. This chapter also gives an overview of the different approaches of jet reconstruction at CMS and application of jet-energy corrections along with the description of the software framework used.

Chapter 5 presents the measurement of inclusive differential multijet cross-sections and the cross-section ratio. The measurements are corrected for detector effects by unfolding procedure which is discussed in details in this chapter. The sources of the experimental uncertainties are studied in details.

Chapter 6 contains a detailed description of the NLO pQCD theory predictions compared to data and the extraction of α_S. The NLO calculations are corrected with the non-perturbative and electroweak corrections. The theoretical uncertainties are calculated from various sources. The unfolded measurements are compared to the predictions at NLO in pQCD and additionally as well as to predictions from several Monte Carlo event generators.

Chapter 7 describes the method to extract $\alpha_s(M_Z)$ from the current measurement and the running of α_S with energy scale Q is presented along with the previous measurements from different experiments.

Chapter 8 summarizes the results and conclusions of the work done in this thesis.

Chapter 2

Theoretical Background

2.1 Jet Algorithms

Chapter 3

Experimental Apparatus

Introduction The LHC is to reveal the physics beyond the Standard Model with centre-of-mass collision energies up to 14 TeV and luminosity up to 10^{34} cm^{-2}s^{-1}. At present, the center-of-mass energy at the LHC is at 8 TeV and it will increase to around 14 TeV collision energy by around 2015. Due to the availability of very high energy for the collisions, it becomes possible for the researchers to understand the fundamental structure of the universe deeply and to look back in its history.

3.1 The Large Hadron Collider

The Large Hadron Collider (LHC) [2] is the world's biggest and the most powerful particle accelerator and collider built by CERN (European Organization for Nuclear Research), at Geneva, Switzerland. It occupies the 27 km circumference circular tunnel (between the border of France and Switzerland), previously used by LEP (Large Electron-Positron) collider [3], at a depth ranging from 50 to 175 metres (164 to 574 ft) underground. Two beams of particles of the same kind, either protons or lead or xenon ions, are accelerated in direction opposite to each other. 1,232 dipole magnets maintain the beams in their circular path and 392 quadrupole magnets keep the beams focused to increase the probabilities of interaction between the particles. Since this thesis is based on the proton-proton (pp) collisions data, the main focus is on protons.

The protons pass through a series of accelerators which increase their energy successively before their injection into the main ring of LHC. Figure 3.1 gives an overview of the various accelerators and detectors comprising the complex structure of the LHC. The protons are obtained by stripping of electrons from hydrogen gas atoms using an electric field. The protons are accelerated up to 100 keV through a radiofrequency quadrupole which provides the first focusing and a further acceleration to 750 keV energy. The linear particle accelerator (LINAC2) increases the energy of protons to 50 MeV. Then these protons are injected into the Proton Synchrotron Booster (PSB) in the form of bunches where they get accelerated to 1.4 GeV energy. The energy of protons is further enhanced to 25 GeV by Proton Synchrotron (PS) and then to 450 GeV by the Super Proton Synchrotron (SPS). Finally the protons are injected into two beam pipelines of the main LHC ring where their energy increases to the collision energy.

The accelerated beams are made to collide at four interaction points around which six detectors : ALICE (A Large Ion Collider Experiment) [4], ATLAS (A Toroidal LHC Apparatus) [5], CMS (Compact Muon Solenoid) [6–8], LHCb (Large Hadron Collider for Beauty) [9], LHCf (Large Hadron Collider forward) [10] and TOTEM (ToTal Elastic and diffractive cross section Measurement) [11], are located. The CMS and ATLAS are the two general purpose detectors dedicated to the search of the Higgs boson, existence of super-symmetry (SUSY) and also looking for extra dimensions. The ALICE is a heavy-ion detector which collides lead ions to study quark-gluon plasma, a state of matter believed to be present just after the Big Bang. The LHCb experiment will explore the differences between matter and antimatter and new physics through b-quark (beauty) studies. TOTEM experiment is dedicated to cross section measurements whereas LHCf focuses on forward physics The LHC operated at the centre-of-mass energy ($\sqrt{s}$) of 7 TeV of pp collisions in the 2010 and

2011 and at $\sqrt{s} = 8$ TeV in the year 2012. After the upgradations , it restarted in 2015 at a much higher centre-of-mass energy of 13 TeV and is running successfully till now. In the coming years, protons will be made to collide at a designed $\sqrt{s} = 14$ TeV with luminosity up to 10^{34} cm^{-2}s^{-1}. In this thesis, work has been carried out using the pp collisions data collected by the CMS detector at $\sqrt{s} = 8$ TeV.

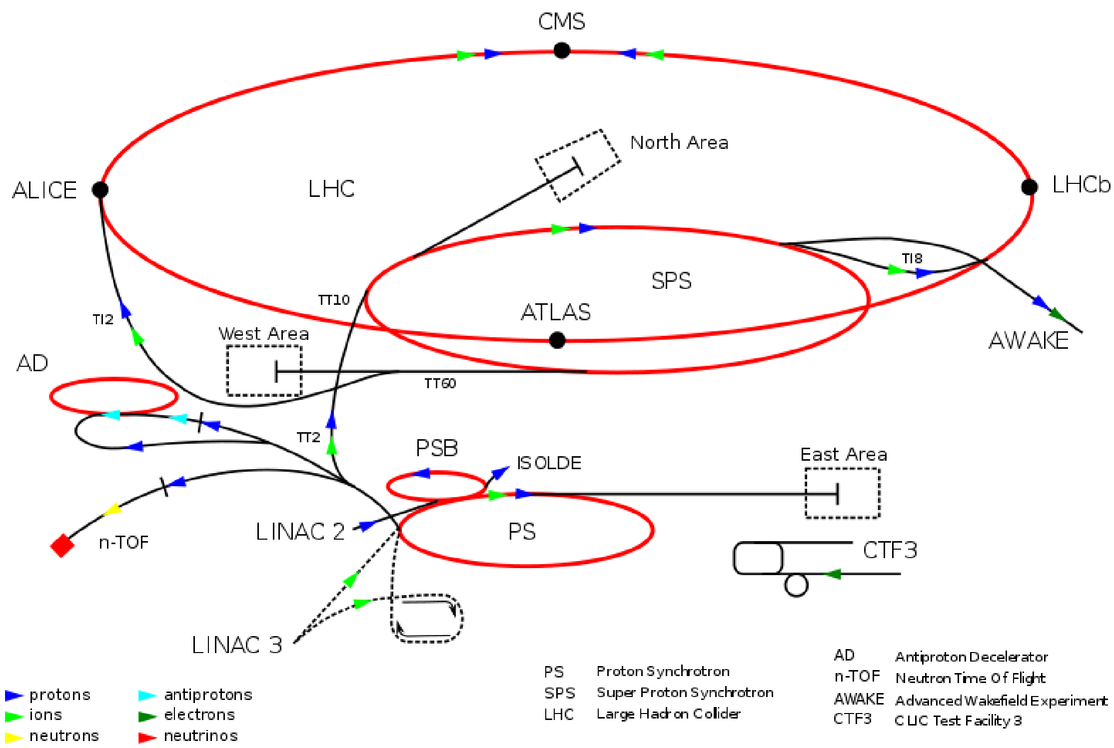

Figure 3.1: Overview of the different experiments of the Large Hadron Collider (LHC), a complex particle accelerator and collider located at CERN[1].

3.2 Luminosity Measurement

Luminosity ($\mathcal{L}$) is one of the most important parameters of an accelerator which characterizes its performance. It gives the rate at which collisions occur and given by the number of collisions produced in a detector per cm^2 and per second. Cross

[1]Source : http://public.web.cern.ch/public/en/research/AccelComplex-en.html

section (σ) is a measurement of the probability that an event occurs. It is related to total number of events N of a process over a time period T and $\mathcal{L}$ as :

$$N = \int_0^T \mathcal{L}\ \sigma\ dt = \mathcal{L}_{int}\ \sigma \tag{3.1}$$

where $\int_0^T \mathcal{L}\ dt = \mathcal{L}_{int}$ is the total integrated luminosity. It is usually expressed in units of barn^{-1} and gives a direct indication of the number of produced events for a process. For example, an integrated luminosity of 10 fb^{-1} means that 10 events are produced in a process with cross section equal to 1 fb.

The luminosity depends on the particle beam parameters and is given by :

$$\mathcal{L} = \frac{N_p^2\ N_b\ f_{rev}\ \gamma\ F}{4\pi\ \epsilon_n\ \beta^*} \tag{3.2}$$

where N_p is the number of particles per bunch, N_b is the number of bunches per beam, f_{rev} is the revolution frequency of the beam, γ is the relativistic gamma factor and F gives the geometric luminosity reduction factor. The effective collision area of the two beams is related to the normalized transverse beam emittance ϵ_n and the value of the betatron function β^* at the interaction point.

The CMS experiment constantly monitors the instantaneous luminosity delivered by LHC which is shown versus time in Fig. 3.2 for proton-proton collisions at nominal center-of-mass energy for the years 2010-2017. The relative instantaneous luminosity is calculated by using two methods [12] : Hadron Forward (HF) method by measuring the particle flux in the hadron forward calorimeter and by counting the number of reconstructed vertices in the pixel tracker. The absolute luminosity measurement relies on van-der-Meer scans done in special runs of the LHC [13]. The uncertainty on the luminosity measured for 2012 data set is 2.5% (syst.) and 0.5% (stat.).

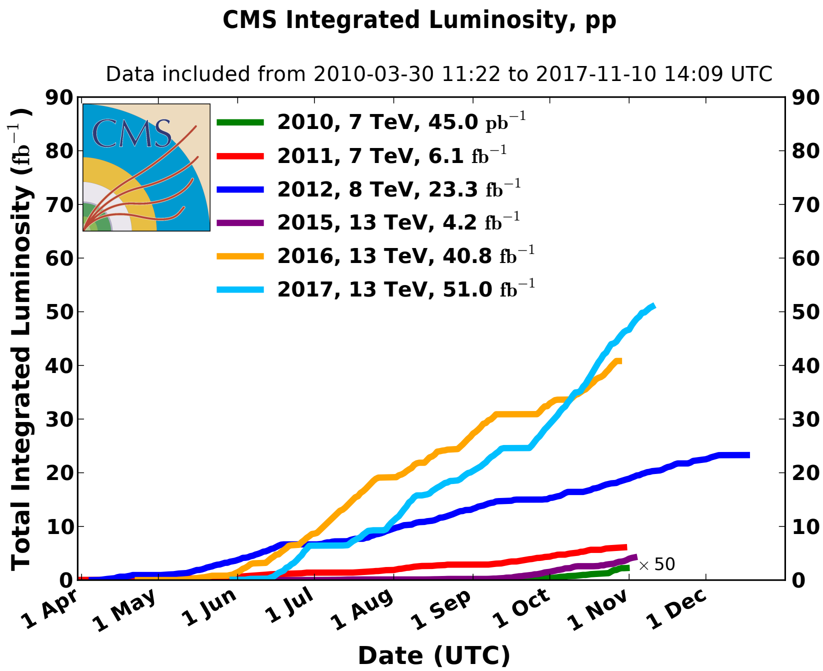

Figure 3.2: The integrated luminosity, delivered to CMS during stable beams for proton-proton collisions at nominal center-of-mass energy, is shown versus time for data-taking in 2010 (green), 2011 (red), 2012 (blue), 2015 (purple), 2016 (orange) and 2017 (light blue) run periods of the LHC[2].

3.3 The Compact Muon Solenoid

The Compact Muon Solenoid (CMS) detector is a general purpose detector located at the interaction point 5 (P5) of the main LHC ring, near the village of Cessy in France. The name of CMS comes from its compact size with main emphasis on the detection of muons and enclosed within high solenoidal magnetic field. The CMS detector aims at identifying the different types of particles produced in proton-proton and heavy ion collisions and measuring their energies and momenta. This is achieved by concentric layers of different sub-detectors arranged in a cylindrical complex structure with 21.6 m length and 15 m diameter. The silicon-based tracker surrounds the the interaction point and forms the innermost layer. It is surrounded

[2]Source : https://twiki.cern.ch/twiki/bin/view/CMSPublic/LumiPublicResults

by a scintillating crystal electromagnetic calorimeter (ECAL) and a sampling hadron calorimeter (HCAL) which are enclosed inside the superconducting solenoid. Outside the magnet lies the large muon detectors embedded inside an iron yoke. The three dimensional view of the CMS detector along with its components is presented in Fig. 3.3. The CMS was constructed in parts at ground and assembled later on

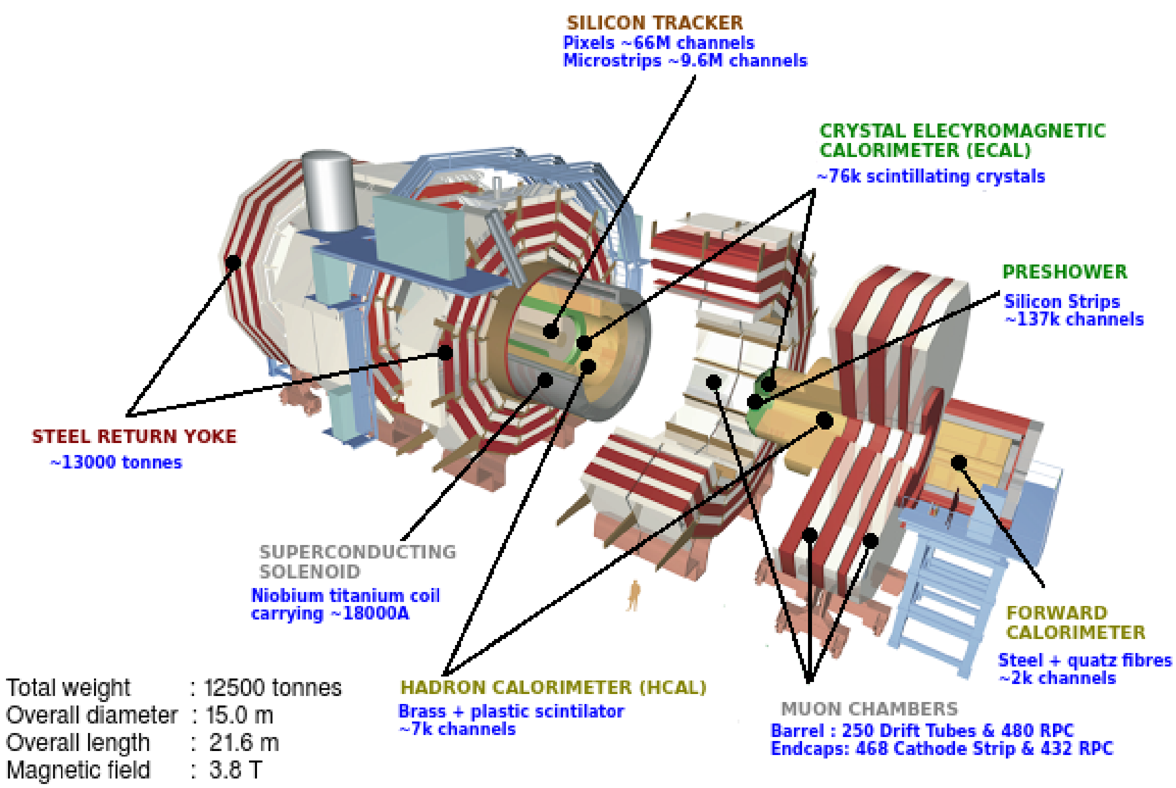

Figure 3.3: The three dimensional view of the CMS detector along with its sub-detector components[3].

in the cavern. The components are easily accessible for upgrades or repairs as the detector can be opened up into movable slices. Figure 3.4 shows the front view of the CMS detector differentiating individual components which contribute to event reconstruction. The path of reconstructed particles is represented by dashed (invisible track) and solid (visible track) lines for different particle classes : photons (γ),

[3]Source : https://orbiterchspacenews.blogspot.in/2013/04/cern-cms-prepares-for-future.html

muons ($\mu^{\pm}$), electrons (e^{-}), neutrons (n) and charged hadrons (pions $\pi^{\pm}$).

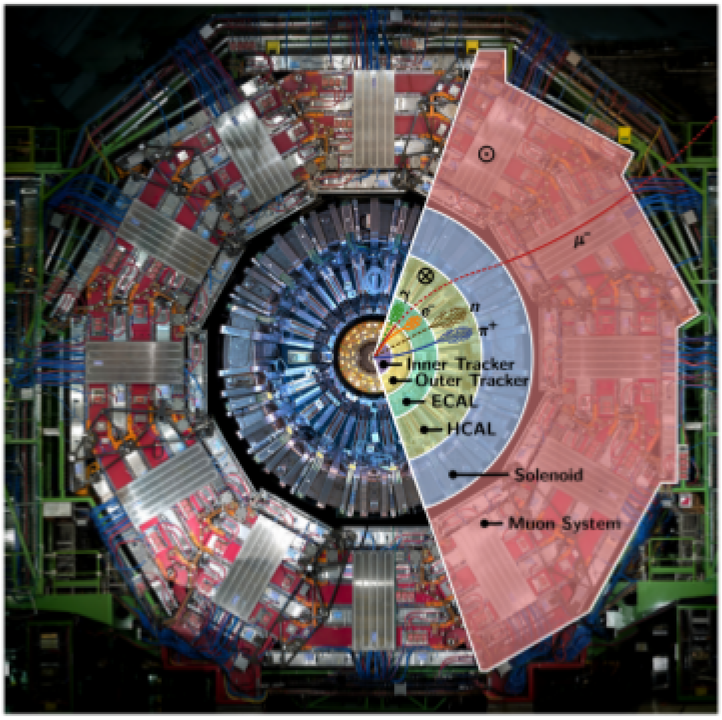

Figure 3.4: Front view of the CMS detector along with its components : inner tracker, outer tracker, electromagnetic calorimeter, hadronic calorimeter, solenoid and muon system. The path of different particles detected by dedicated sub-detectors are shown by dashed (invisible track) and solid (visible track) lines. $\otimes$ and $\odot$ gives the direction of magnetic field inside the solenoid and in the return yoke, respectively. Taken from [8].

A brief overview of the CMS detector has been presented and the details of the its design as well as physics performance are available in Ref. [7,8]. Before going into the details of each sub-detector, first the CMS coordinate system is described in the next section.

3.3.1 Coordinate System

CMS uses right-handed coordinate system having origin at the nominal interaction point of the collision inside the detector. The x-axis points horizontally towards the center of the LHC ring, the y-axis vertically upwards and the z-axis along the beam direction towards the Jura mountains. Following customary polar coordinate conventions, the azimuthal angle ϕ is measured from the x-axis in the x-y plane as $\phi = \tan^{-1}(\frac{y}{x})$, and the polar angle θ, from the z-axis in the z-y plane as $\theta = \tan^{-1}(\frac{x^2+y^2}{2})$. The radial coordinate in x-y plane is denoted by r. The quantities pseudorapidity η and the rapidity y are preferred over the angles θ and ϕ. The pseudorapidity and rapidity are given by Eq. 3.3. Both the quantities are equal for massless particles.

$$
\begin{aligned}
\eta &= -\ln\left(\tan\left(\frac{\theta}{2}\right)\right) \\
y &= \frac{1}{2}\ln\left(\frac{E+p_z}{E-p_z}\right)
\end{aligned}
\tag{3.3}
$$

The difference between rapidities Δy is invariant under longitudinal Lorentz boost whereas it does not hold for η. Hence y is considered in this thesis. The angular distance between the two particles is defined by $\Delta R = \sqrt{(\Delta\eta)^2 + (\Delta\phi)^2}$. The momentum component transverse to the direction of beam p_{T}, is computed from the x- and y-components as $p_{\mathrm{T}} = \sqrt{p_x^2 + p_y^2}$ and the transverse energy is given by $E_T = E\ \sin\theta$.

3.3.2 Inner Tracker System

The charged particles produced from the LHC collisions leave their trajectories as they move outward from the interaction point. These tracks need to be measured very precisely and as close to the collision point as possible. The innermost tracking system of the CMS consisting of silicon detectors measures the hits of charged particles. It surrounds the interaction point and has a cylindrical volume of length of 5.8 m and a diameter of 2.5 m and covers a pseudorapidity range up to $|\eta| <$ ¡ 2.5. When charged particles pass through the silicon detector material, small ionization currents are produced which are detected as a hit. Such multiple hits when combined, reconstruct the track which gives the information about the direction and transverse momentum p_{T} of the charged particle. Silicon detectors have a much higher resolution in tracking charged particles as compared to the older ones such as cloud chambers or wire chambers. CMS inner tracking system shown in Fig. 3.5 consists of two subsystems :

Pixel Detector - A pixel detector lying close to the beam pipe have three co-centric barrel layers at radii of 4.4, 7.3 and 10.2 cm from the beam pipe. It has two disks of pixel modules on each side of barrel. At the LHC design luminosity of 10^{34} cm^{-2}s^{-1}, about 1000 particles from more than 20 overlapping proton-proton interactions traverse through the tracker for each bunch crossing, i.e. every 25 ns. The size of each pixel is 100 µm $\times$ 150 µm which gives an average occupancy of 10^{-4} per bunch crossing. By taking an advantage of the large Lorentz effect, the pixel tracker has a resolution of 10 µm $\times$ 20 µm needed for a precise determination of the primary and secondary vertices and the required momentum resolution.

Strip Detector - After coming out of the pixel detector the charged particles pass through ten layers of silicon strip detectors, reaching out to a radius of 130 cm. The silicon strip detector consists of four inner barrel (TIB) layers assembled in shells with two inner endcaps (TID), each composed of three small discs. The outer barrel (TOB) consists of six concentric layers. Finally two endcaps (TEC) close off the tracker. Each part has silicon modules designed differently for its place within the detector. The strip detector measures the particle tracks with a reduced resolution of 23 µm reflecting the smaller particle flux at larger distances from the interaction point.

The active silicon area of CMS tracker is about 200m^2 which makes it the largest silicon tracker. Along with the measurement of tracks, the energy also needs to be measured for which the calorimeters are present outside the tracker. The tracker should interfere with the particles to a minimum extent so that their momentum can be measured precisely but to measure their energy, they are required to interact with the calorimeters fully.

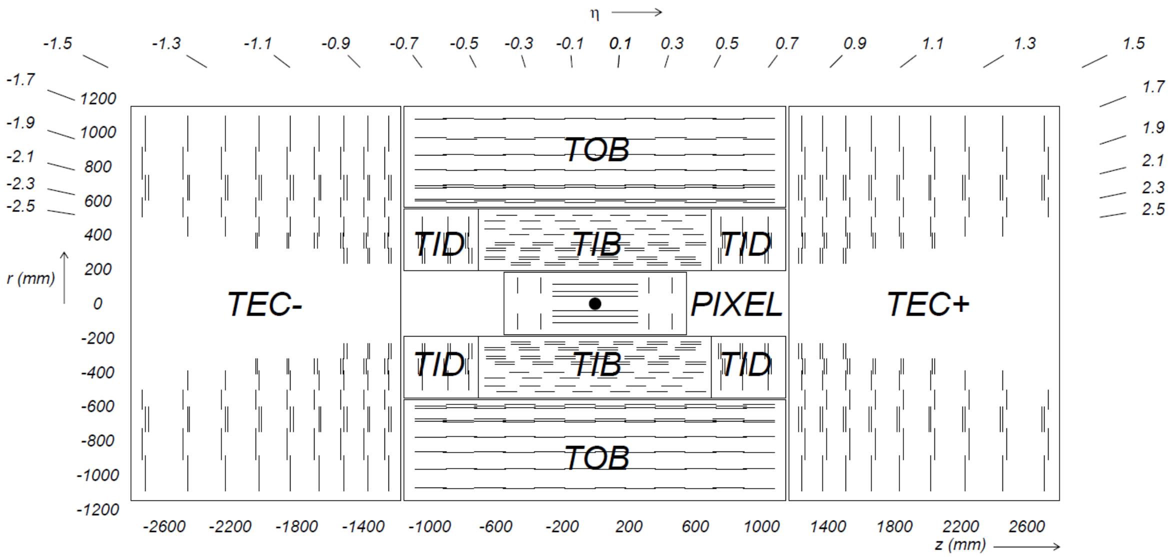

Figure 3.5: The longitudinal section of the inner tracking system consisting of the silicon pixel detector and the silicon strip detector is shown in r-z plane. The silicon strip detector has four components : The Tracker Inner Barrel (TIB) complemented by the Tracker Inner Disks (TID) which are further surrounded by the Tracker Outer Barrel (TOB) in barrel region. Tracker End Cap (TEC) covers high η ranges up to $\eta = 2.5$. Taken from [6].

3.3.3 Electromagnetic Calorimeter

The electromagnetic calorimeter (ECAL) is a homogeneous and hermetic calorimeter used to slow down the produced photons and electrons/positrons and measure their energy by absorb them into the detector material. ECAL consists of an array of lead tungstate ($PbWO_4$) crystals, a very dense material with a short radiation length of $X_0 = 0.89$ cm and covers the pseudorapidity up-to $|\eta| < 3.0$. The particles interact with matter and produce electromagnetic shower through the subsequent processes of bremsstrahlung and electron-positron pair production. The energy of the particles deposited by Compton scattering and the photoelectric effect causes excitation of the material atomic state and the emission of photons. These photons are detected by silicon avalanche photo diodes (APDs) in the barrel region and vacuum phototriodes (VPT) in the end-cap region. The number of created photons gives the direct measure of energy of the incident particle. The incorporation of oxygen makes it highly transparent and enables to emit scintillation light. The small Molière radius of 2.19 cm gives a fine granularity. These properties leads to compact size of ECAL and can be placed easily within the solenoid magnet.

Figure 3.6 presents a geometric view of ECAL in the y-z plane showing the arrangement of different parts of ECAL : the ECAL barrel (EB) extending up to $|\eta| < 1.479$ using more than 60000 crystals and ECAL endcaps (EE) covering the region $1.479 < |\eta| < 3.0$ with an additional 15000 crystals. The preshower detectors (ES) made of lead absorbers and silicon detectors are put in front of the endcaps to distinguish high energetic single photons from low energetic photon pairs originating from neutral pions decays.

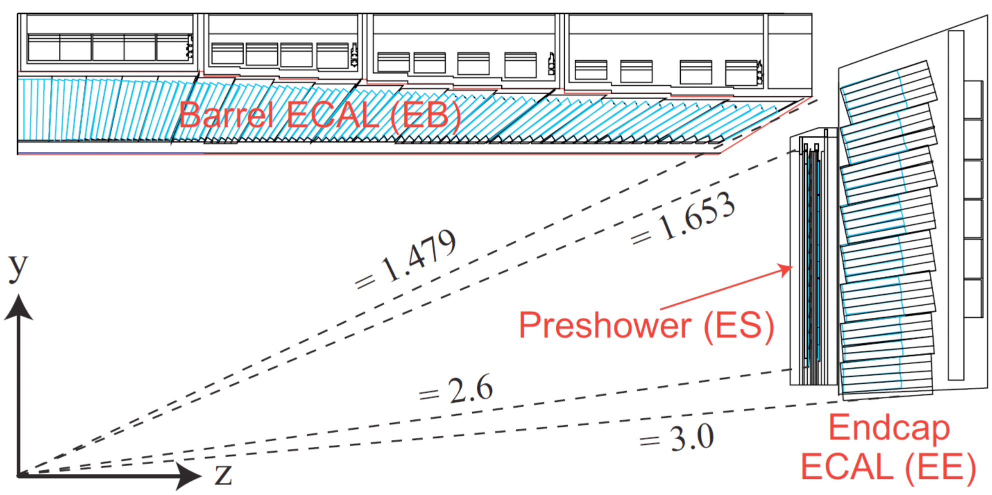

Figure 3.6: A geometric view of one quarter of the electromagnetic calorimeter (ECAL) in y-z plane showing the arrangement of submodules covering the barrel region (EB) and the endcaps (EE). ECAL is complemented with preshower detector (ES) mounted in front of the endcaps. Taken from [7].

The relative energy resolution of the ECAL has been measured to be [14] :

$$\left(\frac{\sigma(\mathrm{E})}{\mathrm{E}}\right)^2 = \left(\frac{2.8\%}{\sqrt{\mathrm{E}}}\right)^2 + \left(\frac{12\%}{\mathrm{E}}\right)^2 + \left(0.30\%\right)^2 \tag{3.4}$$

where E is the energy in GeV. The first term is the stochastic component caused by fluctuations in lateral shower containment and in the energy deposited in the preshower absorber. The second term is the contribution by noise and the last is the constant term comes from the non-uniformity of the longitudinal light collection, inter-calibration errors, and leakage of energy from the back of the crystal.

3.3.4 Hadronic Calorimeter

At LHC, the major fraction of the produced particles are hadrons which are detected by a sampling hadronic calorimeter (HCAL) installed inside the solenoid coil. It is made up of non-magnetic brass absorber having a short interaction length of $\lambda_I =$ 16 cm interleaved with plastic scintillators. The hadrons produced with high energy showers a large number of pions and nucleons by inelastic interactions. The hadronic shower spreads more than the electromagnetic showers because of large transverse momentum of the secondary particles. As the energy of the particles is lower than a certain threshold, the ionization and low-energy hadronic processes come into play. The active scintillation material gets excited and emits blue-violet light. All scintillators are connected to photodiodes using wavelength shifters which read out the signals and pass them to the data acquisition system. The neutral hadrons do not leave track and hence their energy is measured by taking into account the missing transverse energy. The longitudinal view of one quarter of the HCAL presented in Fig. 3.7 shows the different parts :

Hadron Barrel - The hadron barrel (HB) covers the region upto $|\eta| < 1.305$ and overlaps with endcaps for $1.305 \leq |\eta| \leq 1.392$. It has the highest resolution ($\Delta\eta \times \Delta\phi = 0.087 \times 0.087$) and thus optimal region for a data-driven calibration of the jet energy scale. The thickness of the HCAL amounts to 7-11 interaction lengths and which should sufficient enough to stop nearly all hadrons in the calorimeter.

Hadron Outer - The total amount of material in barrel region to absorb the

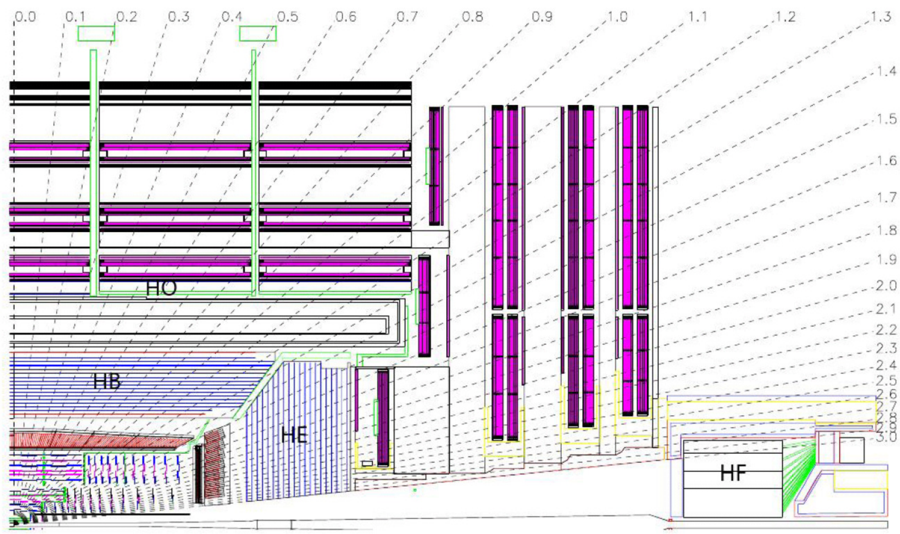

Figure 3.7: Longitudinal view of one quarter of the hadronic calorimeter (HCAL) detector in r-η plane showing its different parts : hadron barrel (HB), hadron outer (HO), hadron endcap (HE) and hadron forward (HF). Taken from [6].

hadronic shower is not sufficient. This requirement is fulfilled by placing an outer hadron (HO) calorimeter as a tail catcher on top of the coil of the magnet. Using the coil as absorbing material, it is able to measure the tails of hadron showers penetrating the HB and the coil.

Hadron Endcap - The hadron endcaps (HE) extends the pseudorapidity range up to $|\eta| < 3.0$. The usage of non-magnetic material in order to not disturb the magnetic field and the close distance to the beamline were the main challenges faced during the construction of the HE. The continuous radiation damages decrease the detector response which need to be corrected and monitored at regular intervals.

Hadron Forward - The hadron forward (HF) calorimeter lies $2.8 < |\eta| < 5.2$ region and is placed more closer to the beam pipe at distance of $z = \pm 11.2$ m from the interaction point. HF detects the jets with very high η and the hadronization products of the beam remnants. It is built using iron absorbers and quartz fibers as active material, which measures the emitted Cerenkov light and produces the signal in the photomultipliers (PMT).

The relative hadronic energy resolution of the barrel HCAL and ECAL combination can be parametrized as :

$$\left(\frac{\sigma(\mathrm{E})}{\mathrm{E}}\right)^2 = \left(\frac{\mathrm{a}}{\sqrt{\mathrm{E}}}\right)^2 + \mathrm{b}^2 \tag{3.5}$$

with a stochastic term a and a constant term b. These values have been measured [15] as $\mathrm{a} = (0.847 \pm 0.016)\ \sqrt{\mathrm{GeV}}$ and $\mathrm{b} = 0.074 \pm 0.008$ whereas for HF the measured values are $\mathrm{a} = 1.98\ \sqrt{\mathrm{GeV}}$ and $\mathrm{b} = 0.09$.

3.3.5 Superconducting Magnet

The superconducting magnet is the key feature of the CMS detector which is 13m long and 6m in diameter. Its refrigerated superconducting niobium-titanium coils cooled at 4 Kelvin produces a magnetic field of 4 Teslas. This intense solenoidal field makes the compactness and cylindrical symmetry of the detector possible. The magnet is placed between the calorimeters and the muon system. The solenoidal magnetic field parallel to the beam bends the tracks of the high momentum charged particles in the transverse plane. The curvature of the trajectory increases with the strength of the magnetic field which make possible to determine the transverse momentum more precisely. The magnet is complemented by a ~10000 tonnes iron yoke which returns the magnetic field.

3.3.6 Muon System

As the name suggests, the detection of muons is of central importance to CMS. Only the muons and neutrinos, out of all the known stable particles, pass through the calorimeter without depositing most or all of their energy. They interact very little with matter and can travel long distances through the dense matter. The

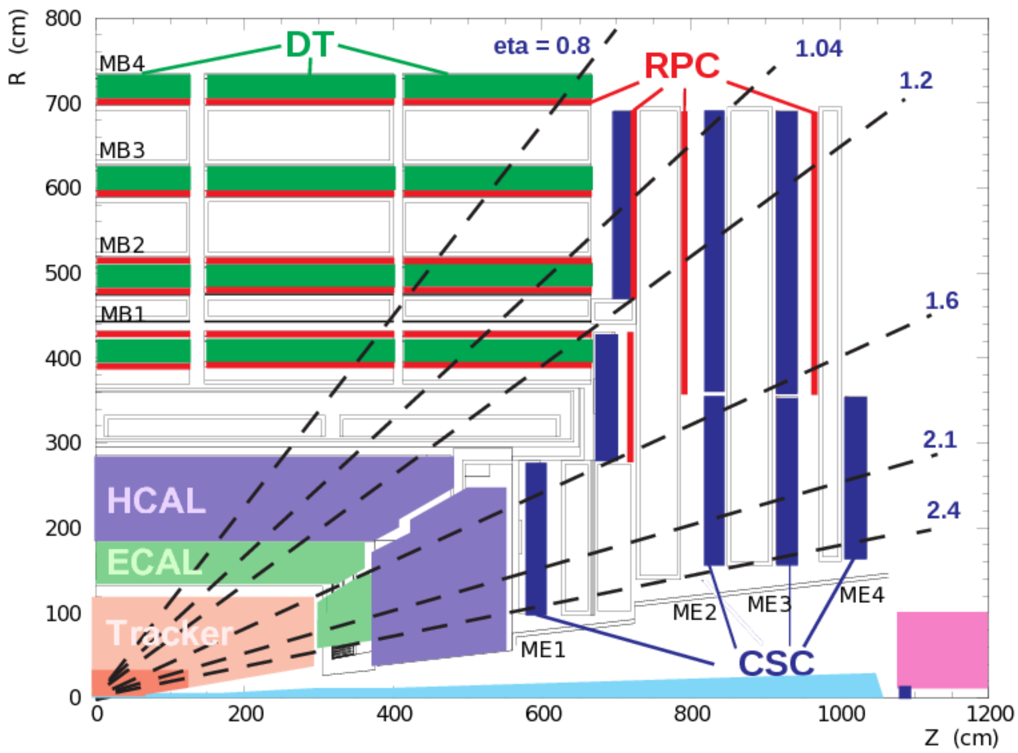

Figure 3.8: A longitudinal view presenting the location of the three muon subsystems : four Drift Tube (DT) stations in the barrel (MB1-MB4, green), four stations of Cathode Strip Chambers (CSC) in the endcap (ME1-ME4, blue), and the Resistive Plate Chambers (RPC) stations (red)[4].

charged muons can be detected by having an additional tracking system outside the calorimeters whereas the neutrinos are practically undetectable as they escape completely without being tracked in any of the layers. Their presence can be detected from the missing energy carried by them. The CMS muon system is installed outside calorimeters in the iron return yoke of the magnet. The muon system perform the muon identification, momentum measurement and triggering. Good muon momentum resolution and trigger capability are enabled by the high-field solenoidal magnet and its flux-return yoke. The latter also serves as a hadron absorber for the identification of muons. The CMS muon system is designed to have the capability of reconstructing the momentum and charge of muons over the entire kinematic range

[4]Source : https://arxiv.org/abs/1209.2646

of the LHC. The muon system shown in Fig. 3.8 consists of three types of gaseous particle detectors :

Drift Tube - The muon barrel (MB) detector has four concentric layers of drift tube (DT) chambers inside the iron yoke which covers the region upto $|\eta| < 1.2$. DT stations are distributed into 5 wheels along the z direction. Each wheel is divided into 12 sectors, each covering a 30° azimuthal angle. The DTs are aluminium tubes of 2.5 m of length and 4.2×1.3 cm^2 of area , filled with gas mixture (58% Ar + 15 % CO_2).

Cathode Strip Chambers - In the forward region, the muon and background flux is higher. So cathode strip chambers (CSC) are preferred because of their fast response time, radiation tolerance and fine segmentation. The four stations of CSCs are installed in each end cap covering in total the region of $0.9 < |\eta| < 2.4$. Each CSC is trapezoidal in shape and consists of 6 gas gaps, each gap having a plane of radial cathode strips and a plane of anode wires running almost perpendicularly to the strips.

Resistive Plate Chambers - Both DT and CSC are accompanied by resistive plate chambers (RPC) which are double-gap chambers, operated in avalanche mode to ensure good operation at high rates. They help to resolve ambiguities in attempting to make tracks from multiple hits in a chamber and provide additional points for determination of a muon trajectory. They provide fast response to the trigger system which is described in the following section.

3.3.7 Trigger and Data Acquisition system

The proton-proton collisions (events) take place at high interaction rates at LHC. In the 2012 run period, at beam crossing frequencies of 25 ns there are 40 million bunch crossings per second with an average of around 20 collisions per bunch crossing. Both the collision and the overall data rates are much higher than the rate at which the information can be stored. So a dramatic rate reduction has to be achieved which is possible with an efficient trigger system by retaining interesting signal events and rejecting background events. The decision of accepting or rejecting an event has to be performed very quickly and it is based on signals of certain physics objects inside the detector. CMS has a two-level complex trigger system :

Level-1 Trigger - The Level-1 (L1) trigger system is based on custom electronics which stores the events at maximum rate of 100 kHz and then forward them to the next level triggers. The L1 system uses only coarsely segmented data from calorimeter and muon detectors, while holding all the high-resolution data in pipeline memories in the front-end electronics. Figure 3.9 shows the workflow of the L1 trigger system. L1 trigger consists of local, regional and global components. The local

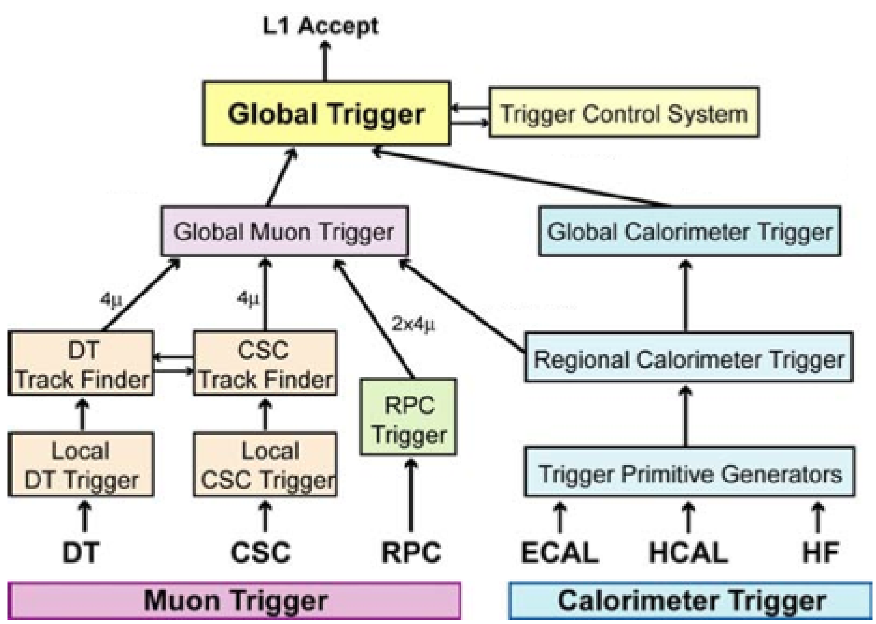

Figure 3.9: Workflow of the L1 trigger system. Taken from [6].

triggers known as Trigger Primitive Generators (TPG), are based on energy deposits in calorimeter trigger towers and tracks in muon chambers. Regional Triggers combine their information and use pattern logic to determine ranked and sorted trigger objects such as electron or muon candidates in limited spatial regions. The rank is determined as a function of energy or momentum and quality, which reflects the level of confidence attributed to the L1 parameter measurements, based on detailed knowledge of the detectors and trigger electronics and on the amount of information available. The Global Calorimeter and Global Muon Triggers determine the highest-rank calorimeter and muon objects across the entire experiment and transfer them to the Global Trigger, the top entity of the Level-1 hierarchy. The latter takes the decision to reject an event or to accept it for further evaluation by the HLT.

High Level Trigger - At the second step, a software-based High-Level Trigger (HLT) is designed to reduce the maximum L1 accept rate of 100 kHz to a final output rate of 100 Hz. The HLT system filter events by performing physics selections using faster versions of the offline reconstruction software. The HLT is provided by a subset of the on-line processor farm which, in turn, passes a fraction of the accepted events to the Data Acquisition (DAQ) system for more complete processing.

3.3.7.1 Jet Triggers

Triggers based on jet and missing transverse energy ($E_{\mathrm{T}}^{\mathrm{miss}}$) triggers are important for search for new physics whereas the single-jet triggers are mainly designed to study quantum chromodynamics (QCD). In this thesis, the single-jet triggers are used to select the events for analysis. At L1, they use mainly information from the calorimeter by looking for an energy cluster and a high energy deposit. The sums of transverse energy from ECAL and HCAL are computed in 4×4 trigger towers, except in the HF region where this quantity is measured in the whole trigger tower itself. If this deposit is greater than a certain threshold, the event is selected at L1 and it is passed to the HLT. Jets are reconstructed in the HLT using the anti-k$_t$ jet clustering algorithm. The inputs for the jet algorithm are either calorimeter towers giving "CaloJet" objects, or the reconstructed particle flow objects giving "PFJet" objects. The processing time of reconstruction algorithm is high and hence the jet trigger paths are divided into multiple selection steps. At first, jets are reconstructed from calorimeter towers. Only for events in which at least one calorimeter jet passes a certain p_{T} threshold, the particle flow algorithm is run and the jets are clustered again from the particle flow candidates. In 2012, most of the jet trigger paths use PFJets as their inputs. The rate of jet events is quite high, so PFJet trigger paths have a pre-selection based on CaloJets. The matching between CaloJets and PFJets is required in single PFJet paths. Due to the flexibility of the HLT, it is possible to apply the jet energy corrections during the HLT selection.

3.3.7.2 Data Acquisition System

As the L1 trigger accepts events at a rate of 100 kHz, the Data Acquisition (DAQ) system has to process the events at the same speed. It reads out the data of all detector subcomponents and assembles the complete events, see Fig. 3.10. The data is subsequently passed to the HLT which further reduces the rates to a few hundred events per second. Finally, the events are merged and saved to a local storage system, from which they are continuously transferred to the Tier-0 computing center at CERN.

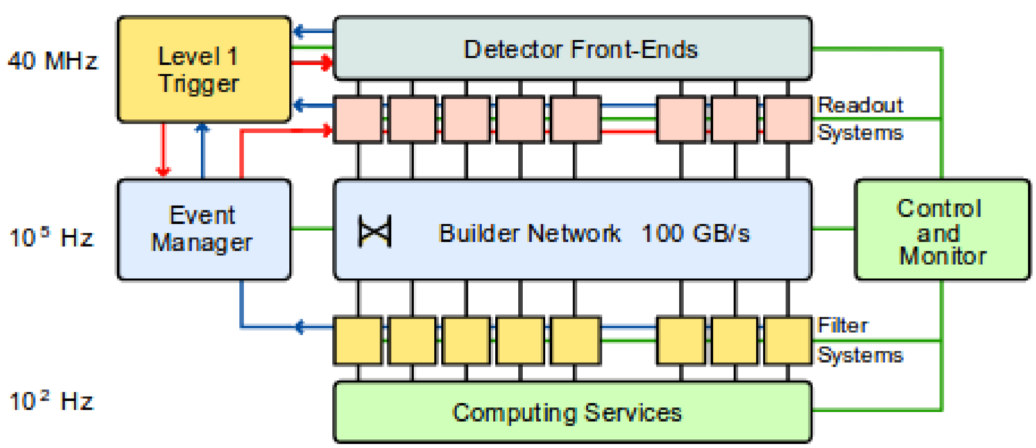

Figure 3.10: Architecture of the CMS DAQ system. Taken from [6].

3.4 Operation of the CMS

Chapter 4

Event Generation, Simulation and Reconstruction

4.1 Computing and Software Tools

4.1.1 Analysis Software

4.1.2 Monte Carlo Event Generators and Simulation Software

4.2 Reconstruction of Jets

A head-on collision between two protons taking place at very high energies can be visualized as an interaction between their constituent quarks and gluons. In a hard scattering process i.e. where the momentum transfer is large, the scattered partons fragment and hadronize into highly collimated bunches of particles. The showers of particles get deposited in the calorimeters in the form of conical structures called "jets". The clustering of the particles is performed by using jet algorithms, discussed in Sec. 2.1, and taking partons, stable particles or reconstructed particle candidates as inputs. The different levels at which the jets are formed are parton level, particle level and reconstructed level, as illustrated in Fig. 4.1. In the CMS detector, jets

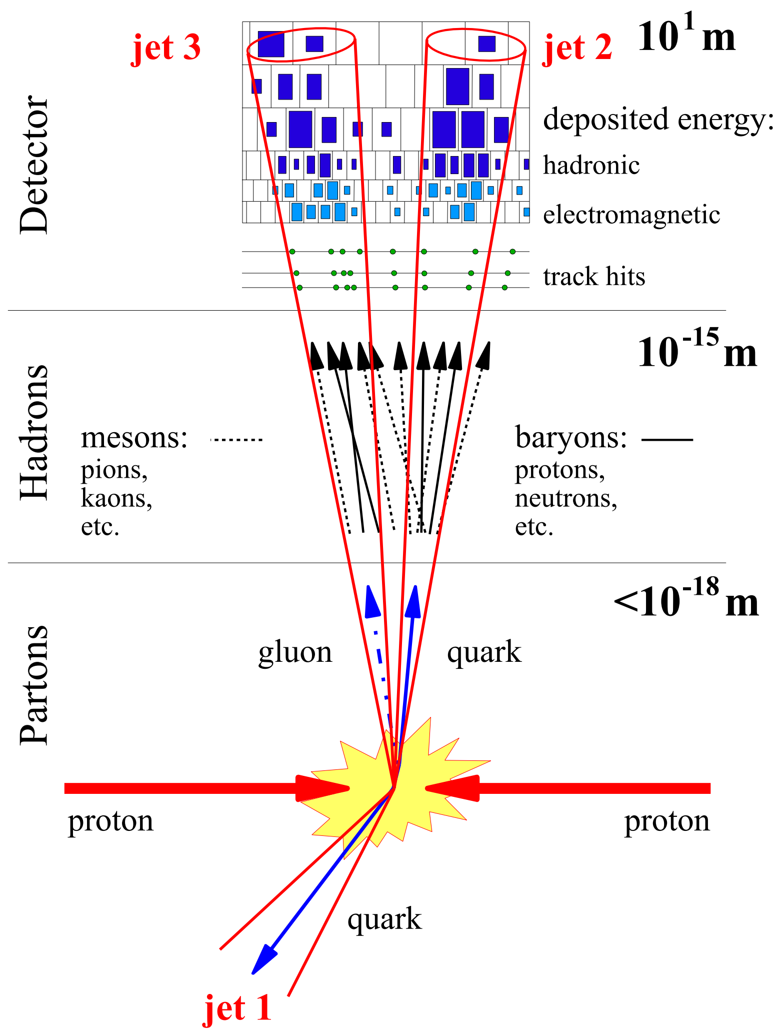

Figure 4.1: In a proton-proton collision, the hard scattered quarks and gluons fragment and hadronize to produce the showers of partons, hadrons, or detector measurements which are clustered into parton jets, particle jets and reconstructed jets, respectively. Taken from [16].

are the localized deposits of energy in the calorimeter cells along with the large number of tracks in the direction of the deposited energy. Depending on the type of input to the jet algorithm, the different reconstruction techniques are available. The jets reconstructed using the energy clusters deposited in the calorimeters are called Calorimeter jets (CaloJets) and the ones clustered by taking particle flow candidates as an input give Particle Flow jets (PFJets).

The analysis presented in this thesis studies the jets clustered using the anti-k$_t$ algorithm with a jet size parameter of R = 0.7 and particle flow candidates. All the particles are reconstructed and identified using a particle-flow (PF) algorithm, discussed in details in next section.

4.2.1 Particle Flow Algorithm

To identify and reconstruct the particles, the CMS employs the event reconstruction technique, Particle Flow (PF) algorithm [17, 18], which combines the information from the individual subdetectors. All the stable particles : electrons, muons, photons, charged and neutral hadrons are reconstructed as well as missing transverse energy ($E_{\mathrm{T}}^{\mathrm{miss}}$) is determined using PF algorithm. $E_{\mathrm{T}}^{\mathrm{miss}}$ is given by the negative vector sum of transverse momemta p_{T} of all the isolated stable particles reconstructed in an event i.e. $E_{\mathrm{T}}^{\mathrm{miss}} = -\sum_{\mathrm{i}} \overrightarrow{p_{\mathrm{T,i}}}$. The transverse momenta of final state stable particles or energies of the calorimeter towers are the inputs to PF algorithm. The additional information of the tracking system enhances the reconstruction performance. The PF algorithm uses the information from the tracks and vertices, hits in the tracking detectors, the energy deposits in ECAL and HCAL as well as the tracks in the muon system. The Combinatorial Track Finder (CTF) algorithm [19] is used to identify the tracks. Based on these tracks, the primary vertices in an event are identified.

The electromagnetic and hadronic calorimeters are divided into a grid of cells based on the detector granularity to identify calorimeter cluster seeds. If there are seeds with an energy exceeding a certain threshold, they are used in an iterative merging algorithm to form Particle Flow clusters. The different elements of the detector information are then linked together into Particle Flow building blocks based on the geometry and 2 fits. At first, muons, which can be well identified using the tracks in the muon detector, are reconstructed using the building blocks connected to the muon system. Blocks connecting the inner tracking system with the ECAL clusters are used to identify electrons. Similarly, charged hadrons are identified using links between the tracking system and the remaining calorimeter clusters. Only neutral objects which leave no traces in the tracking system, remain. ECAL clusters are interpreted as photon candidates, while the remaining HCAL clusters are assumed to be deposits of neutral hadrons. To avoid any kind of double-counting of energy, all Particle Flow building blocks of successfully reconstructed particle candidates are removed and the energy of the calorimeter clusters is recalculated. Finally, a set of so-called Particle Flow candidates is yielded. They consist of well identified particles, which profit from the improved resolution gained by the inclusion of tracking information. This collection of particles is then used to reconstruct the jets and further physical objects.

Chapter 5

Measurement of the Differential Inclusive Multijet Cross-sections and their Ratio

The inclusive differential jet event cross-sections are studied as a function of the average transverse momentum, $H_{\mathrm{T},2}/2 = \frac{1}{2}(p_{\mathrm{T},1} + p_{\mathrm{T},2})$, where $p_{\mathrm{T},1}$ and $p_{\mathrm{T},2}$ denote the transverse momenta of the two leading jets, and are defined by :

$$\frac{\mathrm{d}\sigma}{\mathrm{d}\big(H_{\mathrm{T},2}/2\big)} = \frac{1}{\epsilon\,\mathcal{L}_{\mathrm{int,eff}}} \frac{N_{\mathrm{event}}}{\Delta\big(H_{\mathrm{T},2}/2\big)} \tag{5.1}$$

where N_{event} is the number of inclusive n-jet events counted in an $H_{\mathrm{T},2}/2$ bin, ϵ is the product of the trigger and jet selection efficiencies, which are greater than 99%, $\mathcal{L}_{\mathrm{int,eff}}$ is the effective integrated luminosity, and $\Delta\big(H_{\mathrm{T},2}/2\big)$ are the bin widths. The measurements are reported in units of (pb/GeV). The inclusive n-jet event samples include the events with number of jets $\geq$ n, where n = 2 and 3 in the current study.

The cross-section ratio R_{32}, defined in Eq. 5.2 is obtained by dividing the differential cross-sections of inclusive 3-jet events to that of inclusive 2-jet one, for each bin in $H_{\mathrm{T},2}/2$.

$$R_{32} = \frac{\frac{\mathrm{d}\sigma_{3\text{-}jet}}{\mathrm{d}\left(H_{\mathrm{T},2}/2\right)}}{\frac{\mathrm{d}\sigma_{2\text{-}jet}}{\mathrm{d}\left(H_{\mathrm{T},2}/2\right)}} \tag{5.2}$$

For inclusive 2-jet events ($\mathrm{n_j} \geq 2$) sufficient data are available up to $H_{\mathrm{T},2}/2 = 2000$ GeV, while for inclusive 3-jet events ($\mathrm{n_j} \geq 3$) and the ratio R_{32}, the accessible range in $H_{\mathrm{T},2}/2$ is limited to $H_{\mathrm{T},2}/2 < 1680$ GeV.

5.1 Data Samples

This measurement uses the data which was collected at the centre-of-mass energy of 8 TeV by CMS experiment in the 2012 run period of the LHC. The 2012 data is taken in four periods A, B, C, D and the data sets are divided into samples according to the run period. Further each sample is grouped into subsets based on the trigger decision. For run B-D, the `JetMon` stream datasets contain prescaled low trigger threshold paths (HLTPFJet40, 80, 140, 200 and 260) while the `JetHT` stream datasets contain unprescaled high threshold trigger paths (HLT PFJet320 and 400). For run A, the `Jet` stream contains all the above mentioned trigger paths. The data to be used in physics analysis must satisfy a certain criteria according to which it should fulfill the validation requirements of data quality monitoring procedure. CMS uses JSON (Java Script Object Notation) format files to store the range of good lumi sections within a run. In the current analysis, the applied certification file[1] is based on the final event reconstruction of the 2012 CMS data sets. The datasets used in the current study are mentioned in the Table 5.1 along with the luminosity of each dataset which increases with period. Full 2012 data sample corresponds to an integrated luminosity of 19.71 fb^{-1}.

[1] Cert_190456-208686_8TeV_22Jan2013ReReco_Collisions12_JSON

Table 5.1: Run range and luminosity of the proton-proton collisions data collected at the centre-of-mass energy of 8 TeV by CMS experiment in the year of 2012 in four different run periods A, B, C and D.

Run	**Run range**	**Data set**	**Luminosity** fb^{-1}
A	190456-193621	/Jet/Run2012A-22Jan2013-v1/AOD	0.88
B	193834-196531	/Jet[Mon,HT]/Run2012B-22Jan2013-v1/AOD	4.41
C	198022-203742	/Jet[Mon,HT]/Run2012C-22Jan2013-v1/AOD	7.06
D	203777-208686	/Jet[Mon,HT]/Run2012D-22Jan2013-v1/AOD	7.37

5.1.1 Monte Carlo Samples

To have a comparison of data results with the simulated events, the MadGraph5 [20] Monte-Carlo (MC) event generator has been used. The MadGraph5 generates matrix elements for High Energy Physics processes, such as decays and $2 \rightarrow n$ scatterings. It has been interfaced to pythia6 [21] by the LHE event record [22], to generate the rest of the higher-order effects using the Parton Showering (PS) model, with tune Z2* to model the underlying event. Matching algorithms make sure that thers is no double-counting between the tree-level and the PS-model-generated partons. The MC samples are processed through the complete CMS detector simulation to allow studies of the detector response and compare to measured data on detector level.

The cross-section measured as a function of the transverse momentum p_{T} or the scalar sum of the transverse momentum of all jets H_{T} falls steeply with the increasing p_{T}. So in the reasonable time, it is not possible to generate a large number of high p_{T} events. Hence, the events are generated in the different phase-space region binned in H_{T} or the leading jet p_{T}. Later on, the different phase-space regions are added together in the data analyses by taking into account the cross-section of the different phase-space regions. The official CMS MadGraph5+pythia6 (MG5+P6) MC samples used in this analysis are generated as slices in the H_{T} phase-space are tabulated in Table 5.2 along with their cross-sections and number of events generated.

Table 5.2: The official Monte Carlo samples are produced in phase space slices in H_{T} with the generator MadGraph5 and interfaced to pythia6 for the parton shower and motorization of the events. The cross-section and number of events generated are mentioned for each sample.

Generator	Sample	Events	Cross-section pb
MadGraph5 + pythia6	/QCD_HT-100To250_TuneZ2star_8TeV-madgraph-pythia6/ Summer12_DR53X-PU_S10_START53_V7A-v1/AODSIM	50129518	1.036×10^7
	/QCD_HT-250To500_TuneZ2star_8TeV-madgraph-pythia6/ Summer12_DR53X-PU_S10_START53_V7A-v1/AODSIM	27062078	2.760×10^5
	/QCD_HT-500To1000_TuneZ2star_8TeV-madgraph-pythia6/ Summer12_DR53X-PU_S10_START53_V7A-v1/AODSIM	30599292	8.426×10^3
	/QCD_HT-1000ToInf_TuneZ2star_8TeV-madgraph-pythia6/ Summer12_DR53X-PU_S10_START53_V7A-v1/AODSIM	13843863	2.040×10^2

5.2 Event Selection

The events are selected according to several quality criteria which ensures the high purity and high selection efficiency of the sample to be studied. This event selection also reduces beam induced background, detector-level noise and jets arising from fake calorimeter energy deposits.

5.2.1 Trigger Selection

CMS implements a two-level trigger system to reduce the amount of recorded events to a sustainable rate. In this analysis the jets are the final objects to study. So single jet trigger paths with varying thresholds are used to select events in data. It consists of one L1 trigger seed and multiple HLT filters. The L1 jet trigger uses transverse energy sums computed using both HCAL and ECAL in the central region ($|\eta| < 3.0$) or HF in the forward region ($|\eta| > 3.0$). The single jet triggers (HLT_PFJetX) used for the current study are tabulated in Table 5.3. A single jet trigger selects an event in which at least one jet has the transverse momentum above the threshold. HLT_PFJetX implies that there is at-least one jet in the event, whose $p_{\mathrm{T}} > \mathrm{X}$ (GeV). The L1 trigger has a lower threshold to ensure full efficiency versus p_{T} of the HLT trigger. The p_{T} spectrum is steeply falling and hence the rates for low-p_{T} jets are very high. So it is not feasible to use a single unprescaled trigger for the selection of all required events. To collect sufficient data in the lower part of the p_T spectrum, different five prescaled low-p_T trigger paths, each with different prescale value, are used. Also, one unprescaled trigger i.e. HLT_Jet320 is used in the high p_T region, in which the rate is sufficiently small to collect and store all events. During the reconstruction of the spectrum, the prescales have been taken into the account.

Table 5.3: The single jet trigger paths used in the analysis are listed here. The column $H_{T,2}/2$, 99% indicates the value of $H_{T,2}/2$ at which each trigger exhibits an efficiency larger than 99%. The last column gives the effective luminosity seen by each trigger which divided by the total integrated luminosity of 19.71 fb^{-1}, gives the effective prescale applied on a trigger over the whole run period.

Trigger Path	**L1 threshold** GeV	**HLT threshold** GeV	$\boldsymbol{H_{T,2}/2}$**, 99%** GeV	**Eff. Lumi** fb^{-1}
HLT_PFJet80	36	80	120.0	0.0021
HLT_PFJet140	68	140	187.5	0.056
HLT_PFJet200	92	200	262.5	0.26
HLT_PFJet260	128	260	345.0	1.06
HLT_PFJet320	128	320	405.0	19.71

The efficiency of each trigger path as a function of $H_{T,2}/2$ is described by the turn-on curves with a rising part where the trigger is partly inefficient, until a plateau region where the trigger is fully efficient. Hence it is important to determine the threshold above which a trigger becomes fully efficient. The threshold is the value at which the trigger efficiency exceeds 99%. The trigger efficiency for HLT_PFJetY is given by Eq. 5.3 where HLT_PFJetX is the reference trigger and is assumed to be fully efficient in the considered phase space region. The value of X is chosen previous to that of Y in p_T ordering from the trigger list so that the higher trigger condition can be emulated from the lower trigger path.

$$\epsilon_{\mathrm{HLT\_PFJetY}} = \frac{H_{T,2}/2\left(\mathrm{HLT\_PFJetX} + (\mathrm{L1Object\_p_T} > \mathrm{Z}) + (\mathrm{HLTObject\_p_T} > \mathrm{Y})\right)}{H_{T,2}/2(\mathrm{HLT\_PFJetX})} \tag{5.3}$$

where Y is the p_T threshold of HLT_PFJetY and Z is the L1 seed value corresponding to the trigger path HLT_PFJetY. The denominator represents the number of events for which the reference trigger path HLT_PFJetX has been fired. The numerator is the number of events for which HLT_PFJetX has been fired along the p_{T} of L1Object $\geq$ Z and the p_{T} of HLTObject $\geq$ Y. For example, to obtain turn-on curve for HLT_PFJet260, HLT_PFJet200 is the reference HLT path. The p_{T} cut on L1Object is 128 GeV and p_{T} cut on HLTObject is 260 GeV. The threshold point at which the trigger efficiency is larger than 99% is determined by fitting the turn-on distribution with a sigmoid function described in Eq. 5.4. The trigger turn-on curves as a function of $H_{\mathrm{T},2}/2$ can been seen in Fig. 5.1 which are described by a sigmoid function (blue line). The error bars give the uncertainty on the efficiency which is calculated using Clopper-Pearson confidence intervals [23].

$$f_{fit}(x) = \frac{1}{2}\left(1 + erf\left(\frac{x-\mu}{\sqrt{2}\sigma}\right)\right) \tag{5.4}$$

5.2.2 Primary Vertex Selection

The reconstructed tracks, selected based on the transverse impact parameter significance with respect to the beam line, number of strip and pixel hits and the normalized track χ^2, identify the primary vertex (PV). The tracks are clustered according to the z-coordinate of their point of closest approach to the beam axis. A selection criteria for primary vertex should be followed which helps to identify and reject the beam background events. At-least one good primary vertex reconstructed from at least four tracks within a distance of $\left|z(PV)\right| < 24$ cm to the nominal interaction point in a collision, is required in each event. The radial distance in x-y plane, ρ(PV) should be not be greater than 2 cm. The number of degrees of freedom in fitting for the position of each vertex using its associated tracks should be at-least four in number.

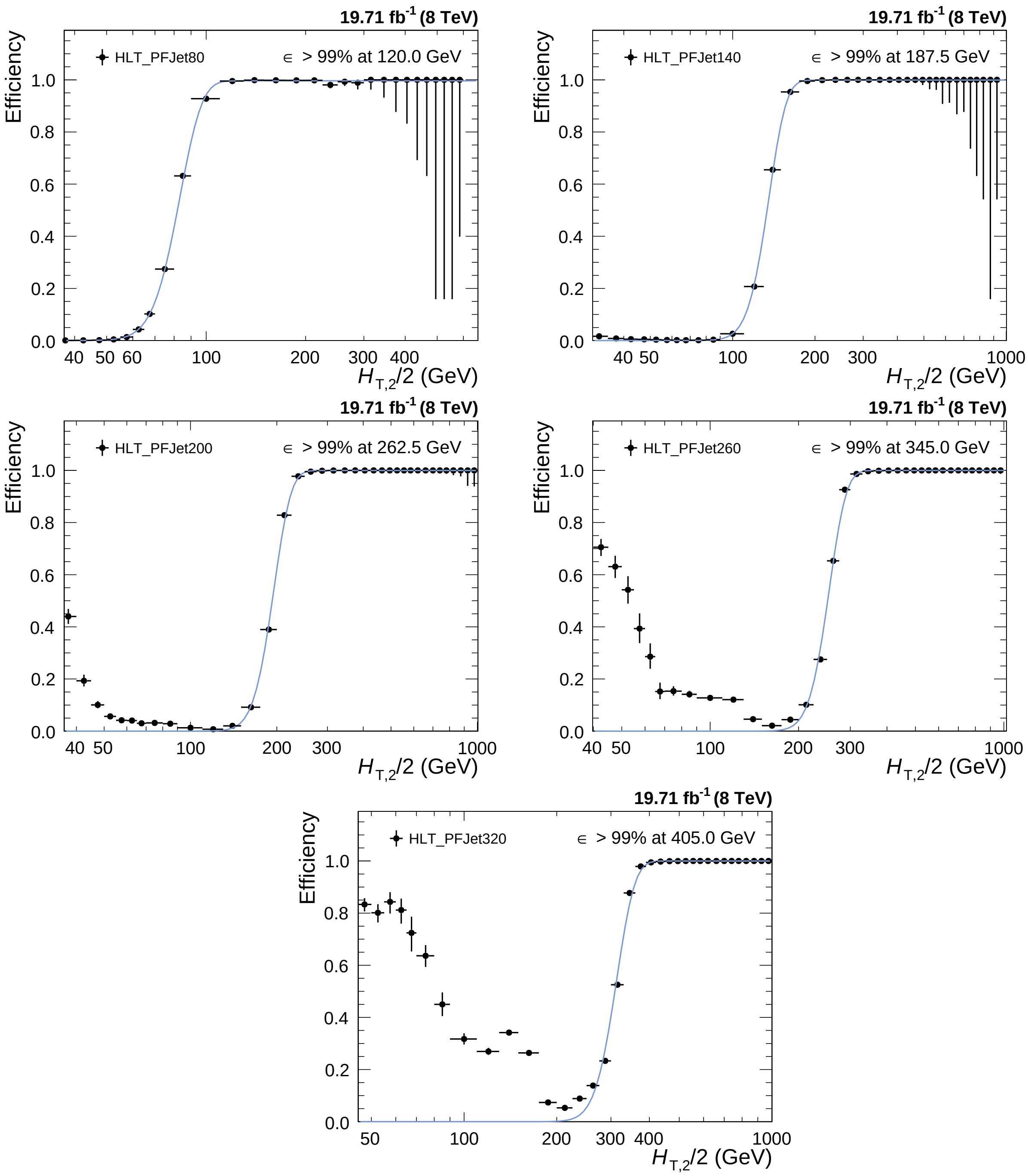

Figure 5.1: Trigger efficiencies turn-on curves for the single jet trigger paths are fitted with a sigmoid function (blue line) to obtain the 99% efficiency threshold. The error bars give the uncertainty on the efficiency which is calculated using Clopper-Pearson confidence intervals [23].

5.2.3 Missing Transverse Energy

In an ideal detector where all particles could be identified and perfectly measured, the transverse momentum of all particles would sum up to zero. But the neutral weakly interacting particles, such as neutrinos, escape from typical collider detectors and do not produce any direct response in the detector elements. The imbalance of total momentum of all visible particles can give the hints of the presence of such particles. The vector momentum imbalance in the plane perpendicular to the beam direction is known as missing transverse momentum or energy ($E_{\mathrm{T}}^{\mathrm{miss}}$). It is one of the most important observables for discriminating leptonic decays of W bosons and top quarks from background events which do not contain neutrinos, such as multijet and Drell–Yan events or searches for physics beyond the Standard Model.

The ratio of missing transverse energy to the total transverse energy $E_{\mathrm{T}}^{\mathrm{miss}}/\sum E_{\mathrm{T}}$, shown in Fig. 5.2 for $\mathrm{n_j} \geq 2$ (left) and $\mathrm{n_j} \geq 3$ events (right), shows a discrepancy between data (black solid circles) and simulated MC (blue histogram), at the tail part of the distribution. This is because of a finite contribution from $\mathrm{Z}(\rightarrow \nu\bar{\nu})$ + jet events which gives rise to non-zero E_{T} in the events in data. Such events are absent in QCD simulated events in MC. Hence $E_{\mathrm{T}}^{\mathrm{miss}}/\sum E_{\mathrm{T}}$ is required to be less than 0.3 to reject events with high $E_{\mathrm{T}}^{\mathrm{miss}}$.

5.2.4 Jet Identification

In order to suppress fake jets, arising from detector noise or misreconstructed particles, jet identification criteria (ID) has been applied. Instead of applying it event-wise, it is applied it on each jet. The algorithm works on reconstructed jets using information of the clustered particle candidates. The official tight jet ID [24], recommended by JETMET group [25] is used. Due to pileup and electronic noise the jet constituent fractions may vary from event to event. In order to reject the noisy jets, some jet selection criteria are optimized to select only good quality jets. The selec-

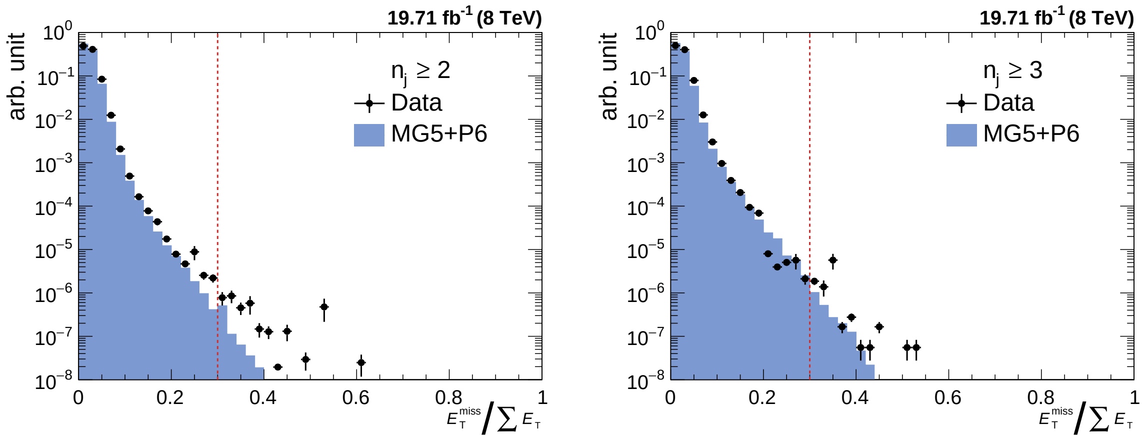

Figure 5.2: Missing transverse energy fraction of the total transverse energy per event in data (black solid circles) and simulated Monte Carlo events (blue histogram) in inclusive 2-jet (left) and 3-jet events (right). To remove background and noise, events with a fraction exceeding a certain threshold, here indicated with the red dashed line, are rejected.

tion criteria are implemented as selection cut on jet fractions. Table 5.4 summarizes the properties of the reconstructed jets and their respective cuts. Each jet should contain at least two particles, one of which should be a charged hadron. The cut on the fraction of neutral hadrons and photons removes HCAL noise and ECAL noise, respectively. Muons that are falsely identified and clustered as jets are removed by the muon fraction criterion. Based on information of the tracker, additional selection cuts are enforced in the region $|\eta| < 2.4$. The charged electromagnetic fraction cut removes the jets clustered from misidentified electrons. Furthermore, the fraction of charged hadrons in the jet must be larger than zero and jets without any charged hadrons are very likely to be pileup jets. The Figs. 5.3 and 5.4 show the distributions of the jet constituents observed in data (black solid circles) and simulated MC events (blue histogram) for $\mathrm{n_j} \geq 2$ and $\mathrm{n_j} \geq 3$, respectively.

5.2.4.1 Jet ID Efficiency

The efficiency of the jet ID as a function of $H_{\mathrm{T},2}/2$ is studied using a tag-and-probe technique with dijet events. The two leading jets are required to be back-to-back in the azimuthal plane such that $|\Delta\phi - \pi| < 0.3$. One of the dijets is selected randomly

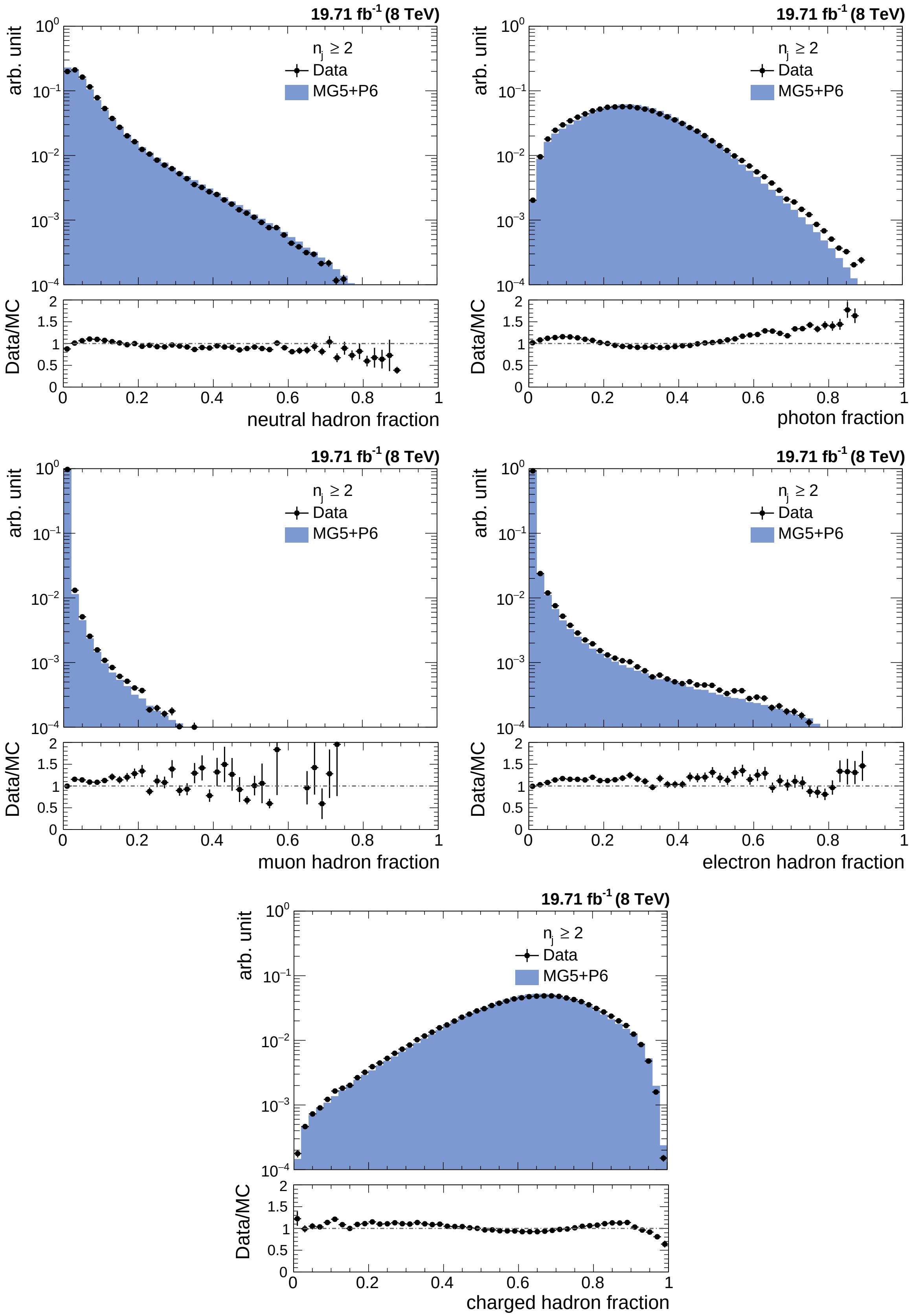

Figure 5.3: The fractions of jet constituents as observed in data (black solid circles) and simulated Monte Carlo events (blue histogram) for different types of PF candidates for inclusive 2-jet events. Data and simulations are normalized to the same number of events. The distributions are shown after the application of the jet ID.

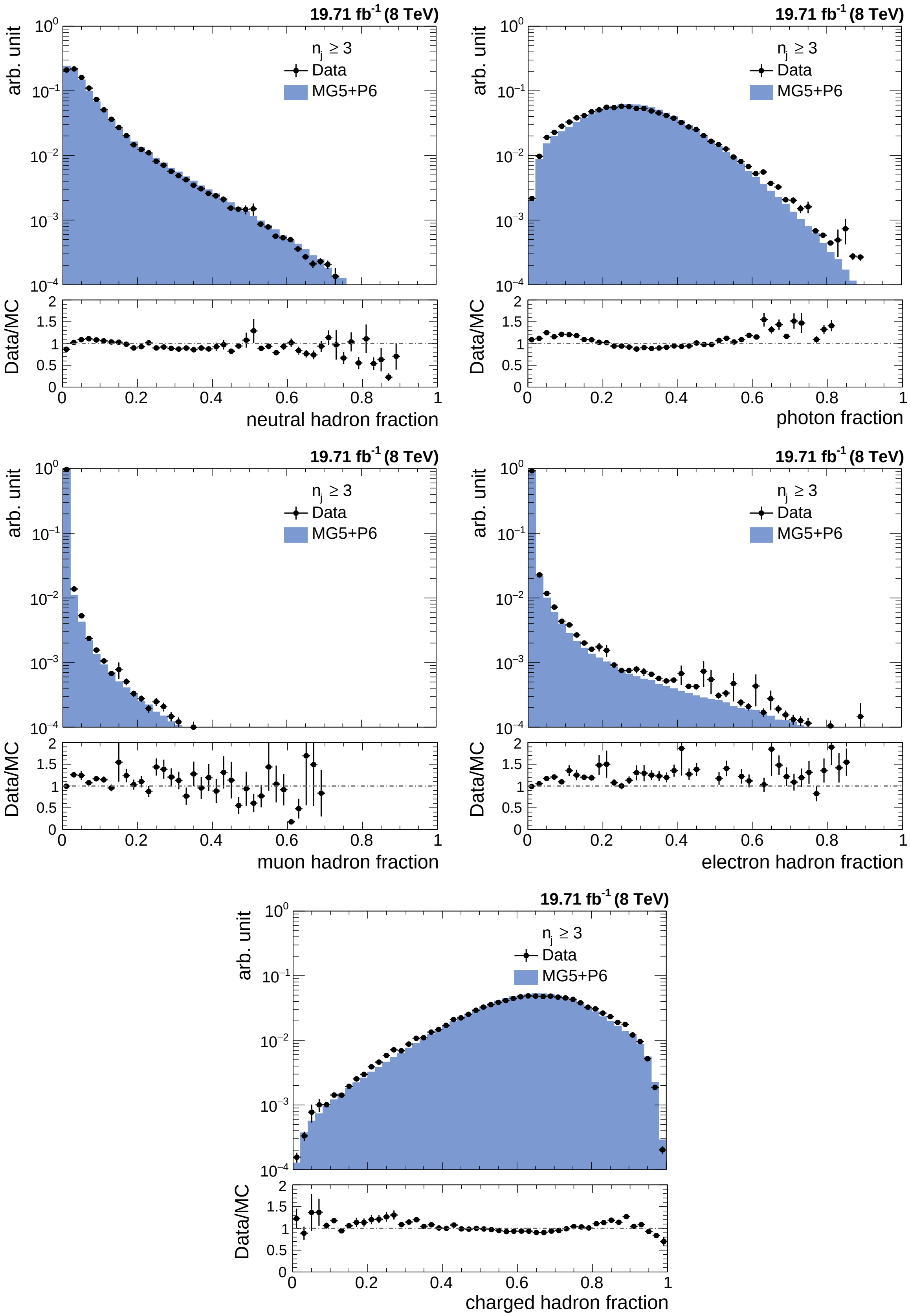

Figure 5.4: The fractions of jet constituents as observed in data (black solid circles) and simulated Monte Carlo events (blue histogram) for different types of PF candidates for inclusive 3-jet events. Data and simulations are normalized to the same number of events. The distributions are shown after the application of the jet ID.

Table 5.4: The jet ID removes noise and fake jets based on the properties of the reconstructed jets and the clustered particle candidates. All the selection cuts which are recommended by the JETMET group are applied [25].

	Property	**Loose ID**	**Tight ID**
Whole η region	neutral hadron fraction	< 0.99	< 0.90
	neutral EM fraction	< 0.99	< 0.90
	number of constituents	> 1	> 1
	muon fraction	< 0.80	< 0.80
only $\|\eta\| < 2.4$	charged hadron fraction	> 0	> 0
	charged multiplicity	> 0	> 0
	charged EM fraction	< 0.99	< 0.90

as a "tag" jet which is required to fulfill the tight jet ID criteria. The other jet is called "probe" jet for which it is examined, whether it also passes the tight jet ID. The ID efficiency is defined as the ratio of events where the probe jet passes the ID requirements, over the total number of dijet events. It is shown as function of $H_{\mathrm{T},2}/2$ in Fig. 5.5 and as expected, it is always greater than 99%. The QCD cross-section decreases as a function of $H_{\mathrm{T},2}/2$ and hence the number of events decrease on moving to higher $H_{\mathrm{T},2}/2$. Consequently the statistical fluctuations for ID efficiency are larger at higher $H_{\mathrm{T},2}/2$.

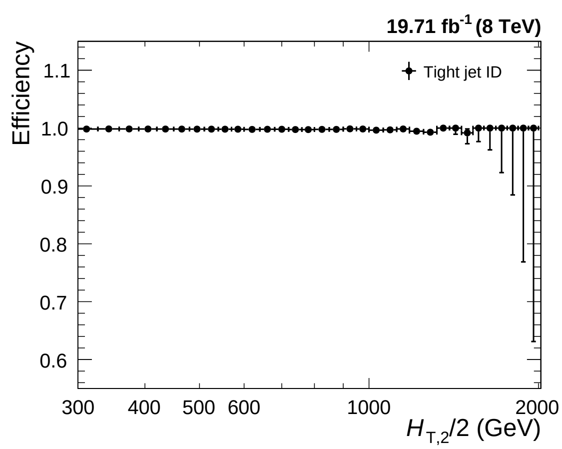

Figure 5.5: The jet ID efficiency is studied as a function of $H_{\mathrm{T},2}/2$ with tag-and-probe technique using dijet event topologies and it always exceeds 99%.

5.2.5 Jet Selection

The measurement of differential cross-sections and their ratio uses jets clustered from particle flow candidates using the anti-k$_t$ jet algorithm with a size parameter, R = 0.7. The energy scale of the jets is corrected with the CMS recommended jet energy corrections, described in Sec. **?** . These corrections are applied to jets in both data[2] as well those in simulated events[3]. The jet selection, based on phase space cuts on transverse momentum and rapidity of jets in an event, is as follows :

- All jets having $p_{\mathrm{T}} > 150$ GeV and $|y| < 5.0$ are selected.
- Events with at least two jets are selected.
- The two leading jets should have $|y| < 2.5$ and further jets are counted only, if they lie within the same central rapidity range of $|y| < 2.5$.

These cuts assure high detector acceptance and exactly same selection is applied in the measurement, simulated events as well in theoretical calculations for a consistent comparison.

5.3 Comparison with Simulation

5.3.1 Pile-up Reweighting

While generating the official Monte-Carlo samples, the number of pileup interactions describing the conditions expected for each data-taking period are taken care of. But the number of pile-up events implemented in the simulation $N_{\mathrm{MC}}(N_{\mathrm{PU,truth}})$, does not match exactly with the one measured actually in data $N_{\mathrm{data}}(N_{\mathrm{PU,est.}})$. To match the pile-up distributions in data, a reweighting factor w_{PU}, as given by Eq. 5.5 is applied

[2] Winter14_V8 jet energy corrections
[3] START53_V27 jet energy corrections

to the simulated events. In Fig. 5.6 the number of reconstructed vertices are shown before (left) and after pile-up reweighting (right). It is observed that before pile-up reweighting there was a significant mismatch of the pile-up distributions in data (black solid circles) and simulated MC events (blue histogram), which completely vanishes after reweighting.

$$w_{\mathrm{PU}} = \frac{N_{\mathrm{data}}(N_{\mathrm{PU,est.}})/\sum N_{\mathrm{data}}}{N_{\mathrm{MC}}(N_{\mathrm{PU,truth}})/\sum N_{\mathrm{MC}}} \tag{5.5}$$

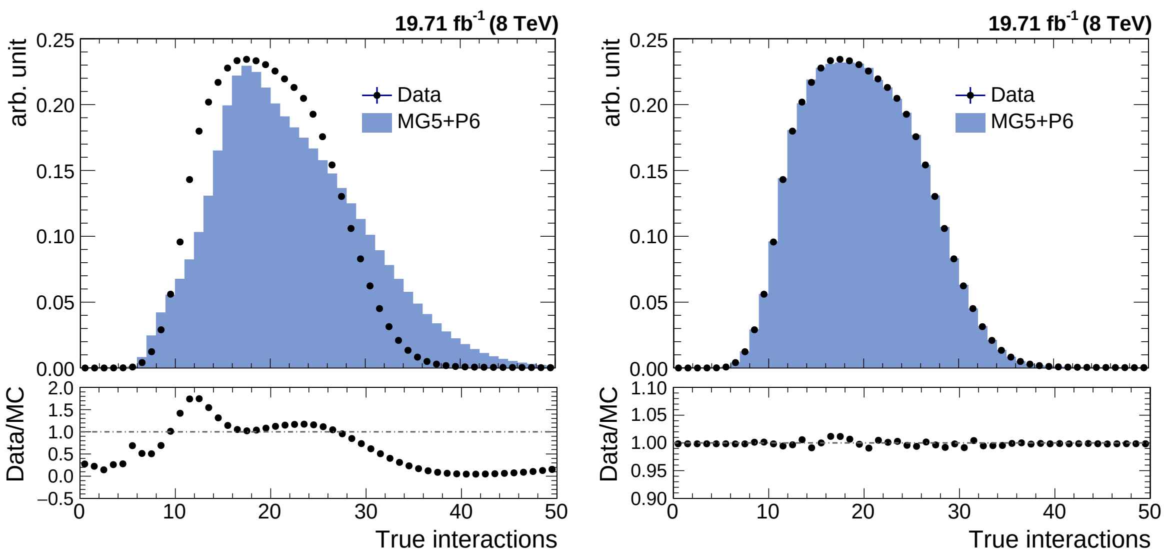

Figure 5.6: Number of reconstructed vertices in data (black solid circles) and simulated Monte Carlo events (blue histogram) before (left) and after (right) the pile-up reweighting.

5.3.2 Comparison of Cross-sections and their Ratio

The measured data distribution of differential cross-section at detector level is compared to the predictions of Monte Carlo simulation using MadGraph5 generator interfaced with pythia6 (MG5+P6) including the detector simulation as well as to a fixed-order theory prediction obtained using CT10-NLO PDF set. Figure 5.7 shows the comparison of differential cross-section as a function of $H_{\mathrm{T,2}}/2$ for $\mathrm{n_j} \geq 2$ (left) and $\mathrm{n_j} \geq 3$ events (right), for data (black solid circles), MG5+P6 MC (red empty circles) and CT10-NLO (blue histogram). The bottom panel in each plot shows the ratio of data to the MC predictions (red line) as well as to the CT10-NLO theory predictions (blue line). The NLO predictions on parton level are not corrected for non-perturbative effects. Still the NLO predictions describe the data better as compared to the LO MC simulations which roughly describes the spectrum on detector level. The sufficient data for $\mathrm{n_j} \geq 2$ and $\mathrm{n_j} \geq 3$ events are available up to $H_{\mathrm{T},2}/2$ = 2000 GeV and 1680 GeV, respectively. Due to some kinematical constraints, the minimum cut on $H_{\mathrm{T},2}/2$ is 300 GeV (explained in Sec. 6.1.1. Hence the differential cross-sections are studied in the range 300 GeV $\leq H_{\mathrm{T},2}/2 <$ 2000 GeV for $\mathrm{n_j} \geq 2$ and 300 GeV $\leq H_{\mathrm{T},2}/2 <$ 1680 GeV for $\mathrm{n_j} \geq 3$ events.

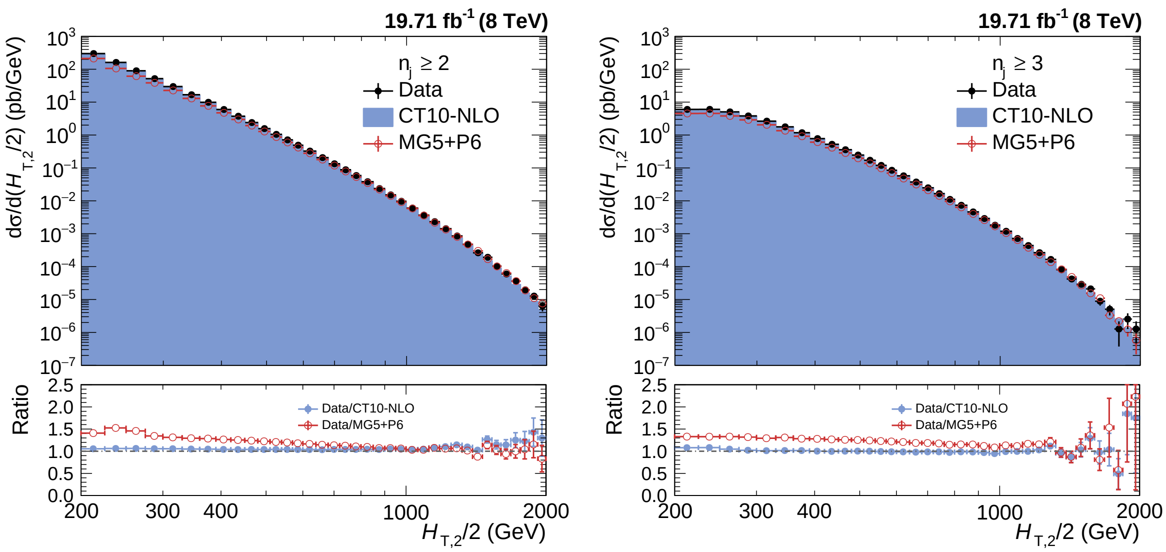

Figure 5.7: The differential cross-sections are compared for data (black solid circles) and LO MadGraph5+pythia6 (MG5+P6) Monte Carlo (red empty circles), at reconstructed level with CT10-NLO theory predictions (blue histogram), as a function of $H_{\mathrm{T},2}/2$ for inclusive 2-jet (left) and 3-jet events (right). Ratios of data to the Monte Carlo predictions (red line) as well as to the CT10-NLO predictions (blue line) are shown in bottom panel of each plot.

The ratio of differential cross-sections, R_{32} as a function of $H_{\mathrm{T},2}/2$, is extracted by dividing the cross-section of selected inclusive 3-jet events to that of inclusive 2-jet events at any given bin size of $H_{\mathrm{T},2}/2$. In the cross-section ratios, the numerator and denominator are not independent samples. So to calculate the

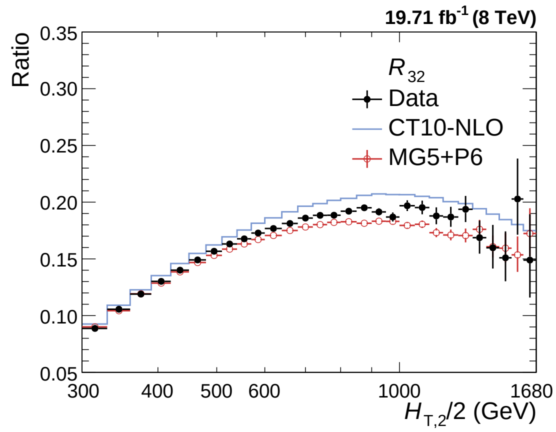

Figure 5.8: Comparison of the cross-section ratio R_{32} as a function of $H_{\mathrm{T},2}/2$, for data (black solid circles) and LO MadGraph5+pythia6 (MG5+P6) Monte Carlo (red empty circles), at reconstructed level with CT10-NLO theory predictions (blue line). The error bars give the asymmetrical statistical uncertainty, calculated by the Wilson score interval method which takes into the account the correlation between the numerator and denominator.

statistical uncertainty for the cross-section ratios at reconstructed level, the Wilson score interval method is used which takes into account the correlation between the numerator and the denominator and give asymmetric errors. Figure 5.8 shows the comparison of the cross-section ratio R_{32} as a function of $H_{\mathrm{T},2}/2$, for data (black solid circles) and LO MadGraph5+pythia6 (MG5+P6) Monte Carlo (red empty circles), at reconstructed level with CT10-NLO theory predictions (blue line). Since in $\mathrm{n_j} \geq 3$ events, the enough statistics for differential cross-section is available upto 1680 GeV of $H_{\mathrm{T},2}/2$ only, R_{32} is also studied in the range 300 GeV $\leq H_{\mathrm{T},2}/2 <$ 1680 GeV. The bin-wise inclusive 2-jet and 3-jet events differential cross-sections as well as their ratio R_{32}, calculated at detector level, along with statistical uncertainty (in %) are tabulated in Table A.1.

5.4 Jet Energy Resolution (JER)

In an ideal experiment, the value of a physical quantity would be determined exactly with an infinite precision. For e.g. whenever a particle with energy E passes an ideal calorimeter having infinite resolution, the measured energy should always be equal to E. But in real world, the measured energy of the above mentioned particle might differ from the value E. This difference of the measured quantity from its true value may be due to detector noise, uncertainties in the calibration, non-linearity of the response etc. Hence this results in the finite value of the resolution of the detector known as jet energy resolution (JER). In such case, the measured values of energy of different particles, passing through the same detector with same energy E, will be different. Such measurements are described by a Gaussian distribution which is centered around the true value of the measured quantity and its width is generally interpreted as detector resolution. Hence the importance of the detector resolution lies in the fact that it indicates how much the measured value of the observable differs from the true one i.e. how precisely a physical observable can be measured. The narrower the distribution, the higher the resolution is and hence the more efficient is the detector.

Due to finite resolution of the CMS detector, the measured transverse momentum of jets gets smeared. Since the observable in this study i.e. $H_{\mathrm{T},2}/2$ is the average sum of transverse momentum of leading and sub-leading jets, the resolution of the detector has to be studied in terms of the observable. CMS detector simulation based on MG5+P6 MC event generators is used to determine the resolution as both the particle and reconstructed level information is available. The jets clustered from stable generator particles called Gen jets as well as from particle flow candidates reconstructed from the simulated detector output called Reco jets, are used. The studies of the JETMET working group at CMS has shown that the jet energy resolution in data is actually worse than in simulation [26]. So the reconstructed jet transverse momentum needs to be smeared additionally to match the resolution in data. Table 5.5 shows the scaling factors (c) which need to be applied on the transverse momentum of simulated reconstructed jets. The scaling factors depend on the absolute η of the jet. The uncertainty on these measured scaling factors ($c_{central}$) needs to be taken into account in a physics analysis. This is done by smearing the reconstructed jets with two additional sets of scaling factors, c_{up}

and c_{down}, that correspond to varying the factors up and down respectively, by one sigma and evaluating the impact of these new sets.

Table 5.5: JETMET working group at CMS has shown that the jet energy resolution in data is actually worse than in simulation [26]. To match the resolution in data, the reconstructed jet transverse momentum in simulated events need to be smeared by applying the scale factors. The uncertainty on the resolution is given by an upwards and downwards variation c_{up} and c_{down} of the measured scaling factor $c_{central}$.

η	0.0 - 0.5	0.5 - 1.1	1.1 - 1.7	1.7 - 2.3	2.3 - 2.8
$c_{central}$	1.079	1.099	1.121	1.208	1.254
c_{down}	1.053	1.071	1.092	1.162	1.192
c_{up}	1.105	1.127	1.150	1.254	1.316

The reconstructed jet p_{T} is smeared randomly using a Gaussian width widened by the scaling factor ($c_{central}$)

$$p_{\mathrm{T}} \rightarrow Gauss\left(\mu = p_{\mathrm{T}}, \sigma = \sqrt{c^2_{central} - 1} \cdot \mathrm{JER}(p_{\mathrm{T}})\right) \tag{5.6}$$

where $\mathrm{JER}(p_{\mathrm{T}})$ is the resolution determined as a function of jet p_{T} using MG5+P6 MC simulated events. After smearing transverse momentum of each reco jet, $H_{\mathrm{T},2}/2$ is calculated from both generator particle jets (Gen $H_{\mathrm{T},2}/2$) as well as the particle flow or reconstructed jets (Reco $H_{\mathrm{T},2}/2$). Then the response is calculated as defined in the Eq. 5.7.

$$R = \frac{\text{Reco } H_{\mathrm{T},2}/2}{\text{Gen } H_{\mathrm{T},2}/2} \tag{5.7}$$

The width of the response distribution in a given Gen $H_{\mathrm{T},2}/2$ bin is interpreted as the resolution which in good approximation can be described by the σ of a Gaussian fit of the response distribution. A double-sided Crystal-Ball function takes into account the non-Gaussian tails of the jet response distribution. The resolution as a function of $H_{\mathrm{T},2}/2$ is calculated separately for both $\mathrm{n_j} \geq 2$ and $\mathrm{n_j} \geq 3$ events.

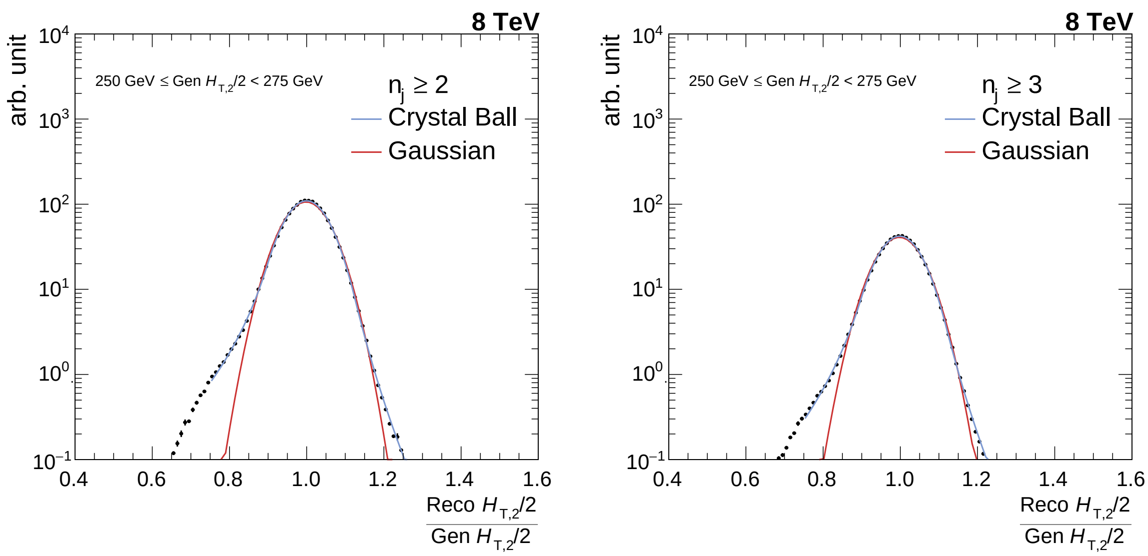

Figure 5.9: Fitting of the resolution distribution, obtained using LO MadGraph5+pythia6 (MG5+P6) Monte Carlo simulated events, as a function of $H_{\mathrm{T},2}/2$ for inclusive 2-jet (left) and 3-jet events (right). The blue line shows the double-sided Crystal Ball function fit of $\frac{\text{Reco } H_{\mathrm{T},2}/2}{\text{Gen } H_{\mathrm{T},2}/2}$ in each Gen $H_{\mathrm{T},2}/2$ bin, overlayed by Gaussian fitting the core of the resolution (red line).

A fit example for one Gen $H_{\mathrm{T},2}/2$ bin is shown in Fig. 5.9 for $\mathrm{n_j} \geq 2$ (left) and 3-jet events (right). Here the black dots represent the jet response distribution and the double-sided Crystal-Ball fit (blue line) is overlayed by the Gaussian fit (red line). The resolution in each Gen $H_{\mathrm{T},2}/2$ bin is then plotted as a function of Gen $H_{\mathrm{T},2}/2$.

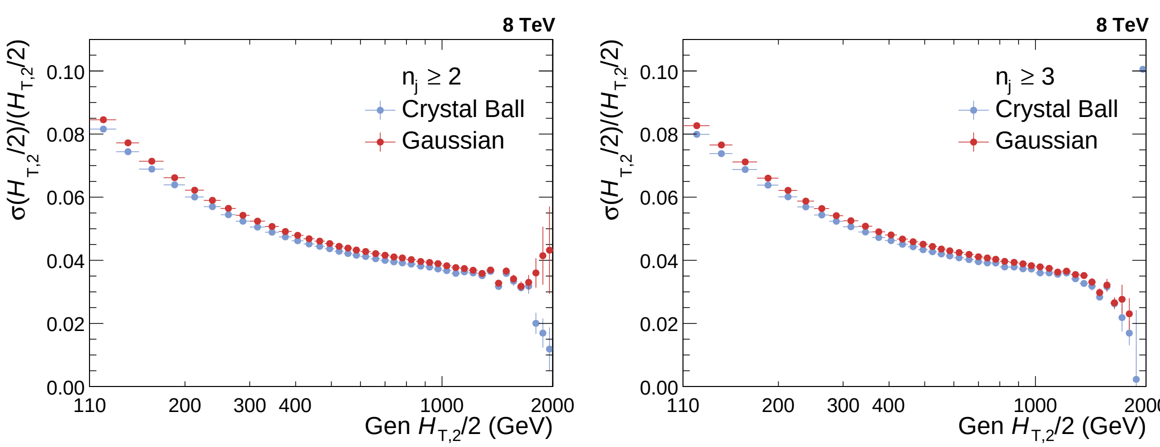

Figure 5.10: Comparison of jet energy resolution calculated using Crystal-Ball fit function (blue solid circles) and Gaussian fit function (red solid circles) for inclusive 2-jet (left) and 3-jet events (right).

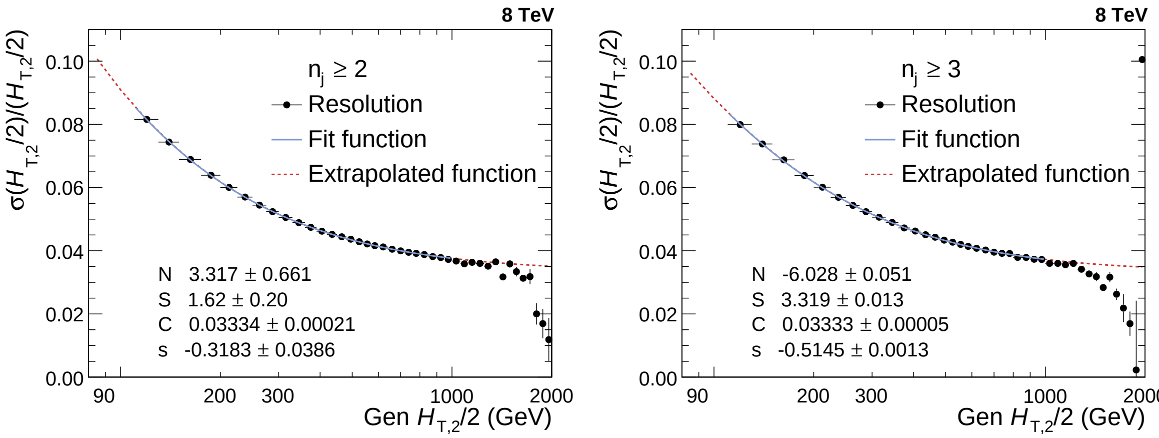

Figure 5.11: Jet energy resolution (JER) is shown as a function of Gen $H_{\mathrm{T},2}/2$ for inclusive 2-jet (left) and 3-jet events (right). JER (black solid circles) is fitted by using the modified NSC-formula (blue solid line) which is extrapolated to 80 GeV and upto 2000 GeV (red dashed line) to consider the migration into lower as well as higher bins.

As expected, it has been observed from Fig. 5.10 that the Crystal Ball function (blue solid circles) describes the measured distributions better as compared to Gaussian function fit (red solid circles), especially in the low-$H_{\mathrm{T},2}/2$ region where the non-Gaussian tails are more pronounced. Hence JER is determined using Crystal Ball function fit. Figure 5.11 shows the final relative jet energy resolution (JER) which is described by a modified version of the NSC formula (blue solid line) [27], as mentioned in Equation 5.8. To consider the migration to lower as well higher bins and to obtain the resolution with reasonable statistics over the full range of Gen $H_{\mathrm{T},2}/2$, the fit function is extrapolated to 80 GeV and upto 2000 GeV which is shown by red dashed line. The fit formula used here is basically the usual NSC formula which describes the resolution in terms of noise N originating due to electronic and pileup noise and is independent of $H_{\mathrm{T},2}/2$; a stochastic component S due to sampling fluctuation and EM fraction fluctuation per hadrons; and a constant term C because of dead material, magnetic field and calorimeter cell to cell fluctuation. In the low $H_{\mathrm{T},2}/2$ region the tracking has a non-negligible influence on the resolution due to the particle flow algorithm, so the additional parameter s is introduced to obtain slightly better fits. The parameters obtained after fitting the relative resolution using the above mentioned NSC formula are tabulated in Table 5.6 for $n_j \geq 2$ and $n_j \geq 3$ events. This calculated JER is used in unfolding procedure to smear the generated truth spectrum which is used as input in getting the response matrices and is explained in details in Sec. 5.5.1. Since JER in $n_j \geq 2$ events is similar to that one in $n_j \geq 3$ events, so N, S and C fit parameters obtained for $n_j \geq 3$ events are used for unfolding R_{32}.

$$\frac{\sigma(x)}{x} = \sqrt{sgn(N) \cdot \frac{N^2}{x^2} + S^2 \cdot x^{s-1} + C^2} \tag{5.8}$$

Table 5.6: The parameters obtained by fitting the relative resolution as a function of $H_{\mathrm{T},2}/2$, using the modified NSC formula, for inclusive 2-jet and 3-jet events.

	N	S	C	s
Inclusive 2-jet	3.32	1.62	0.0333	-0.318
Inclusive 3-jet	-6.03	3.32	0.0333	-0.515

Since the JER is calculated using MG5+P6 Reco and Gen $H_{\mathrm{T},2}/2$ distributions, so it is expected that if Gen $H_{\mathrm{T},2}/2$ is smeared using this JER, it should match the Reco $H_{\mathrm{T},2}/2$. But this extracted JER in one large rapidity bin, smears the Gen $H_{\mathrm{T},2}/2$ too much because Smeared Gen/Gen ratio (red line) shows a discrepancy from simulated Reco/Gen ratio (blue line), as observed in Fig. 5.12 for $n_j \geq 2$ (left) and $n_j \geq 3$ events (right). Some shortcomings in the detector simulation of the theory spectra leads to these small nonclosures. When the 30% reduced JER is used to smear Gen, then the ratio Smeared Gen/Gen (pink line) matches with simulated Reco/Gen ratio (blue line) within the statistical fluctuations. Hence an additional unfolding uncertainty is attributed by comparison to 30% reduced JER for both $n_j \geq 2$ and $n_j \geq 3$ events. Due to high statistical fluctuations at high $H_{\mathrm{T},2}/2$, range is presented upto 1680 GeV only.

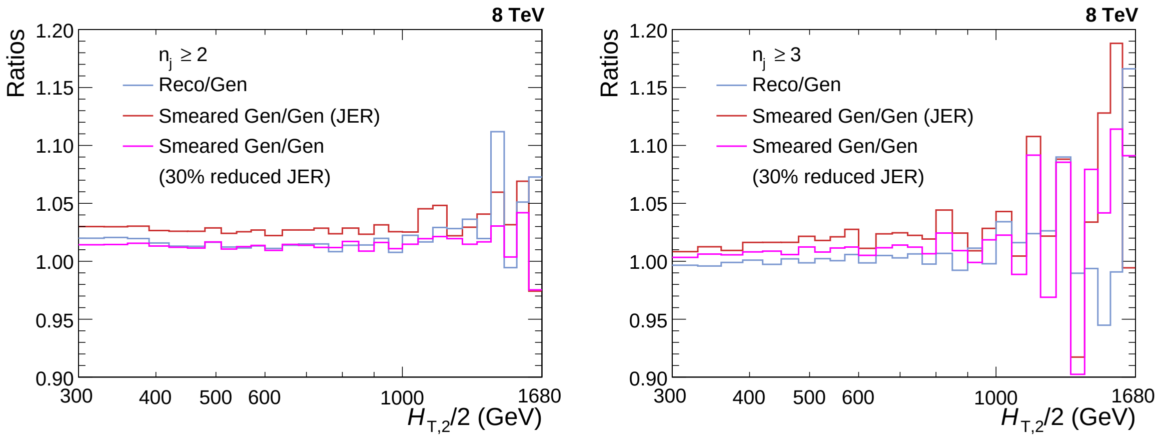

Figure 5.12: MadGraph5+pythia6 (MG5+P6) Gen smeared using extracted jet energy resolution (JER) shows a discrepancy from simulated Reco as Smeared Gen/Gen ratio (red line) does not match with Reco/Gen ratio (blue line), for both inclusive 2-jet (left) and 3-jet events (right). Smeared Gen/Gen ratio (pink line) where Gen is smeared using 30% reduced JER matches with simulated Reco/Gen ratio (blue line) within the statistical fluctuations. Hence an additional unfolding uncertainty is attributed by comparison to 30% reduced JER.

5.5 Unfolding

One of the main goals in an experimental measurement is to do the comparison of data with theory predictions or with the results obtained from other experiments. But the finite resolution of a detector and the steeply falling jet p_T spectrum distorts the physical quantities. As a result, the measured observables are different from their corresponding true values. Each p_T bin content contains the migrated events from neighbouring bins along with the original events. So an unfolding process of the data should be followed in order to remove detector effects. In this analysis, the measurements are corrected for detector smearing effects and unfolded to stable particle level by using the iterative D′Agostini Bayesian algorithm [28, 29] as implemented in RooUnfold software package [30]. In this algorithm, the number of iterations regularize the unfolding process. The obtained distribution in one iteration is taken as the input in the next one. χ^2 between two successive iterations is given by Eq. 5.9. The number of iterations stop when χ^2/N_{bins} is < 1. A reduced χ^2 is obtained by a higher number of iterations but this will also increase the uncertainty and there are larger bin-by-bin fluctuations and correlations. So the optimization of number of iterations is very important. In the current analysis, unfolding done with "four" iterations gives the best results with low χ^2 and low bin-by-bin correlations.

$$\chi^2 = \sum_{i=1}^{N_{bins}} \left(\frac{n_i^{j+1} - n_i^j}{\sqrt{n_i^j}} \right)^2 \tag{5.9}$$

where n_i^j number of events in i-th bin for j-th iteration

The measured differential cross-sections as a function of $H_{\mathrm{T},2}/2$, are unfolded separately for $\mathrm{n_j} \geq 2$ and $\mathrm{n_j} \geq 3$ events. The measured cross-section ratio R_{32} is also corrected for detector smearing effects and unfolded to particle level. There can be two ways to obtain unfolded cross-section ratio :

- **Method I :** First unfold separately the inclusive 2-jet and 3-jet measured cross-sections and then construct the ratio R_{32}
- **Method II :** Unfold directly the cross-section ratio R_{32}

In further analysis, unfolded cross-section ratio R_{32} and its systematic uncertainties are calculated using Method I, whereas Method II is used only to propagate the statistical uncertainties including bin-by-bin correlations and statistical correlations between the inclusive 3-jet and 2-jet events cross-sections. Unfolding takes the response matrix as an input which are explained in the next section.

5.5.1 Response Matrices

The response matrix is a two dimensional mapping between the true and measured distributions. It is usually derived from simulated Monte Carlo (MC) samples, which takes the true distribution from MC as an input and smears it by taking into account the detector resolution. Then this response matrix is used to unfold the measured data spectrum. But there are several drawbacks of constructing response matrix using this method. In some phase space regions, the shape of the distribution is not well described by the LO predictions. Also, the limited number of events in the MC samples at high transverse momenta introduces high statistical fluctuations in the response matrix.

However, there is an indirect way of constructing the response matrix which uses a custom Toy Monte Carlo method. In this method, the particle level or true $H_{\mathrm{T},2}/2$ spectrum is obtained by fitting the theoretically predicted NLO spectrum. Then this distribution is smeared with forward smearing technique, using the extracted jet energy resolution (JER) to obtain the reconstructed level or measured $H_{\mathrm{T},2}/2$ spectrum. After that, the response matrix is constructed from these two distributions is used for the unfolding procedure.

5.5.1.1 Inclusive Cross-sections

The NLO spectrum of the differential cross-sections for $\mathrm{n_j} \geq 2$ and $\mathrm{n_j} \geq 3$ events obtained using CT10-NLO PDF set are fitted with the following two different functions defined in Eq. 5.10 and 5.13. These functions describes the shape as well as normalization of the distribution.

- **Function I :**

$$f(H_{\mathrm{T},2}/2) = N[x_T]^{-a}[1 - x_T]^b \times exp[-c/x_T] \tag{5.10}$$

where N is normalization factor and a, b, c are fit parameters.

This function is derived from the below function [31] :

$$f(p_T;\alpha,\beta,\gamma) = N_0[p_T]^{-\alpha}\left[1 - \frac{2\;p_T\;cosh(y_{min})}{\sqrt{s}}\right]^{\beta} \times exp[-\gamma/p_T] \tag{5.11}$$

using

$$\alpha = a, \quad \beta = b, \quad \gamma = c * \sqrt{s}/2, x_T = \frac{2 * H_{\mathrm{T},2}/2 * cosh(y_{min})}{\sqrt{s}} = \frac{2 * H_{\mathrm{T},2}/2}{\sqrt{s}} \tag{5.12}$$

where transverse scaling variable x_T corresponds to the proton fractional momentum x for dijets with rapidity $y = 0$, $\sqrt{s} = 8000$ GeV and y_{min} is low-edge of the rapidity bin y under consideration (here y_{min} is taken equal to 0)

- **Function II :**

$$f(H_{T,2}/2) = A_0\Big(1 - \frac{H_{T,2}/2}{A_6}\Big)^{A_7} \times 10^{F(H_{\mathrm{T},2}/2)}, \text{where} \quad F(x) = \sum_{i=1}^{5} A_i \Big(log(\frac{x}{A_6})\Big)^i \tag{5.13}$$

where the parameter A_6 is fixed to $\frac{\sqrt{s}}{2\ cosh(y_{min})}$, where $\sqrt{s} = 8000$ GeV and y_{min} is the minimum rapidity. The other parameters are derived from the fitting.

Figure 5.13 shows the fitted CT10-NLO spectrum of differential cross-section as a function of $H_{\mathrm{T},2}/2$ (green solid circles) using Function I (top) and using Function II (bottom) : for inclusive 2-jet (left) and 3-jet events (right). Function I is used primarily to generate response matrices and perform the closure tests and Function II is used as an alternative function to calculate unfolding uncertainty, described in Sec. 5.6.3. To include the migration to lower bins, the fit functions described by red lines are extrapolated to 80 GeV (blue dashed lines).

A flat $H_{\mathrm{T},2}/2$ spectrum is generated by using toy Monte Carlo events and the fit parameters obtained from the NLO spectrum using function I (as shown in Fig. 5.13) provides weights to the flat spectrum. A total of ten million events are generated randomly (in $H_{\mathrm{T},2}/2$ range 80-2000). These generated values are then smeared with a Gaussian function, where σ of the Gaussian is determined from the relative resolution

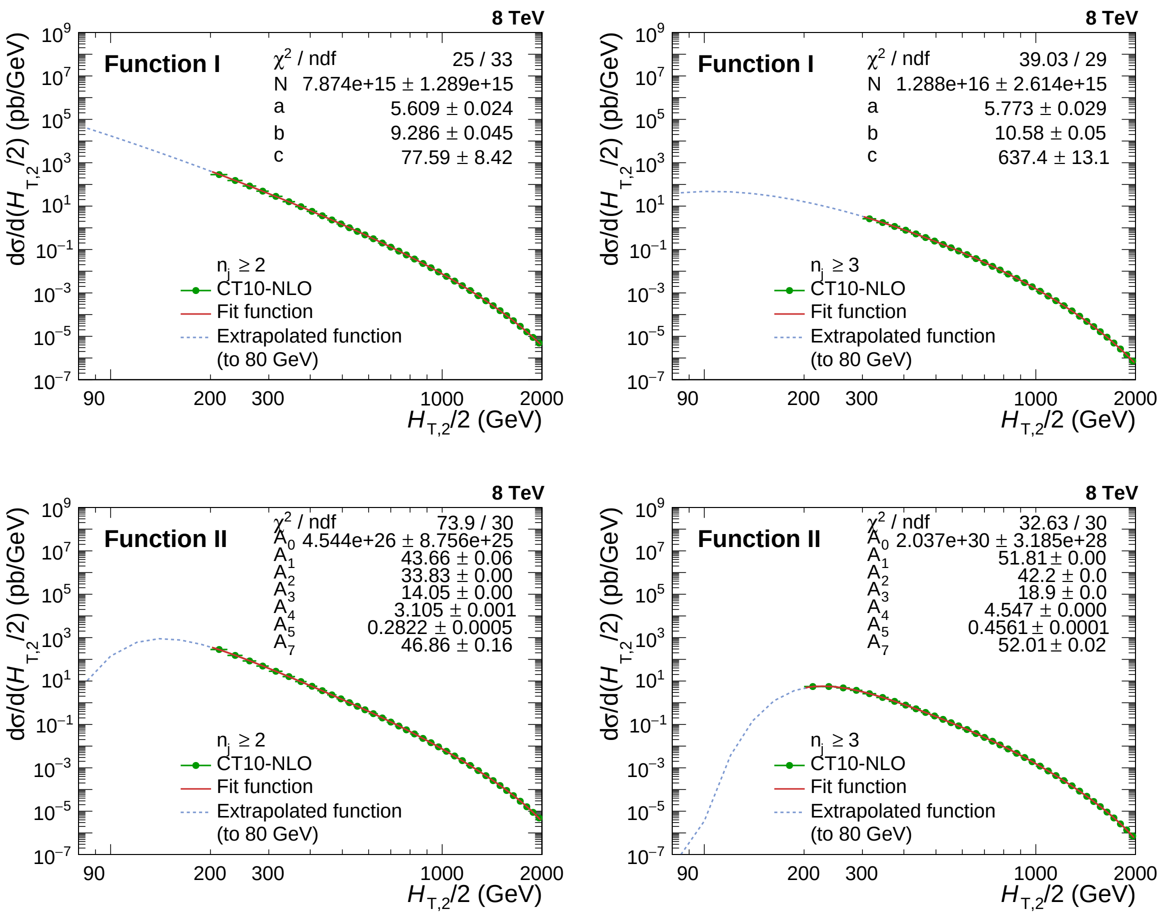

Figure 5.13: Fitted CT10-NLO spectrum of differential cross-section as a function of $H_{T,2}/2$ (green solid circles) using Function I (top) defined in Eq. 5.10 and using Function II (bottom) given by Eq. 5.13, for inclusive 2-jet (left) and 3-jet events (right). To consider the migration to lower $H_{T,2}/2$ bins, the fit functions described by red lines are extrapolated to 80 GeV (blue dashed lines).

parametrization as a function of $H_{T,2}/2$ calculated from NSC formula mentioned in equation 5.8. The parameters N, S, C used for smearing are taken from Table 5.6. These randomly generated ($\mathrm{Gen_{Toy}}$) and smeared ($\mathrm{Measured_{Toy}}$) values are used to fill the response matrices. Figure 5.14 shows the response matrices derived using the Toy MC for $n_j \geq 2$ (left) and $n_j \geq 3$ events (right). The matrices are normalized to the number of events in each column. The response matrices are diagonal as the migrations in off-diagonal bins are much smaller than the bins along the diagonal.

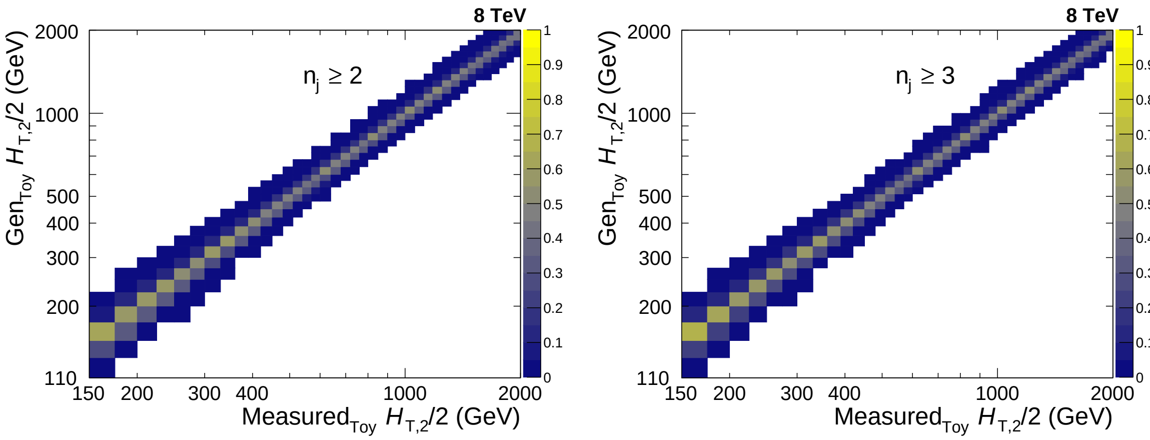

Figure 5.14: The response matrices are derived using the Toy Monte Carlo and forward smearing method, for inclusive 2-jet (left) and 3-jet events (right). The matrices are normalized to the number of events in each column and are diagonal with small off-diagonal migrations between close-by $H_{\mathrm{T},2}/2$ bins.

5.5.1.2 Cross-section Ratio, R_{32}

To obtain the statistical uncertainty on the unfolded cross-section ratio R_{32}, Method II is used. In this method, the response matrix is constructed using Toy MC method as done in Sec. 5.5.1.1 for differential cross-sections. To obtain the true spectrum for R_{32}, the ratio of cross-section spectrum described by Eq. 5.10 for inclusive 3-jet to that of 2-jet events is taken. This ratio is shown by green solid circles in Fig. 5.15 (left) which is fitted using a polynomial function of degree 8 (red line). Then as explained in above section, response matrix is derived for R_{32} using the Toy Monte Carlo and forward smearing method which is shown in Fig. 5.15 (right). The matrix is normalized to the number of events in each column and is diagonal with small off-diagonal migrations between close-by $H_{\mathrm{T},2}/2$ bins.

5.5.2 Closure Test

A closure test has been performed to confirm the working of the unfolding procedure. In this test, $\mathrm{Measured}_{\mathrm{Toy}}$ spectrum is unfolded using the constructed response matrices shown in Figure 5.14. It is expected that the same $\mathrm{Gen}_{\mathrm{Toy}}$ spectrum should be re-obtained after unfolding. Figure 5.16 confirms that the unfolded $\mathrm{Measured}_{\mathrm{Toy}}$

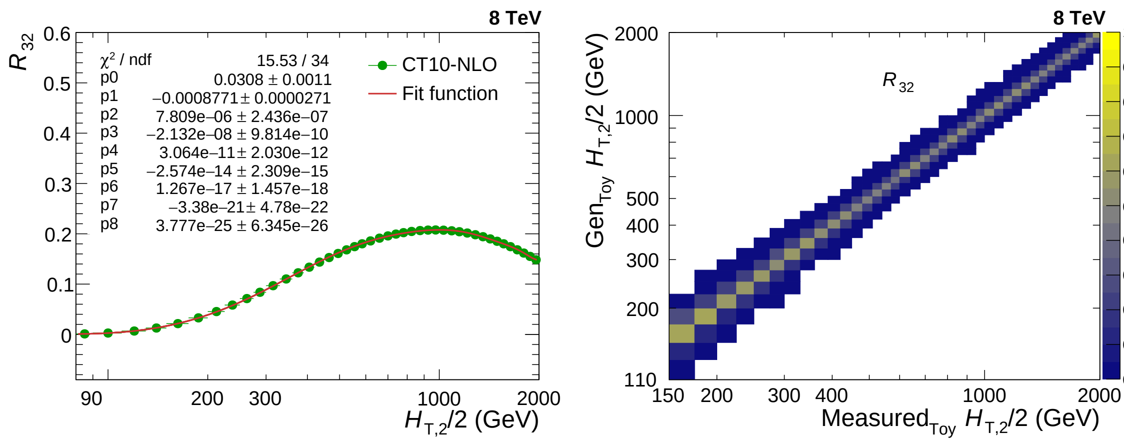

Figure 5.15: Left : The ratio of cross-sections described by Eq. 5.10 for inclusive 3-jet to that of 2-jet events is shown as a function of $H_{\mathrm{T},2}/2$ (green solid circles). It is fit using a polynomial function of degree 8 (red line). Right : The response matrix is derived using the Toy Monte Carlo and forward smearing method, for the cross-section ratio R_{32}. The matrix is normalized to the number of events in each column and is diagonal with small off-diagonal migrations between close-by $H_{\mathrm{T},2}/2$ bins.

spectrum matches exactly with $\mathrm{Gen_{Toy}}$ spectrum as the ratio of these distributions is perfectly flat at one for both $\mathrm{n_j} \geq 2$ (top left) and $\mathrm{n_j} \geq 3$ events (top right) cross-sections as well as the cross-section ratio R_{32} (bottom).

For another closure test, Reco MG5+P6 MC differential cross-section distribution is unfolded using the above constructed response matrices using JER for forward smearing the randomly generated spectrum. While taking ratio of the unfolded distribution to that of Gen MG5+P6 MC, it is observed that a well closure is not obtained. This is represented by blue line in Fig. 5.17 for $\mathrm{n_j} \geq 2$ (top left) and $\mathrm{n_j} \geq 3$ events (top right). As observed in Fig. 5.12 in Sec. 5.4, if Reco MG5+P6 MC is unfolded using the response matrices obtained using 30% reduced JER, then the good closure is obtained as shown by red line in Fig. 5.17. Since unfolded cross-section ratio R_{32} is the ratio of unfolded differential cross-sections (Method I), same behaviour is observed for R_{32} (bottom).

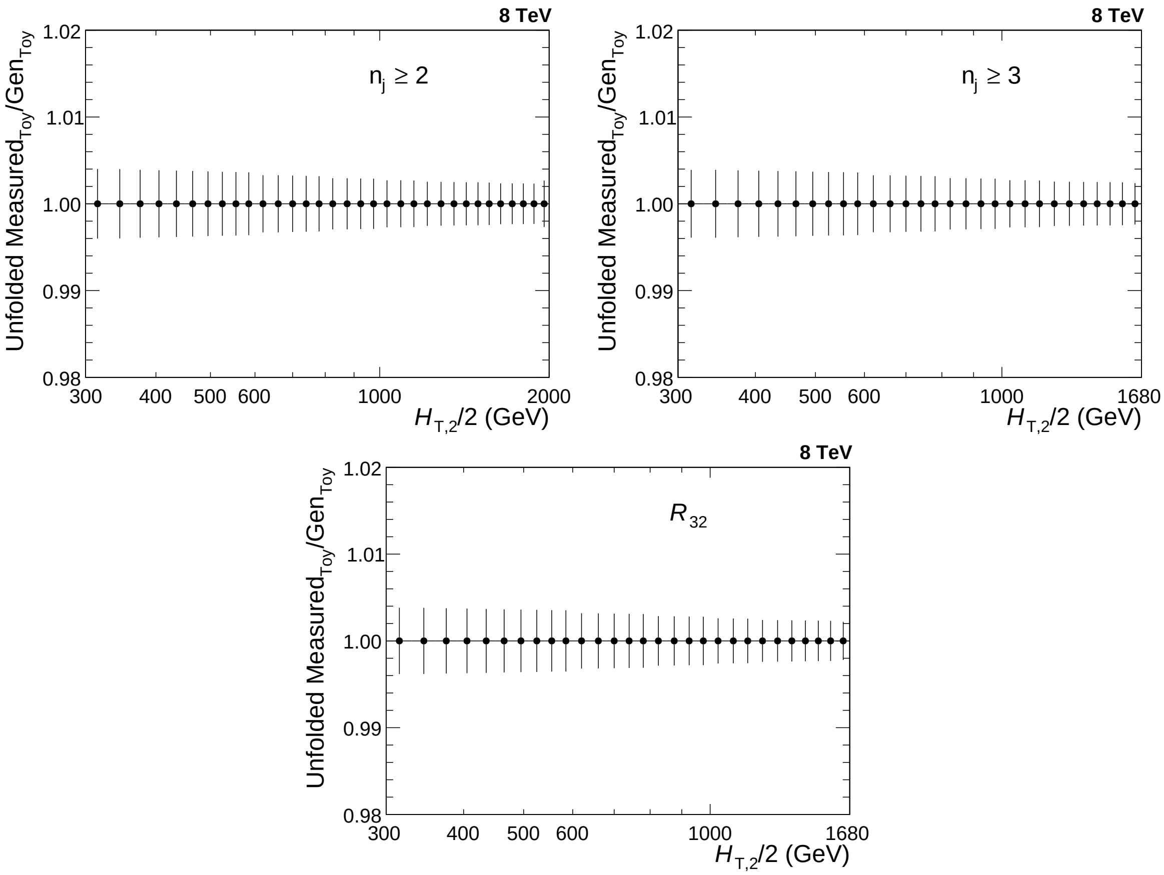

Figure 5.16: Closure test of the unfolding technique where the smeared spectrum obtained from Toy Monte Carlo method (Measured$_{\rm Toy}$), is unfolded using the constructed response matrices (obtained by forward smearing the randomly generated spectrum (Gen$_{\rm Toy}$) using extracted jet energy resolution (JER)). As expected, the unfolded measured$_{\rm Toy}$ spectrum matches exactly with Gen$_{\rm Toy}$ spectrum as the ratio of these distributions is perfectly flat at one for both inclusive 2-jet (top left) and 3-jet events (top right) cross-sections as well as the cross-section ratio R_{32} (bottom).

5.5.3 Unfolding of the Measurement

After validity the unfolding method, the measured differential cross-sections as well as R_{32} are unfolded using the above reconstructed response matrices. The unfolded data spectrum is compared to that of measured one in Fig. 5.18 for $\rm n_j \geq 2$ (top left) and $\rm n_j \geq 3$ events (top right) cross-sections and for the cross-section ratio R_{32} (bottom). As already discussed that 30% reduced JER gives better closures than JER, so the unfolding of data is done with response matrices using JER (blue solid circles) as well as 30% reduced JER (red solid circles) for smearing. The difference

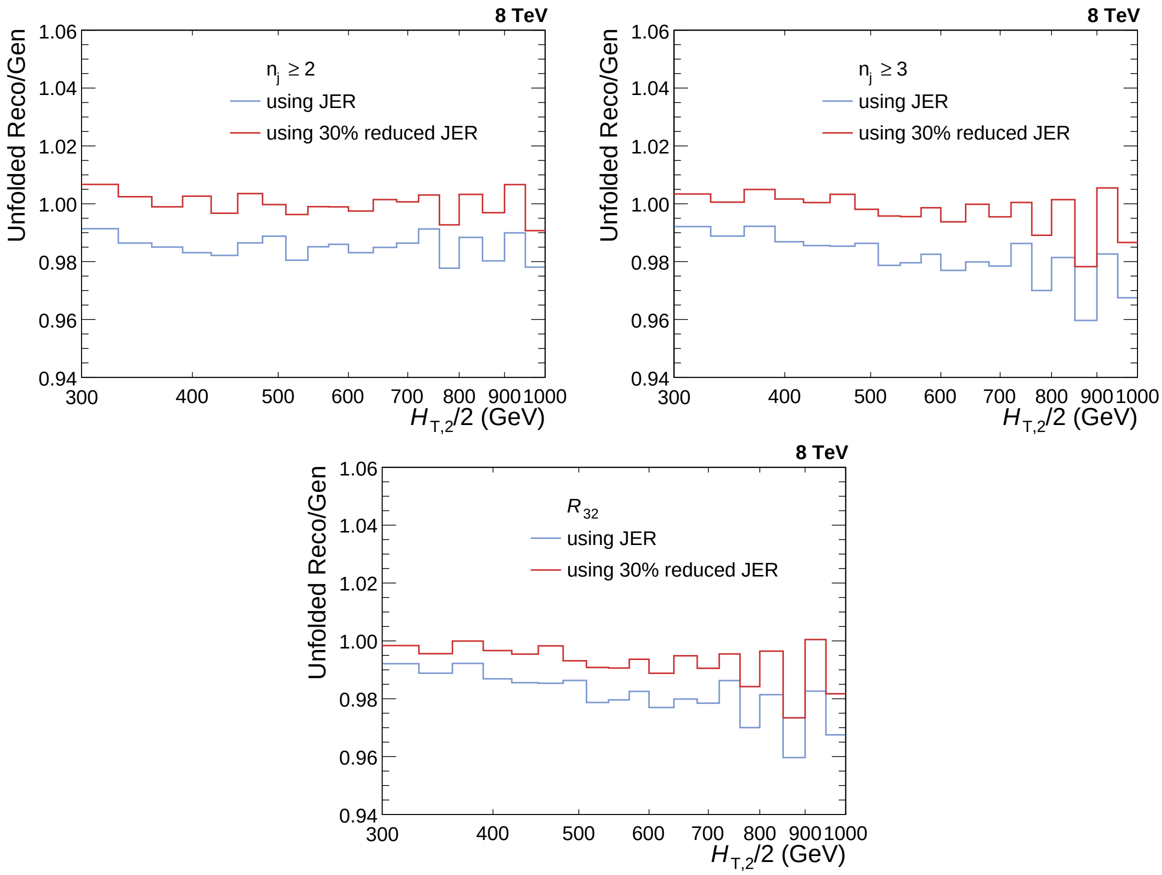

Figure 5.17: Reco MadGraph5+pythia6 Monte Carlo (MG5+P6 MC) differential cross-section distributions unfolded with the response matrices (obtained by forward smearing the randomly generated spectrum (Gen) using extracted jet energy resolution (JER)), does not give a good closure with Gen MG5+P6 MC (blue line), for inclusive 2-jet (top left) and 3-jet events (top right). After performing the unfolding using 30% reduced JER, a good closure is obtained (red line). Since unfolded the cross-section ratio R_{32} is the ratio of unfolded differential cross-sections, same behaviour is observed for R_{32} (bottom).

between both is taken as an additional uncertainty on the unfolded measurement.

5.6 Experimental Uncertainties

In an experimental measurement of any physical observable, the uncertainties play a key role and hence are important to study in a physics analysis. The uncertainties can be categorized into two types : statistical and systematic. The statistical uncertainties arise due to random fluctuations depending on the number of events.

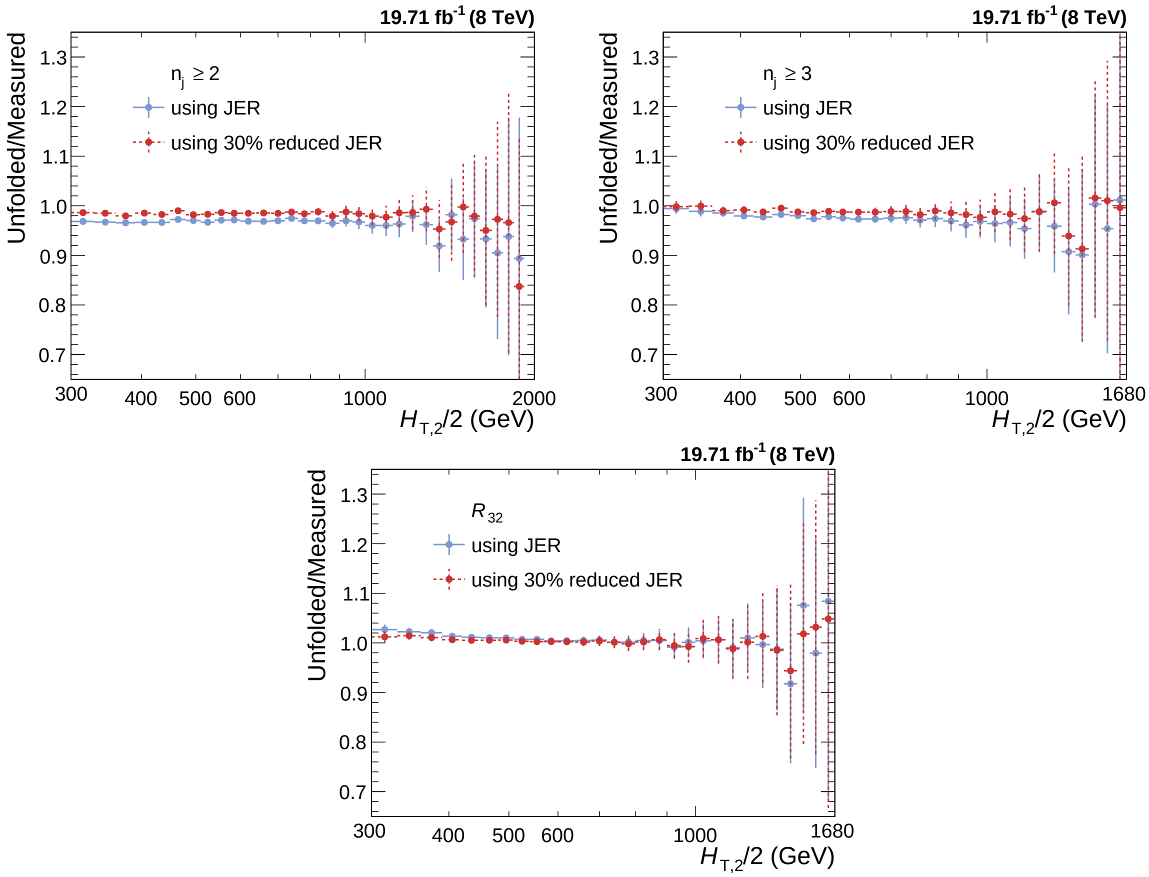

Figure 5.18: The measured differential cross-sections as well as the cross-section ratio R_{32} are unfolded as a function of $H_{\mathrm{T},2}/2$ using the response matrices derived using the Toy Monte Carlo and forward smearing method. The unfolded spectrum are compared with that of the measured one for inclusive 2-jet (top left) and 3-jet events cross-sections (right) as well as for R_{32} (bottom). The unfolding is done with response matrices using JER (blue solid circles) as well as 30% reduced JER (red solid circles) for smearing. The difference between both is taken as an additional uncertainty on the unfolded measurement.

The more the number of events, less is the statistical uncertainty. The systematic uncertainties may be due to known detector effects, model dependence, assumptions made or various corrections applied. In general, if the statistical and systematic uncertainties are uncorrelated, these can be added in quadrature to obtain the total uncertainty on the measurement. In this section, all the experimental uncertainties affecting the measurement of cross-sections and the cross-section ratio R_{32} are described. The systematic experimental uncertainties for R_{32} are propagated from the cross-sections to the ratio taking into account correlations. Due to this, the systematic uncertainties may cancel for R_{32} completely or partially as compared to those for the individual cross-sections.

5.6.1 Statistical Uncertainty

Statistical uncertainty on the measurement is obtained through the unfolding procedure using a toy MC method. The measured data points are smeared within their statistical uncertainties to get the smeared spectrum. Such smeared spectrums are produced million in number and the unfolding is performed multiple times for each smeared spectra. The differences between the unfolded spectrums and the measured one give the statistical uncertainty. The unfolding process introduces more statistical fluctuations which can be observed in Fig. 5.19. Here the fractional statistical uncertainties of the unfolded data (red line) are compared with those of the measured one (blue line) for $\mathrm{n_j} \geq 2$ (top left) and $\mathrm{n_j} \geq 3$ events cross-sections (top right) as well as for the cross-section ratio R_{32} (bottom).

After the unfolding, the final statistical uncertainties become correlated among the bins such that the size of these correlations varies between 10 and 20%. The correlation (anti-) is more significant for neighbouring bins in $H_{\mathrm{T},2}/2$ as compared to the far off ones. In Fig. 5.20, the correlations of the statistical uncertainty after the unfolding can be seen for $\mathrm{n_j} \geq 2$ (top left) and $\mathrm{n_j} \geq 3$ events cross-sections (top right) and for the cross-section ratio R_{32} (bottom). These correlations must be considered while performing the fits to extract the value of the strong coupling constant, α_S.

5.6.2 Jet Energy Corrections Uncertainty

As explained in Sec. ?, the measured jet energy is corrected for a variety of detector effects by applying jet energy corrections (JEC) [32]. There are 25 mutually independent sources which contribute to JEC. Each source presents a 1σ shift and is fully correlated in p_{T} and η but uncorrelated to all other sources. The observable is

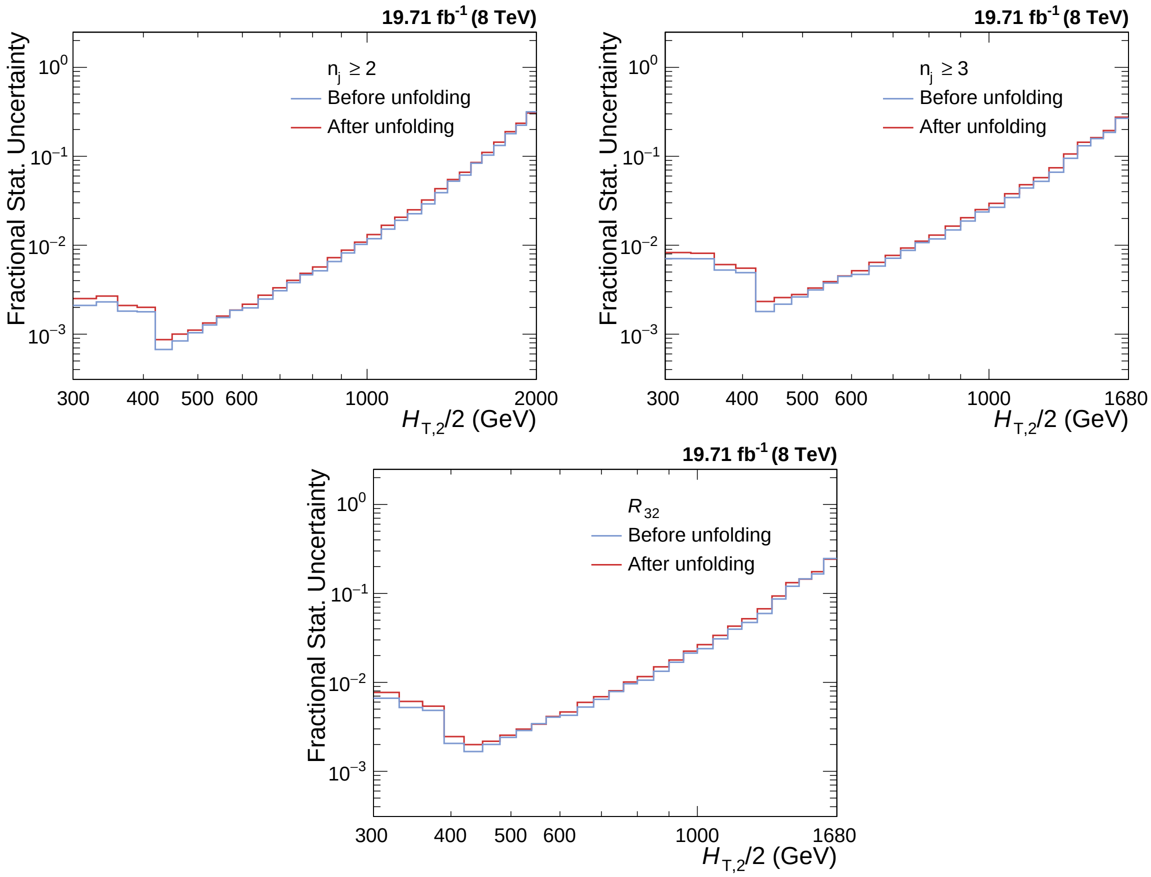

Figure 5.19: The fractional statistical uncertainties of the unfolded data (red line) are compared with those of the measured one (blue line) for inclusive 2-jet (top left) and 3-jet events cross-sections (top right) as well as for the cross-section ratio R_{32} (bottom). After unfolding, the statistical uncertainty increases slightly.

studied with the nominal values of the jet energy which gives nominal distributions as well as by varying up and down the energy of all jets by the uncertainty. The differences between the nominal distributions and the ones obtained by varying the jet energy gives the uncertainties from each source. The JEC uncertainties can be asymmetric in nature which leads to separate treatment of upwards and downwards variation of each source. The sum in quadrature of uncertainties from all sources gives the total JEC uncertainty. In the current analysis, JEC uncertainties are a dominant source of experimental uncertainty at low $H_{\mathrm{T},2}/2$. The JEC uncertainty ranges from 3% to 10% for $\mathrm{n_j} \geq 2$ and from 3% to 8% for $\mathrm{n_j} \geq 3$ events cross-sections measurement. To calculate JEC uncertainty for ratio R_{32}, the inclusive 2-jet and

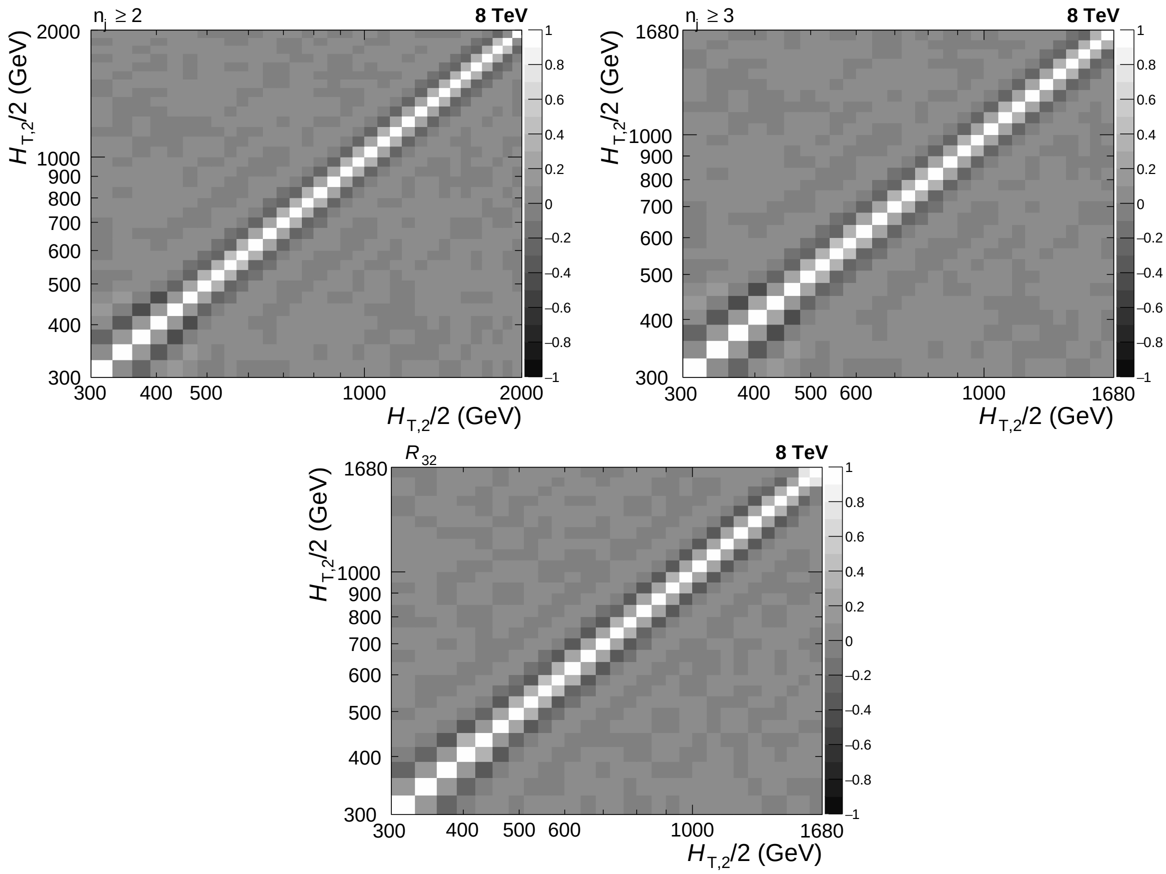

Figure 5.20: The unfolding procedure introduces the correlations of the statistical uncertainty through bin migrations which are shown here for inclusive 2-jet (top left) and and 3-jet events cross-sections (top right) as well as for the cross-section ratio R_{32} (bottom). The correlation (anti-) is more significant between neighbouring bins than far-ff ones.

3-jet events cross-sections are measured as a function of $H_{\mathrm{T},2}/2$ by shifting the jet p_{T} according to the JEC uncertainty for each source of JEC separately. Then the ratio of these cross-sections is taken and the difference of these from the central ratio R_{32}, gives the JEC uncertainty for R_{32}. As expected, JEC uncertainty for R_{32} is small as compared to that for individual cross-sections and is about 1 to 2% over all $H_{\mathrm{T},2}/2$ bins.

The sources of JEC considered in the current measurements are : AbsoluteStat, AbsoluteScale, AbsoluteFlavMap, AbsoluteMPFBias, Fragmentation, SinglePionECAL, SinglePionHCAL, FlavorQCD, RelativeJEREC1, RelativeJEREC2, RelativeJERHF, RelativePtBB, RelativePtEC1, RelativePtEC2, RelativePtHF, RelativeFSR, RelativeStatFSR, RelativeStatEC2, RelativeStatHF, PileUpDataMC, PileUpPtRef, PileUpPtBB, PileUpPtEC1, PileUpPtEC2 and PileUpPtHF. The AbsoluteFlavMap uncertainty is exactly zero for the 8 TeV and can be ignored. For the four sources : RelativeJERHF, RelativePtHF, RelativeStatHF, PileUpPtHF, the JEC uncertainty is exactly zero because of $|y| < 2.5$ cut used in the analysis. So only 20 sources contribute to the total JEC uncertainty. The Figs. A.1-A.3 show the JEC uncertainty from each source separately for inclusive 2-jet (top) and 3-jet events cross-sections (middle) as for cross-section R_{32} (bottom). Depending on the origin of sources, they are categorized into four groups which are described below in brief :

1. **Pileup :** This uncertainty origins from the differences in the transverse momentum between the true offset and the Random Cone method (i.e. essentially difference of pile-up inside and outside of jets), in simulated events. This uncertainty is derived from Z/γ+jet, dijet and multijet data using fit procedure to estimate the residual pileup uncertainty after the calibration.

2. **Relative :** The forward jets are calibrated by the relative η-dependent corrections using dijet events. The main contribution to the uncertainty comes from jet energy resolution (JER), derived by varying JER scale factors up and down by quoted uncertainties and the initial and final state radiation bias corrections.

3. **Absolute :** A global fit to Z/γ+jet and multi-jet events gives the absolute calibration of the jet energy scale. The uncertainties are related to the lepton momentum scale for muons in Z ($\rightarrow \mu\mu$)+jet and the single pion response in the HCAL.

4. **Flavor :** Flavor response differences are studied from simulation by cross-checking the results with quark- and gluon-tagged γ+jet and Z+jet events. These uncertainties are based on PYTHIA6.4 and HERWIG++2.3 differences

propagated through the data-based calibration method.

The details of the jet energy corrections and uncertainties can be found in [33].

5.6.3 Unfolding Uncertainty

The unfolding uncertainty is comprised of three uncertainties which are explained as follows :

1. **Jet Energy Resolution :** The calculation of the jet energy resolution (JER) using simulated MG5+P6 Monte Carlo events is already explained in Sec. 5.4. As mentioned before, the measured jet transverse momentum (p_{T}) in simulated MC events needs to be smeared additionally to match the resolution in data. This smearing is done by using measured scale factors ($c_{central}$) mentioned in Table 5.5. It is recommended by JETMET group that the uncertainty on these measured scaling factors must be taken into account in a physics analysis. Since JER is used in constructing the response matrix which is an input in unfolding procedure, so the uncertainty on scale factors accounts for the unfolding uncertainty. To calculate JER uncertainty, p_{T} is smeared with two additional sets of scale factors corresponding to varying the factors up and down by one sigma, and corresponding $H_{\mathrm{T},2}/2$ is calculated. Then again JER is calculated as a function of $H_{\mathrm{T},2}/2$ using these upwards (c_{up})and downwards (c_{down}) variations of the scaling factors. Alternative response matrices are built using the JER with above variations and the unfolding is performed again. The differences of the obtained unfolded spectrums to the nominal ones accounts for a systematic JER uncertainty.

2. **Model Dependence :** It is explained in Sec. 5.5.1 that to obtain the true $H_{\mathrm{T},2}/2$ spectrum to be used in constructing response matrix using Toy MC method, the fitting of the CT10-NLO predictions is performed with the Function I described in Eq. 5.10. Using the alternative function, Function II given

by Eq. 5.13, for this fitting and then constructing different response matrix, gives the model dependence of the true $H_{\mathrm{T},2}/2$ spectrum. The differences in unfolded distributions using the above mentioned two different response matrices gives the model dependence uncertainty.

3. **Additional Uncertainty :** Small nonclosures observed in Fig. 5.12 introduces a supplementary uncertainty which is attributed by comparison of distributions unfolded using response matrices constructed using JER from simulation with that obtained with a 30% reduced JER.

All the three above mentioned uncertainties are added in quadrature to get the total unfolding uncertainty which increases from about 1% at low $H_{\mathrm{T},2}/2$ up to 2% at the high $H_{\mathrm{T},2}/2$ ends of the cross-sections for both $\mathrm{n_j} \geq 2$ and $\mathrm{n_j} \geq 3$ events. This uncertainty account for about less than 1% for R_{32}.

5.6.4 Luminosity Measurement Uncertainty

The measurement of the luminosity delivered to CMS detector by LHC in the proton-proton collisions in the year of 2012 is done by using the silicon pixel cluster counting method [12]. The uncertainty related to the integrated luminosity measurement is estimated to be 2.5% (syst.) and 0.5% (stat.). This uncertainty propagates directly to any absolute cross-section measurement. Hence, a total systematic uncertainty of 2.6% is considered across all the $H_{\mathrm{T},2}/2$ bins. At low $H_{\mathrm{T},2}/2$, it is similar in size as the one from JEC. This uncertainty cancels completely for R_{32}.

5.6.5 Residual Uncertainty

The small trigger and jet identification inefficiencies account for smaller than 1% uncertainties on the cross-section measurements [34, 35]. Hence, an uncorrelated residual uncertainty of 1% is assumed across all $H_{\mathrm{T},2}/2$ bins for both $\mathrm{n_j} \geq 2$ and

$n_j \geq 3$ events cross-sections whereas for R_{32}, it gets cancel completely.

5.6.6 Total Experimental Uncertainty

After calculating the uncertainties from all the above mentioned sources, the total experimental uncertainty on measurement of cross-sections as well as cross-section ratio R_{32}, is obtained by adding in quadrature the uncertainties from individual sources. The values of uncertainties (in %) from each source as well as total uncertainty, for each $H_{T,2}/2$ bin, are tabulated in Tables A.2, A.3 and A.4 for $n_j \geq 2$ and $n_j \geq 3$ events cross-sections and cross-section ratio R_{32}, respectively. Figure 5.21 shows the experimental uncertainties, from different sources as well as the total uncertainty, affecting the measurement of $n_j \geq 2$ (top left) and $n_j \geq 3$ events cross-sections (top right) and cross-section ratio R_{32} (bottom). The error bars represent the statistical uncertainty obtained after unfolding. The systematic uncertainties due to jet energy corrections (JEC by blue line), luminosity (red dashed line), unfolding (green dashed line) and residual effects (light purple line) are also presented. The uncertainties due to luminosity and residual effects cancel completely in R_{32}. The total uncertainty (black dashed line) on the measurements is asymmetric in nature and dominated by the uncertainty due to the jet energy corrections (JEC) at lower $H_{T,2}/2$ values and by statistical uncertainty at higher $H_{T,2}/2$ values. The experimental uncertainties from each source as well as total uncertainty are also quoted in Table 5.7.

The complete data analysis of the differential inclusive 2-jet and 3-jet events cross-sections as well as their ratio R_{32} has been presented as a function of $H_{T,2}/2$. The measured spectrums after correcting for detector effects through the unfolding procedure, are compared with the next-to-leading order (NLO) pQCD calculations in the next chapter.

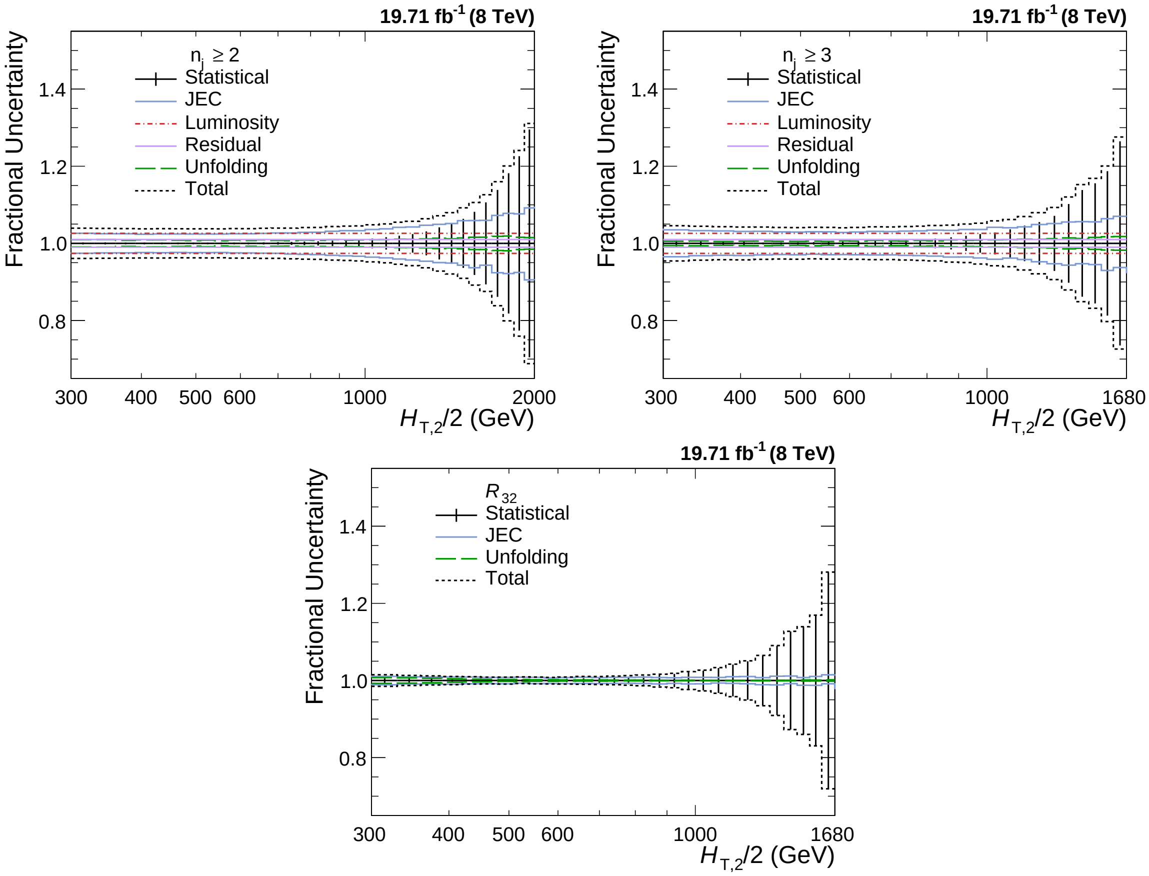

Figure 5.21: Experimental uncertainties from different sources affecting the measurement of cross-sections for inclusive 2-jet (top left) and 3-jet events (top right) and cross-section ratio R_{32} (bottom). The error bars represent the statistical uncertainty after unfolding. The systematic uncertainties due to jet energy corrections (JEC by blue line), luminosity (red dashed line), unfolding (green dashed line) and residual effects (light purple line) are also presented. The uncertainties due to luminosity and residual effects cancel completely in R_{32}. The total uncertainty (black dashed line) is the quadrature sum of the individual sources of uncertainty.

Table 5.7: Overview of all experimental uncertainties affecting the measurement of cross-sections for inclusive 2-jet (left) and 3-jet events (middle) and cross-section ratio R_{32} (right). The uncertainties due to luminosity and residual effects cancel completely in R_{32}. The total uncertainty is the quadrature sum of the individual sources of uncertainty.

Uncertainty Source	**Inclusive 2-jet**	**Inclusive 3-jet**	$\boldsymbol{R_{32}}$
Statistical	$<$ 1 to 30%	$<$ 1 to 27%	$<$ 1 to 28%
Jet energy corrections (JEC)	3 to 10%	3 to 8%	1 to 2%
Unfolding	1 to 2%	1 to 2%	$<$ 1%
Luminosity	2.6%	2.6%	cancels
Residual	1%	1%	cancels
Total	4 to 32%	4 to 28%	1 to 28%

Chapter 6

Theoretical Calculations

In an experiment, the measurements are validated by doing the comparison with the perturbative QCD (pQCD) theoretical calculations. The lowest order (LO) calculations describe well the shapes of the measured distributions but not the normalization due to the dependence on the unphysical renormalization (μ_r) and factorization (μ_f) scales. The next-to-leading order calculations (NLO) improves the precision by reducing the dependence on μ_r and μ_f scales and become an essential feature in the determination of fundamental parameters such as α_S and the parton distribution functions (PDF). This chapter describes the next-to-leading order pQCD calculations used for comparison with the measurements. NLO pQCD calculations need to be corrected for the multiparton interactions (MPI) and hadronization effects by applying non-perturbative (NP) corrections and also for the electroweak interactions (EW).

6.1 Fixed Order NLO Calculations

The predictions of the inclusive differential jet event cross-section at NLO accuracy in pQCD are computed with the NLOJET++ program version 4.1.3 [36, 37]. The results are provided within the framework of FASTNLO version 2.3 [38, 39].

The PDFs are accessed through the LHAPDF6 library [40, 41]. The FASTNLO is preferred over the direct calculation with NLOJET++ because with FASTNLO the calculations of the cross-sections can be repeated several times with different PDFs and scale choices required for calculating the PDF and scale uncertainties. Here the factorization and renormalization scales are chosen equal to $H_{\mathrm{T},2}/2$, i.e. $\mu_f = \mu_r = H_{\mathrm{T},2}/2$.

In the current study, different PDF sets available for a series of different assumptions on the strong coupling constant at the scale of the Z boson mass $\alpha_s(M_Z)$ are used for NLO calculations. Table 6.1 summarizes the already existing PDF sets in LHC Run 1 (upper rows) and the newer PDF sets for Run 2 (lower rows). The different columns list the number of flavours N_f, the assumed masses M_t and M_Z of the top quark and the Z boson, respectively, the default values of $\alpha_s(M_Z)$, and the range in $\alpha_s(M_Z)$ variation available for fits for different PDF sets. All sets uses a variable-flavour number scheme with at most five or six flavours apart from the ABM11 PDFs, which employ a fixed-flavour number scheme with $N_F = 5$. Out of these eight PDF sets the following three are not considered further because of the below mentioned reasons :

- At NLO, predictions based on ABM11 do not describe LHC jet data at small jet rapidity [42–45].
- The HERAPDF2.0 set exclusively fits HERA DIS data with only weak constraints on the gluon PDF.
- The range in values available for $\alpha_s(M_Z)$ is too limited for the NNPDF3.0 set.

Mainly CT10 PDF set is considered for comparison between data and theory predictions as well as for calculating theoretical uncertainties.

Table 6.1: NLO PDF sets are available via LHAPDF6 with various assumptions on the value of $\alpha_s(M_Z)$. The upper rows list the already existing sets in LHC Run 1 and newer ones for Run 2 are listed in lower rows, along with the corresponding number of flavours N_f, the assumed masses M_t and M_Z of the top quark and the Z boson, respectively, the default values of $\alpha_s(M_Z)$, and the range in $\alpha_s(M_Z)$ variation available for fits.

Base set	N_F	M_t (GeV)	M_Z (GeV)	$\alpha_s(M_Z)$	$\alpha_s(M_Z)$ range
ABM11 [46]	5	180	91.174	0.1180	0.110 - 0.130
CT10 [47]	$\leq$5	172	91.188	0.1180	0.112 - 0.127
MSTW2008 [48, 49]	$\leq$5	10^{10}	91.1876	0.1202	0.110 - 0.130
NNPDF2.3 [50]	$\leq$6	175	91.1876	0.1180	0.114–0.124
CT14 [51]	$\leq$5	172	91.1876	0.1180	0.111–0.123
HERAPDF2.0 [52]	$\leq$5	173	91.1876	0.1180	0.110–0.130
MMHT2014 [53]	$\leq$5	10^{10}	91.1876	0.1200	0.108–0.128
NNPDF3.0 [54]	$\leq$5	173	91.2	0.1180	0.115–0.121

6.1.1 NLO Correction Factors

The differences between LO predictions and NLO predictions give the effect of the higher-order contributions to the pQCD predictions. These are described by a NLO correction factor, k-factor, which is derived as the ratio of cross-sections at NLO accuracy to that at LO i.e.

$$\text{k-factor} = \frac{\sigma_{\text{NLO}}}{\sigma_{\text{LO}}} \tag{6.1}$$

The impact of the higher-order corrections is determined by the size of k-factor. The small size of k-factor indicates that the cross-section predictions are precisely described at the LO whereas the larger size hints the contributions from NLO. Figure 6.1 shows the k-factors of the NLOJet++ calculations, for inclusive 2-jet and 3-jet event cross-sections and their ratio R_{32}, using five different PDF sets. k-factor for R_{32} is obtained by taking the ratio of k-factors for inclusive 3-jet event cross-sections to that of inclusive 2-jet. The k-factors are similar for all the PDF sets in the lower region, but the differences increase in regions with larger $H_{\mathrm{T},2}/2$. It is observed that for inclusive 3-jet event cross-sections, k-factor jumps at lowest

$H_{\mathrm{T},2}/2$. This is because some jet configurations are kinematically forbidden near the p_{T} cut bin i.e. 150 GeV. Since the first few bins in $H_{\mathrm{T},2}/2$ (below 225 GeV) still suffer from these kinematical effects, the minimum value of $H_{\mathrm{T},2}/2$ studied is 300 GeV.

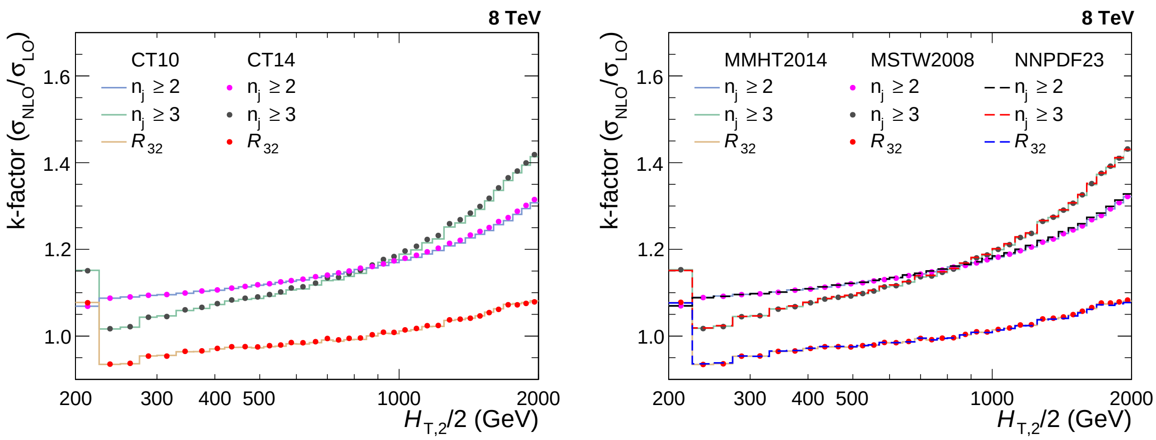

Figure 6.1: The k-factors of the NLOJET++ calculations, for inclusive 2-jet and 3-jet event cross-sections and their ratio R_{32}, using five different PDF sets.

6.1.2 Non-Perturbative Corrections

The fixed-order pQCD NLO calculations predict the parton-level cross-section but lacks accuracy due to several effects. The partons which are emitted close to each other in phase space are not handled well in lower order perturbation theories and hence requires a parton shower (PS) correction. The scattering phenomena between partons within a colliding proton, other than the hard scattering, give rise to multi-parton interactions (MPI). The partons of the hard scattering forms colorless bound states called hadrons through a process of hadronization (HAD). The MPI and hadronization cannot be modelled well within the perturbative framework. Since the fixed-order NLO calculations do not include these additional soft QCD effects, these calculations cannot be compared directly to unfolded data. So the corrections for non-perturbative effects (NP) should be taken into account in NLO calculations. The ratio of cross-section predicted with a nominal event generation interfaced to the simulation of UE contributions and to the one without hadronization and MPI effects gives the NP correction factors which are defined as :

$$C^{\mathrm{NP}} = \frac{\sigma^{\mathrm{PS+HAD+MPI}}}{\sigma^{\mathrm{PS}}} \tag{6.2}$$

In the current study, the NP effects are estimated by using samples obtained from various MC event generators with a simulation of parton shower and underlying-event (UE) contributions. The leading order (LO), HERWIG++ [55] with the default tune of version 2.3 and PYTHIA6 [21] with tune Z2*, and the NLO, POWHEG [56–58], MC event generators are considered. The matrix-element calculation is performed with POWHEG interfaced to PYTHIA8 with tune CUETS1 [59] for the UE simulation. The ratio, defined in Eq. 6.2, is obtained for each MC generator and is fitted by a power-law function defined in Eq. 6.3. Since this ratio obtained from different MC generators have large differences, so the average of the envelope, which covers all the differences, is taken as the correction factor which is then applied as bin-by-bin multiplicative factor to the parton-level NLO cross-section. The half of the envelope it is taken as the uncertainty on the NP correction factor.

$$f(H_{\mathrm{T,2}}/2) = a \cdot \left(H_{\mathrm{T,2}}/2\right)^{b} + c \tag{6.3}$$

The NP correction factors, $C^{\mathrm{NP}}_{\text{3-jet}}$ and $C^{\mathrm{NP}}_{\text{2-jet}}$ are calculated for $\mathrm{n_j} \geq 2$ and $\mathrm{n_j} \geq 3$ event cross-sections respectively and then their ratio gives the correction factor for R_{32}. The correction factors are shown in Fig. 6.2 for the inclusive 2-jet (top left) and 3-jet event cross-sections (top right), and for ratio R_{32} (bottom). At $H_{\mathrm{T,2}}/2$ ~300 GeV, the NP corrections amount to ~4-5% for inclusive 2-jet and 3-jet event cross-sections and ~1% for R_{32}, and decrease rapidly for increasing $H_{\mathrm{T,2}}/2$. On comparing the NP correction factors of R_{32} with that for individual cross-sections, it has been observed that the non-perturbative effects get reduced in R_{32}.

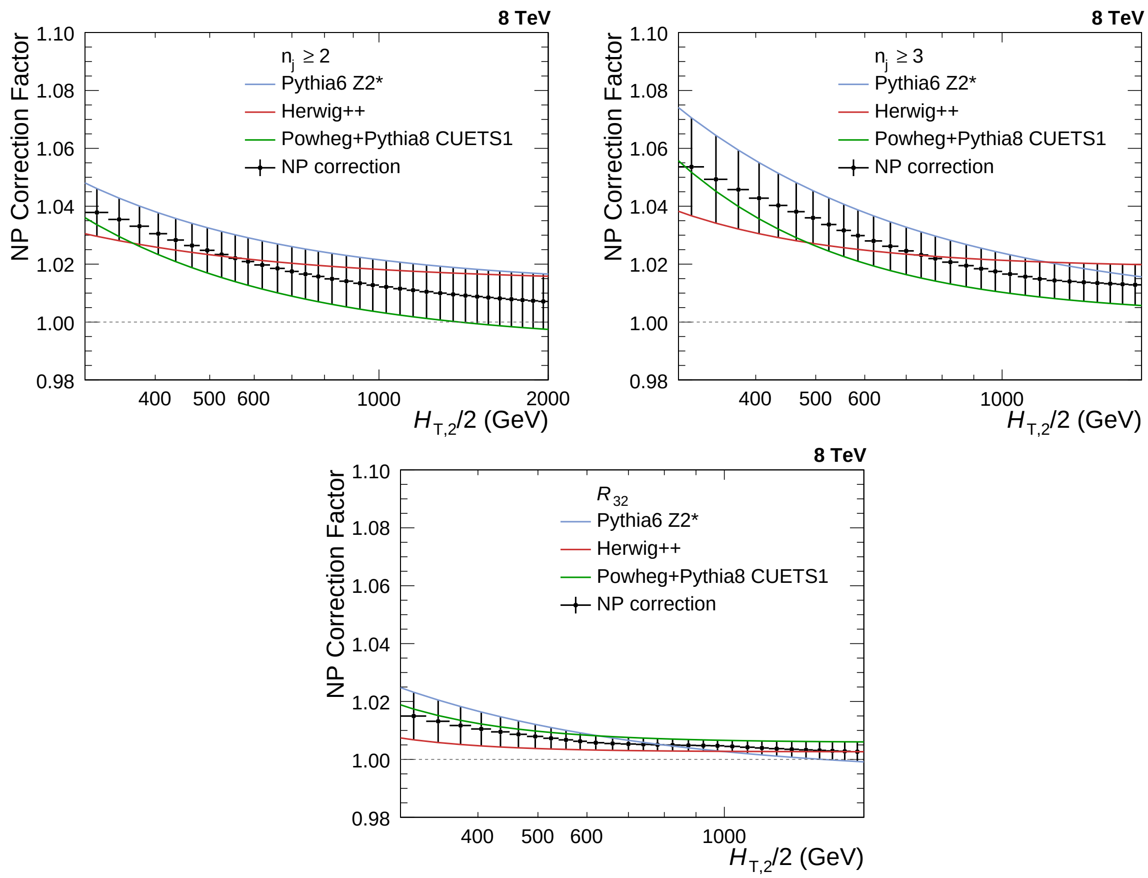

Figure 6.2: The nonperturbative (NP) corrections are presented as a function of $H_{\mathrm{T},2}/2$ for inclusive 2-jet (top left) and 3-jet (top right) event cross-sections, as well as their ratio R_{32}. These corrections are calculated from the leading order HERWIG++ with the default tune of version 2.3 (red line) and PYTHIA6 with tune Z2* (blue line); and the next-to-leading order POWHEG interfaced to PYTHIA8 with tune CUETS1 (green line) Monte Carlo event generators. The black solid circles give the average NP correction factor along with the uncertainty shown by the error bars.

6.1.3 Electroweak Corrections

In LHC, the centre-of-mass energy of proton-proton collisions is well beyond the electroweak (EW) scale ∼O(100 GeV). At such a high energy, the impact of higher order EW corrections is much more with respect to QCD effects [60] and affect jet cross-sections at large $H_{\mathrm{T},2}/2$. The quark-quark scattering processes involving virtual exchanges of massive W and Z bosons contribute to electroweak (EW) corrections. The fixed-order QCD calculations do not include EW corrections and hence the NLO theory calculations are corrected for EW effects. The EW corrections have

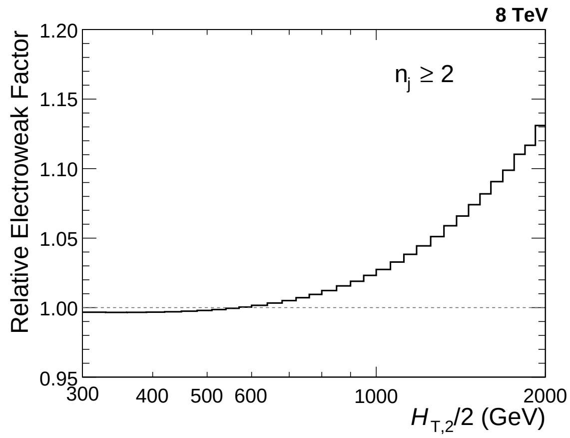

Figure 6.3: The electroweak (EW) corrections [61] in the phase space of the measurement are shown as a function of $H_{\mathrm{T},2}/2$ for inclusive 2-jet event cross-sections. These corrections are applied as a bin-by-bin correction factor to the fixed-order calculation of NLOJet++ as well as the MC predictions of MadGraph5+pythia6. The EW correction factor increases up to 13% at high ends of $H_{\mathrm{T},2}/2$ and significantly improves the agreement between data and prediction.

been calculated for inclusive 1-jet and 2-jet case, in Ref. [61]. The EW correction factors in the phase space of the measurement are shown as a function of $H_{\mathrm{T},2}/2$ in Fig. 6.3 for inclusive 2-jet event cross-sections. These correction factor increases up to 13% at high ends of $H_{\mathrm{T},2}/2$ which are applied as a bin-by-bin correction factor to the fixed-order calculation of NLOJet++. To see the effects of EW corrections, a ratio of data to theory predictions obtained using CT10-NLO PDF set and corrected with NP effects without including EW corrections (left) and including EW corrections (right) is plotted for inclusive 2-jet event cross-sections in Fig. 6.4. On comparing both the figures, it is observed that the EW corrections significantly improve the agreement between data and prediction in the high $H_{\mathrm{T},2}/2$ region. EW corrections are not available yet for inclusive 3-jet production and hence not applied for inclusive 3-jet event cross-sections. The guess from theory side is that EW for inclusive 2-jet and 3-jet will be similar, so for R_{32}, it is assumed to be equal to the factor of 1. Since the EW effects are not taken care of in MC simulations so these corrections are applied to MC predictions also.

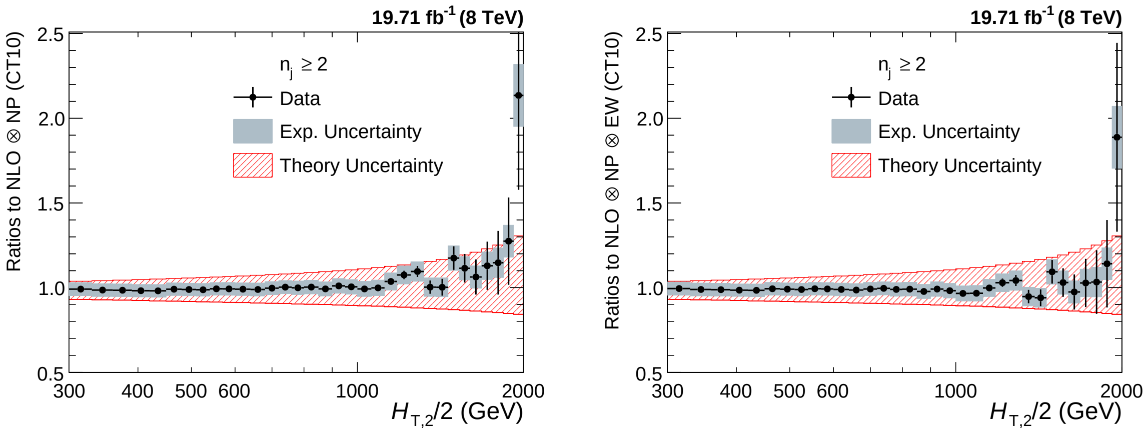

Figure 6.4: Ratio of data over theory obtained using the CT10-NLO PDF set and corrected with non-perturbative effects (NP) without including electroweak (EW) corrections (left) and including EW corrections (right) is shown for inclusive 2-jet event cross-sections. The error bars represents the statistical uncertainty of the data and the shaded rectangles represents the total experimental systematic uncertainty. The shaded band around unity indicate the total uncertainty of the theory. The EW corrections significantly improve the agreement between data and prediction in the high $H_{T,2}/2$ region.

6.2 Theoretical Uncertainties

The measurements are not only sensitive to experimental uncertainties but also to the theoretical uncertainties. The renormalization and factorization scale variations, PDF uncertainties and the non-perturbative corrections contribute to theoretical uncertainties which are described below :

6.2.1 Scale Uncertainty

In perturbative QCD calculations of cross-sections, one has to choose a renormalization (μ_r) and factorization (μ_f) scale. The dependence on scales is negligible if these calculations are performed for all orders of the perturbative series. But the perturbative series is truncated at NLO, so there is a scale dependence of the measurement which is covered by systematic uncertainty known as scale uncertainty. The scale uncertainty is evaluated with the conventional recipe of varying the default scale $H_{T,2}/2$ chosen for μ_r and μ_f independently in the following six combinations: $(\mu_r/H_{T,2}/2,\ \mu_f/H_{T,2}/2)$ = (1/2,1/2), (1/2,1), (1,1/2), (1,2), (2,1) and (2,2). The maximal upwards and downwards deviations in cross-section from the central prediction give the scale uncertainty. To calculate the scale uncertainty for cross-section ratio R_{32}, first R_{32} is obtained for each above mentioned scale choice and then its difference from central R_{32} is taken. The scale uncertainty calculated using CT10-NLO PDF set ranges from 5% to 13% and 11% to 17% for inclusive 2-jet and 3-jet events cross-sections respectively, and from 6% to 8% for R_{32}.

6.2.2 PDF Uncertainty

The calculation of jet cross-sections in proton-proton collisions relies upon the knowledge of PDFs. These PDF sets are determined by global fits to all the available deep inelastic scattering (DIS) and related hard scattering data from different experiments. The various sources affect the PDFs such as theory model, input parameters like the strong coupling constant α_S, the quark masses and the statistical and systematic uncertainty sources of the data included in the PDF fit. These sources contribute to PDF uncertainty which is evaluated according to the prescriptions given for each PDF set. The CT10-NLO PDF set [47, 62] employ the eigenvector method to evaluate the PDF uncertainties. The CT10-PDF set consists of $N_{\mathrm{ev}} = 26$ eigenvectors with two PDF members per eigenvector k, which are varied upwards and downwards to generate a set of eigenvector pairs. The asymmetric uncertainties, ΔX^+ and ΔX^-, of a quantity X are given by Eq. 6.4 where X_0 is the central prediction, X_k^+ and X_k^- are the predictions using the upwards and downwards variation of each eigenvector k.

$$
\begin{aligned}
\Delta X^+ &= \sqrt{\sum_{k=1}^{N_{\mathrm{ev}}} \left[\max(X_k^+ - X^0, X_k^- - X^0, 0)\right]^2} \\
\Delta X^- &= \sqrt{\sum_{k=1}^{N_{\mathrm{ev}}} \left[\min(X_k^+ - X^0, X_k^- - X^0, 0)\right]^2}
\end{aligned}
\tag{6.4}
$$

The symmetric uncertainty ($\Delta X^{\pm}$) is given by half the difference of the upwards and downwards variations :

$$\Delta X^{\pm} = \sqrt{\sum_{k=1}^{N_{\mathrm{ev}}} \left[\frac{X_k^{+} - X_k^{-}}{2} \right]^2} \tag{6.5}$$

The CT10-NLO PDF set uncertainties are downscaled by a factor of 1.64 in order to have the uncertainties at the 68.3% confidence level CL(1σ) instead of 90% CL(2σ) such that to have a uniform treatment with respect to other PDF sets. The PDF uncertainty as derived with the CT10-NLO PDF set is the dominant source of uncertainty and ranges from 3% to 30% for inclusive 2-jet and from 4% to 32% for 3-jet cross-sections. For R_{32}, the ratio of predictions for inclusive 3-jet to that of 2-jet is taken for each eigen vector with upwards and downwards variations separately and then PDF uncertainty is calculated as done for individual cross-sections. The PDF uncertainty ranges and from 2% to 10% for cross-section ratio R_{32}.

6.2.3 Non-perturbative Uncertainty

As discussed in 6.1.2, the differences in the non-perturbative (NP) corrections calculated from various Monte Carlo event generators introduce the NP uncertainty which is of the order of 1% and 1 to 2% for inclusive 2-jet and 3-jet event cross-sections respectively, and $< 1\%$ for cross-section ratio R_{32}.

6.2.4 Total Theoretical Uncertainty

The total systematic theoretical uncertainties are obtained as the quadratic sum of the scale, PDF and NP uncertainties. Figure 6.5 presents the systematic theoretical uncertainties affecting the cross-section measurement for inclusive 2-jet (top left) and 3-jet events (top right) and the cross-section ratio R_{32} (bottom), using CT10-

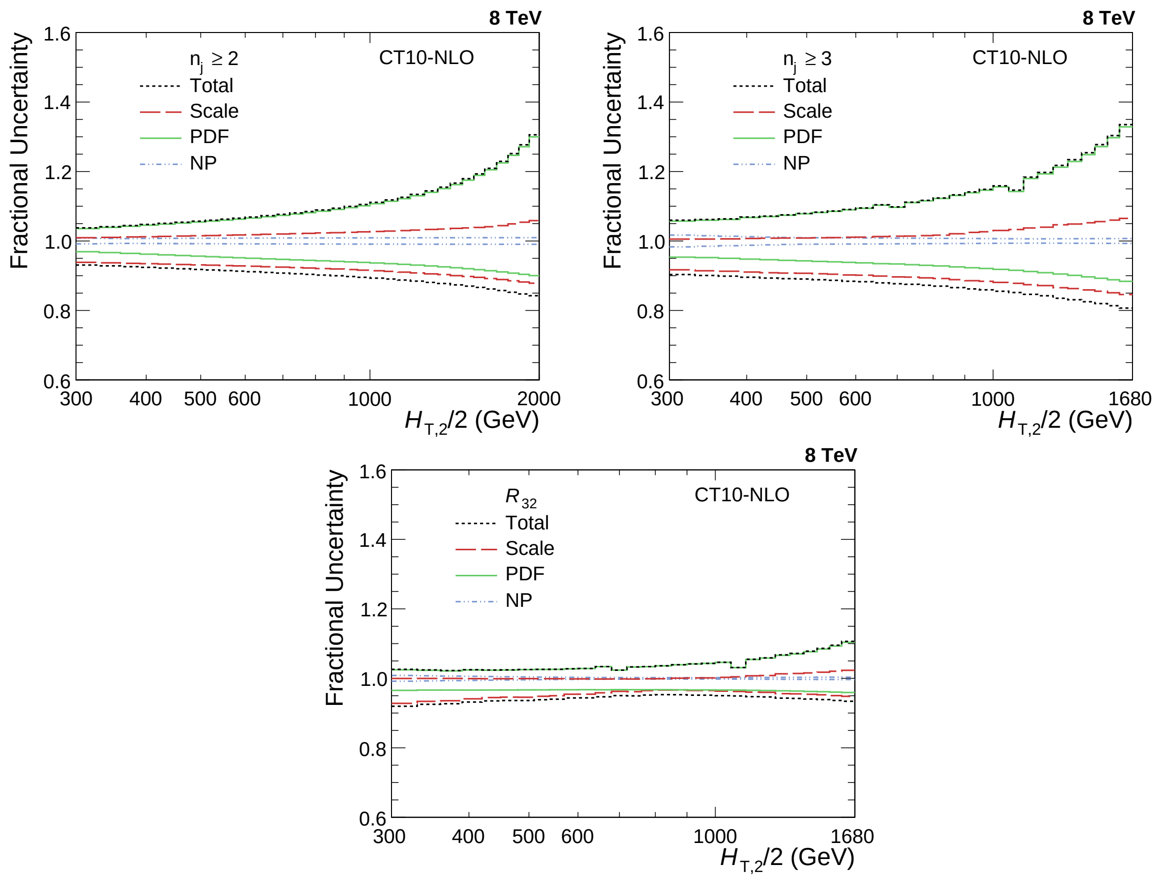

Figure 6.5: The systematic theoretical uncertainties affecting the cross-section measurement for inclusive 2-jet (top left) and 3-jet events (top right) and their ratio R_{32} (bottom). The scale (red dashed line), PDF (green line) and NP (blue dashed line) uncertainties as well as total uncertainty (black dashed line) obtained using CT10-NLO PDF set are shown. The total theoretical uncertainty is asymmetric and is dominated by PDF uncertainty.

NLO PDF set. The scale (red dashed line), PDF (green line) and NP (blue dashed line) uncertainties as well as total theoretical uncertainty (black dashed line) are shown. The total theoretical uncertainty is asymmetric and is dominated by PDF uncertainty which grows in magnitude with increasing value of $H_{\mathrm{T},2}/2$. Table 6.2 quotes the values of the theoretical uncertainty from each source as well as total uncertainty affecting the measurements. The bin-wise values of uncertainties (in %) from each source as well as total uncertainty are shown in Tables A.5, A.6 and A.7 for $\mathrm{n_j} \geq 2$ and $\mathrm{n_j} \geq 3$ event cross-sections and cross-section ratio R_{32}, respectively. The computation of the NLO predictions with NLOJET++ is also subject to statistical fluctuations from the complex numerical integrations. For the inclusive 2-jet event cross-sections this uncertainty is smaller than about a per mille, while for the inclusive 3-jet event cross-section it amounts to 1-9 per mille. Hence the statistical uncertainty is not considered in the total theoretical uncertainty. The small dips at ∼700 and 1000 GeV in the PDF uncertainty for inclusive 3-jet events cross-sections and cross-section ratio R_{32} is a feature of the CT10-NLO PDF set.

Table 6.2: Overview of all systematic theoretical uncertainties, obtained using CT10-NLO PDF set, affecting the measurement of cross-sections for inclusive 2-jet (left) and 3-jet events (middle) and cross-section ratio R_{32} (right).

Uncertainty Source	**Inclusive 2-jet**	**Inclusive 3-jet**	$\boldsymbol{R_{32}}$
Scale	5 to 13%	11 to 17%	6 to 8%
PDF	3 to 30%	4 to 32%	2 to 10%
Non-perturbative (NP)	1%	1 to 2%	$< 1\%$
Total	3 to 30%	5 to 34%	3 to 11%

6.3 Comparison of Theory to Data

After correcting the measurement for detector effects as well as NLO pQCD calculations for non-perturbative (NP) and electroweak (EW) effects, it is now feasible to compare the measured cross-sections with the theory predictions. Figure 6.6 shows the measured differential inclusive 2-jet and 3-jet event cross-sections as a function of $H_{\mathrm{T},2}/2$ after unfolding for detector effects. On the left, the measurements (points) are compared to the NLOJet++ predictions using the CT10-NLO PDF set (line), corrected for NP effects and in addition for EW effects in the 2-jet case. On the right, the comparison is made to the predictions from MadGraph5+pythia6 (MG+P6) with tune Z2* (line), corrected for EW effects in the 2-jet case. The error bars give the total experimental uncertainty, given by the quadrature sum of the statistical and systematic uncertainties. On a logarithmic scale, the data are in well agreement with the NLO predictions over the whole range of $H_{\mathrm{T},2}/2$ from 300 GeV up to 2000

(2-jet) and 1680 GeV (3-jet) respectively.

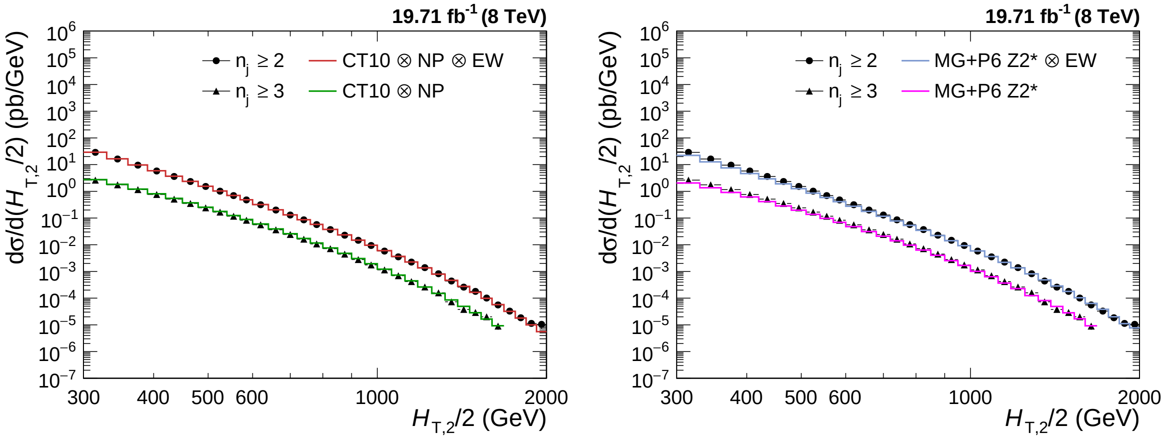

Figure 6.6: Comparison of the measured differential inclusive 2-jet and 3-jet event cross-sections as a function of $H_{\mathrm{T},2}/2$ to theoretical predictions. On the left, the data (points) are shown together with NLOJet++ predictions (line) using the CT10-NLO PDF set, corrected for non-perturbative (NP) and electroweak (EW) effects (2-jet) or only NP effects (3-jet). On the (right), the data (points) are compared to predictions from MadGraph5+pythia6 (MG+P6) with tune Z2* (line), corrected for EW effects in the 2-jet case. The error bars give the total experimental uncertainty, given by the quadrature sum of the statistical and systematic uncertainties.

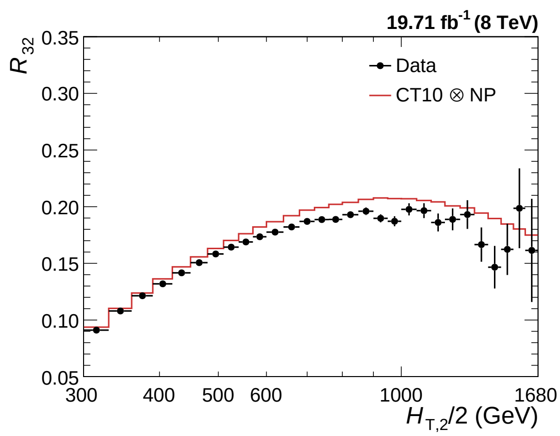

Figure 6.7: Cross-section ratio R_{32} as a function of $H_{\mathrm{T},2}/2$ calculated from data (solid circles) in comparison to that from NLO pQCD predictions obtained using the CT10-NLO PDF set corrected with non-perturbative (NP) corrections (line). The error bars correspond to the total experimental uncertainty derived as quadratic sum from all uncertainty sources.

Figure 6.7 shows the cross-section ratio R_{32} obtained from unfolded data data (solid circles) in comparison to that from NLO pQCD predictions obtained using the CT10-NLO PDF set corrected with NP corrections (line). The error bars here represents the total experimental uncertainty derived as quadratic sum from all uncertainty sources. The deviations of measured R_{32} from the theoretical predicted value can be explained by the electroweak effects which are not considered yet because of their unavailability for inclusive 3-jet event cross-sections.

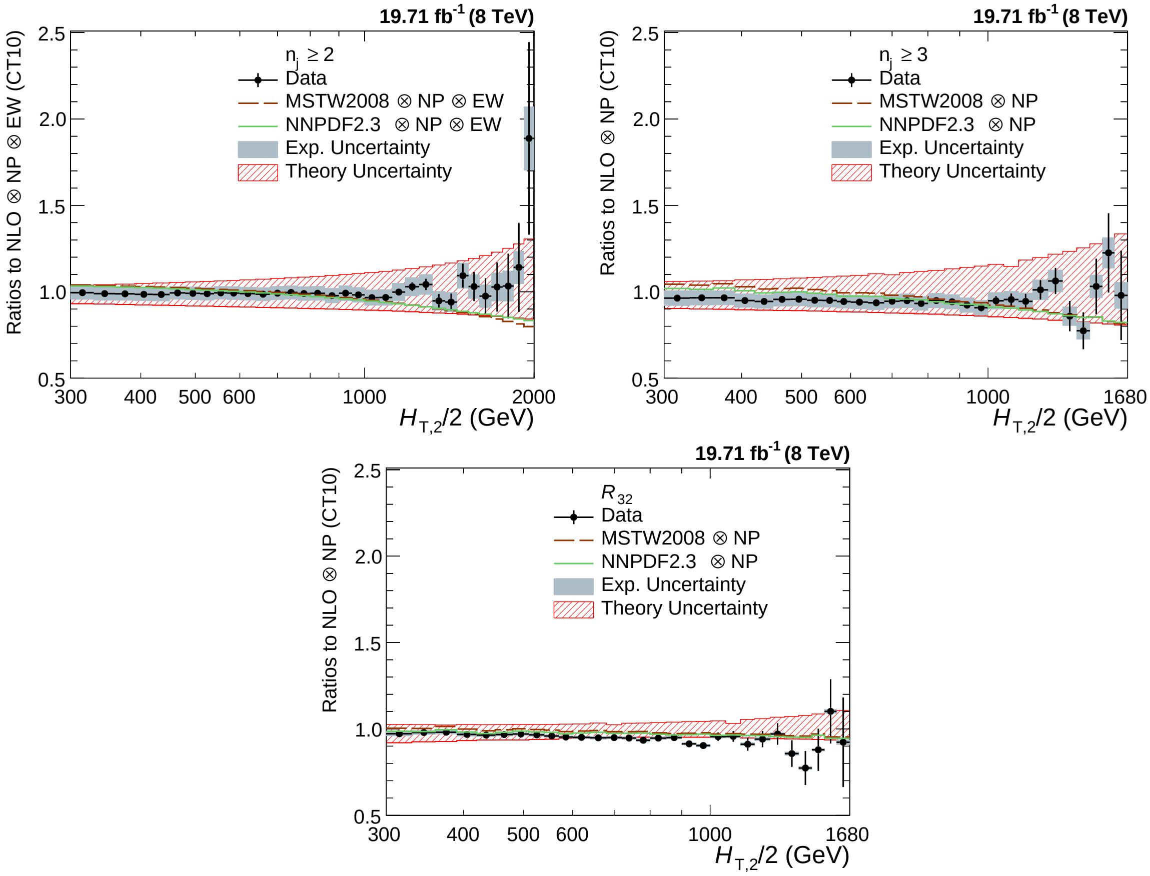

Figure 6.8: Ratio of data over theory using the CT10-NLO PDF set for inclusive 2-jet (top left) and 3-jet event cross-sections (top right) and their ratio R_{32} (bottom). The theory predictions are corrected for non-perturbative effects (NP) and also for electroweak effects (EW) for inclusive 2-jet only. For comparison predictions employing two other PDF sets, MSTW2008 and NNPDF2.3, are also shown. The error bars represents the statistical uncertainty of the data and the shaded rectangles represents the total experimental systematic uncertainty. The shaded band around unity indicate the total uncertainty of the theory.

For better visibility, the ratios of data over the theory at NLO are also studied in details. In Fig. 6.8, the ratios of data over NLOJet++ predictions using the CT10-NLO PDF set are shown for inclusive 2-jet (top left) and 3-jet event cross-sections (top right) as well as their ratio R_{32} (bottom). The data are well described by the predictions within their uncertainty, which is dominated at large $H_{T,2}/2$ by

PDF effects in the upwards and by scale variations in the downwards direction. A trend towards an increasing systematic excess of the 2-jet data with respect to theory, starting at about 1 TeV in $H_{\mathrm{T},2}/2$, is remedied by the inclusion of EWK corrections. In the 3-jet case the statistical precision of the data and the reach in $H_{\mathrm{T},2}/2$ is insufficient to observe any effect. The alternative PDF sets MSTW2008 and NNPDF2.3 exhibit a small underestimation of the cross-sections at high $H_{\mathrm{T},2}/2$.

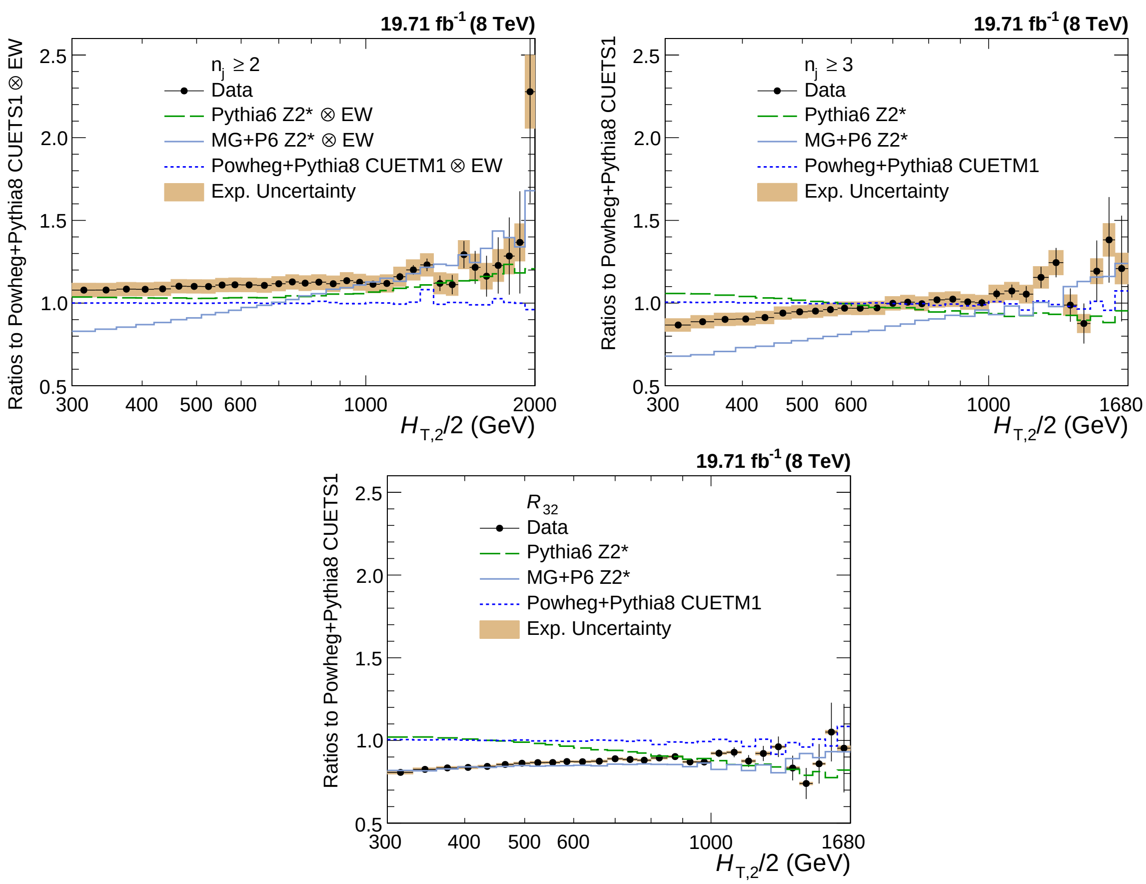

Figure 6.9: Ratio of data over the prediction from POWHEG+PYTHIA8 with tune CUETS1 are presented for inclusive 2-jet (top left) and 3-jet event cross-sections (top right) as well as their ratio R_{32} (bottom). For comparison the alternative tune CUETM1 of POWHEG+PYTHIA8, the tree-level multi-leg improved prediction by MADGRAPH5+PYTHIA6 with tune Z2*, and the the LO MC predictions from PYTHIA6 tune Z2* are shown as well. The error bars correspond to the statistical uncertainty of the data and the shaded rectangles to the total experimental systematic uncertainty. EW corrections have been accounted for in this comparison in the 2-jet case only.

The POWHEG framework providing a NLO dijet calculation matched to the parton showers of PYTHIA8 employed with the CUETS1 and CUETM1 tunes [59] is also used for a comparison. The ratios of data over theory from POWHEG+PYTHIA8 with tune CUETS1 are shown for inclusive 2-jet (top left) and 3-jet event cross-sections (top right) as well as their ratio R_{32} (bottom) in Fig. 6.9. For comparison, the LO prediction from PYTHIA6 with tune Z2*, the tree-level multi-leg improved prediction by MADGRAPH5+PYTHIA6 with tune Z2*, and the matched NLO prediction from POWHEG+PYTHIA8 with tune CUETM1 are shown as well. EW corrections have been accounted for in this comparison in the 2-jet case only. Significant discrepancies, which are cancelled to a large extent in the ratio R_{32}, are visible in the comparison with the LO prediction from MADGRAPH5+PYTHIA6 with tune Z2*, in particular for small $H_{\mathrm{T},2}/2$. In contrast, the employed dijet MC POWHEG+PYTHIA8 better describe the 2-jet event cross-section, but fail for the 3-jet case.

The jet measurements at hadron colliders can be used to extract the strong coupling constant α_S, which is discussed in the next chapter.

Chapter 7

Determination of the Strong Coupling Constant

The inclusive jet production cross-section at hadron colliders mainly depends on the strong coupling constant α_S for a given centre-of-mass energy. Hence the measurements of the inclusive jet cross-section and jet properties provide a direct probe to measure the strong coupling constant. The measurement of α_S has been already done by various experiments such as CMS [1,35,44,63,64], ATLAS [65], D0 [66,67], H1 [68,69], and ZEUS [70]. In this thesis, the measurements of differential inclusive 2-jet and 3-jet event cross-sections as well as the cross-section ratio R_{32}, as a function of $H_{\mathrm{T},2}/2$ are used to extract the value of the strong coupling constant at the scale of the Z boson mass $\alpha_s(M_Z)$. The differential inclusive jet production cross-section upto at NLO is given by [71] :

$$\frac{d\sigma}{d(H_{\mathrm{T},2}/2)} = \alpha_S^2(\mu_r)\hat{X}^{(0)}(\mu_f, H_{\mathrm{T},2}/2)\left[1 + \alpha_S(\mu_r)K1(\mu_r, \mu_f, H_{\mathrm{T},2}/2)\right] \tag{7.1}$$

where $\frac{d\sigma}{d(H_{\mathrm{T},2}/2)}$ is the differential inclusive jet production cross-section as a function of $H_{\mathrm{T},2}/2$, μ_r and μ_f are the renormalization and factorization scales set equal to $H_{\mathrm{T},2}/2$, $\alpha_S^2(\mu_r)\hat{X}^{(0)}(\mu_f, H_{\mathrm{T},2}/2)$ is the leading order (LO) contribution to the differential inclusive jet production cross-section and $\alpha_S^3(\mu_r)\hat{X}^{(0)}(\mu_f, H_{\mathrm{T},2}/2)K1(\mu_r, \mu_f, H_{\mathrm{T},2}/2)$ is the next-to-leading order (NLO) contribution. Equation 7.1 shows how the inclusive jet production cross-section varies with $\alpha_S(\mu_r)$.

7.1 Sensitivity of Measurements to $\alpha_s(M_Z)$

For a fixed choice of μ_r and μ_f, different input values of $\alpha_s(M_Z)$ to a PDF set will lead to different theory predictions of the differential cross-section distribution. This will give an estimate of the sensitivity of the theory predictions to the varying input value of $\alpha_s(M_Z)$. A comparison of the measured spectrum with the theory predictions obtained using all $\alpha_s(M_Z)$ inputs will give a hint of the input value of $\alpha_s(M_Z)$ for which the theory distribution has the closest matching with data. In this section, the sensitivity of the inclusive differential jet event cross-sections and cross-section ratio, R_{32} to varying input values of $\alpha_s(M_Z)$ for different PDF sets is demonstrated by plotting the ratios of data over theory predictions with central value of $\alpha_s(M_Z)$.

Figures 7.1, 7.2 and 7.3 present the ratio of data to the theory predictions, corrected for NP effects, for all variations in $\alpha_s(M_Z)$ available for the PDF sets CT10, CT14, MSTW2008, MMHT2014 and NNPDF2.3 at NLO evolution order as specified in Table 6.1, for inclusive 2-jet event cross-sections, inclusive 3-jet events cross-sections and ratio R_{32} respectively. The $\alpha_s(M_Z)$ value is varied in the range 0.112-0.127, 0.111-123, 0.110-0.130, 0.108-0.128 and 0.114-0.124 in steps of 0.001 for the CT10, CT14, MSTW2008, MMHT2014 and NNPDF2.3PDF sets, respectively. The error bars correspond to the total experimental uncertainty derived as quadratic sum from all uncertainty sources. The theory predictions are also corrected for EW effects for inclusive 2-jet events cross-section. A small slope increasing with $H_{\mathrm{T},2}/2$

is visible for most PDFs in both cross-sections. This effect is largely cancelled in the cross-section ratio. R_{32} exhibits a flat behaviour with respect to the predictions for all five PDF sets in the whole range of $H_{\mathrm{T},2}/2$ up to 1680 GeV. Therefore, these data can be used to determine the strong coupling constant, although only up to 1 TeV for the cross-sections as long as electroweak corrections are not taken into account.

Moreover, the different sensitivity to $\alpha_s(M_Z)$ caused by the leading power in α_S in the expansion of the 2-jet inclusive ($\propto \alpha_S^2$) and the 3-jet inclusive cross-section ($\propto \alpha_S^3$), and their ratio ($\propto \alpha_S^1$) is clearly visible from the spread between the calculations for the smallest and largest value of $\alpha_s(M_Z)$ within the same PDF set when passing through Figures 7.1–7.3. This also demonstrates the potential of ratios R_{mn} with m-$n > 1$.

7.2 Determination of $\alpha_s(M_Z)$

As discussed in the previous section, the measured inclusive 2-jet and 3-jet event cross-sections and their ratio R_{32} can be used for a determination of the strong coupling constant $\alpha_s(M_Z)$. To extract the value of $\alpha_s(M_Z)$, a general fit procedure [1, 64] has been followed and is described in the following section.

7.2.1 Fitting Procedure

The value of $\alpha_s(M_Z)$ is determined by minimizing the chi-square (χ^2) between the experimental measurement and the theoretical predictions. The χ^2 is defined as:

$$\chi^2 = M^T C^{-1} M \tag{7.2}$$

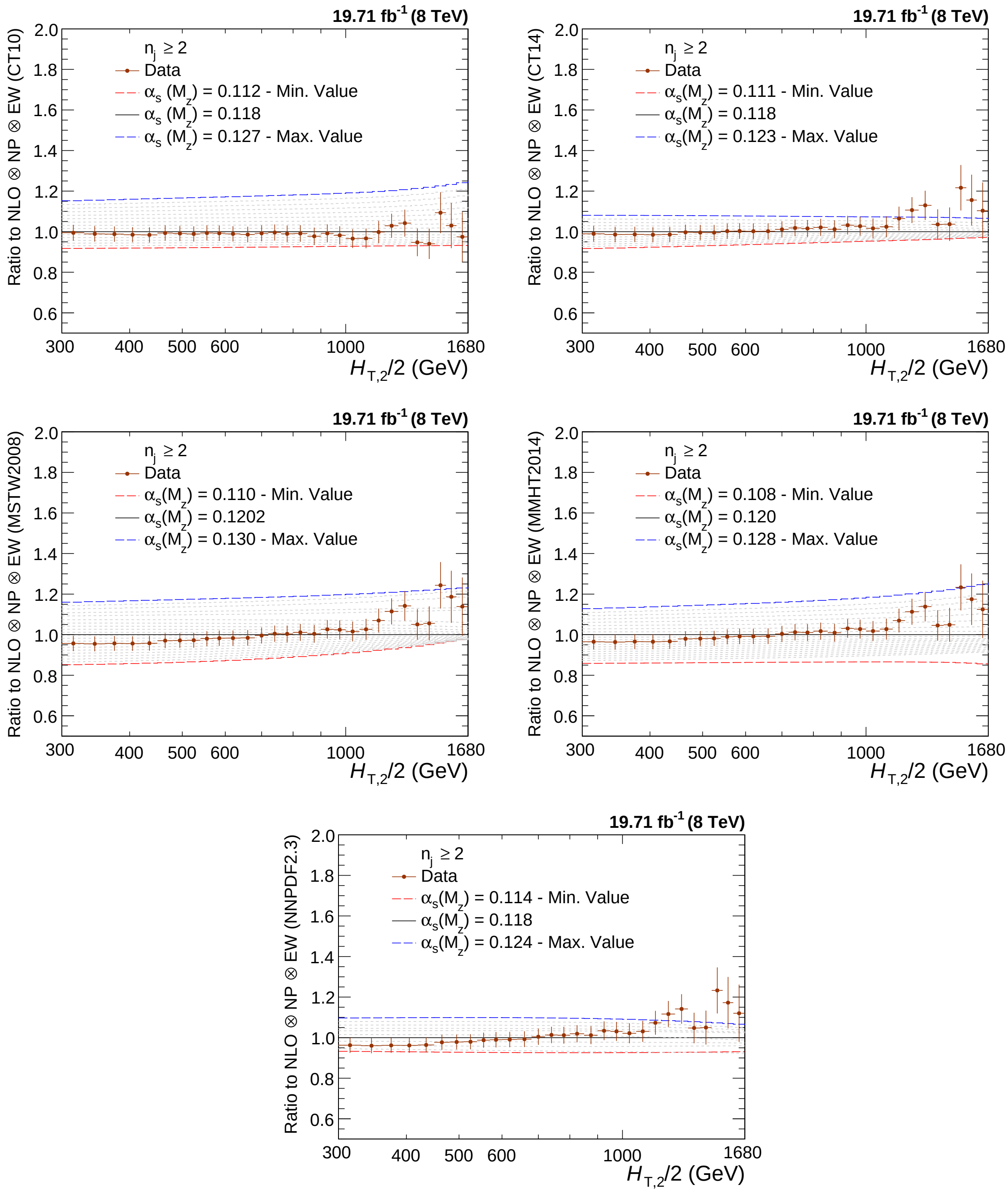

Figure 7.1: Ratio of the inclusive 2-jet differential cross-section to theory predictions using the CT10 (top left), the CT14 (top right), the MSTW2008 (middle left), the MMHT2014 (middle right) and NNPDF2.3 (bottom) NLO PDF sets for a series of values of $\alpha_s(M_Z)$. The $\alpha_s(M_Z)$ value is varied in the range 0.112-0.127, 0.111-123, 0.110-0.130, 0.108-0.128 and 0.114-0.124 in steps of 0.001 for the CT10, CT14, MSTW2008, MMHT2014 and NNPDF2.3 NLO PDF sets, respectively. The error bars correspond to the total experimental uncertainty. The theory predictions are corrected for non-perturbative (NP) and electroweak (EW) effects.

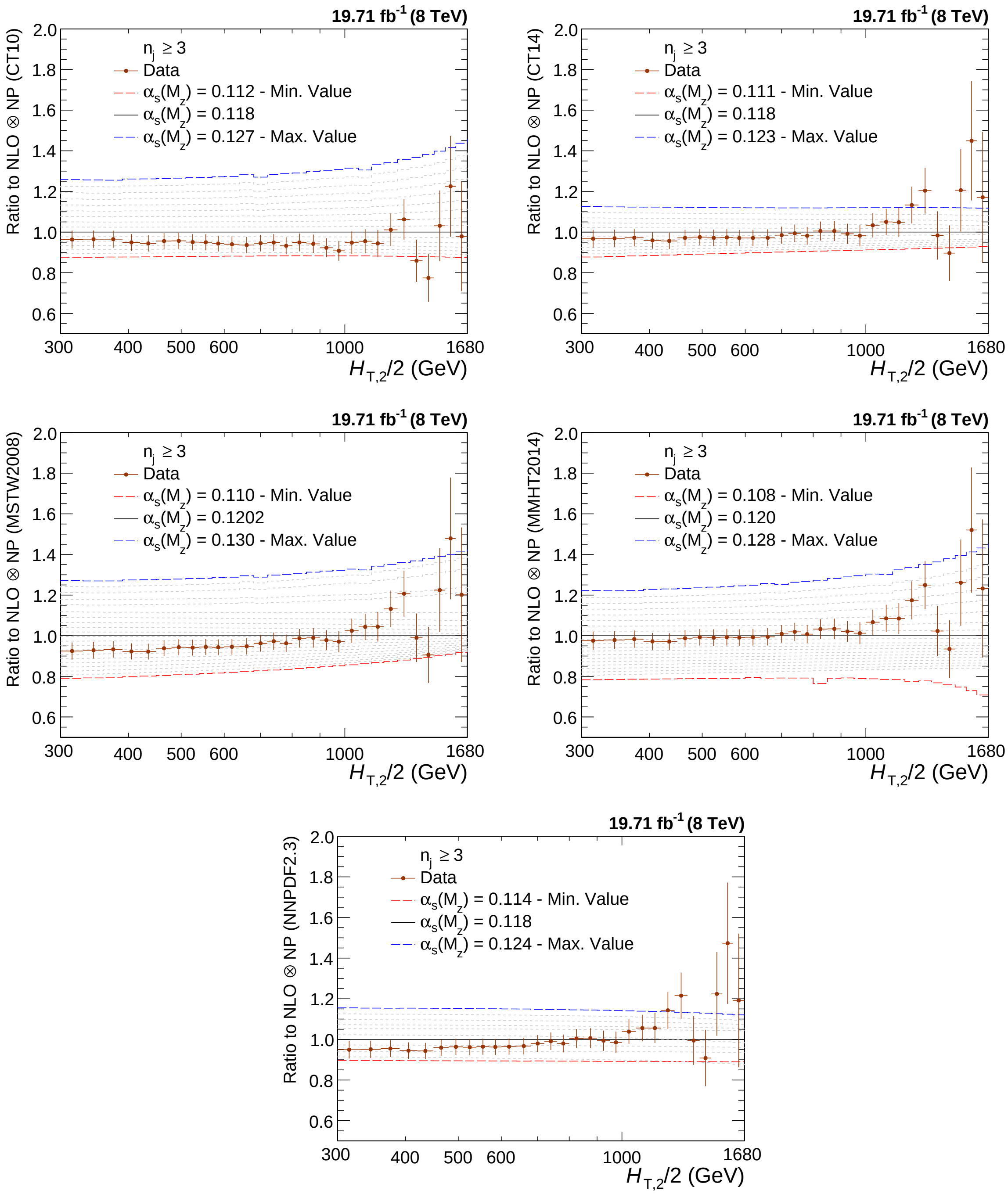

Figure 7.2: Ratio of the inclusive 3-jet differential cross-section to theory predictions using the CT10 (top left), the CT14 (top right), the MSTW2008 (middle left), the MMHT2014 (middle right) and NNPDF2.3 (bottom) NLO PDF sets for a series of values of $\alpha_s(M_Z)$. The $\alpha_s(M_Z)$ value is varied in the range 0.112-0.127, 0.111-123, 0.110-0.130, 0.108-0.128 and 0.114-0.124 in steps of 0.001 for the CT10, CT14, MSTW2008, MMHT2014 and NNPDF2.3 NLO PDF sets, respectively. The error bars correspond to the total experimental uncertainty. The theory predictions are corrected for non-perturbative (NP) effects.

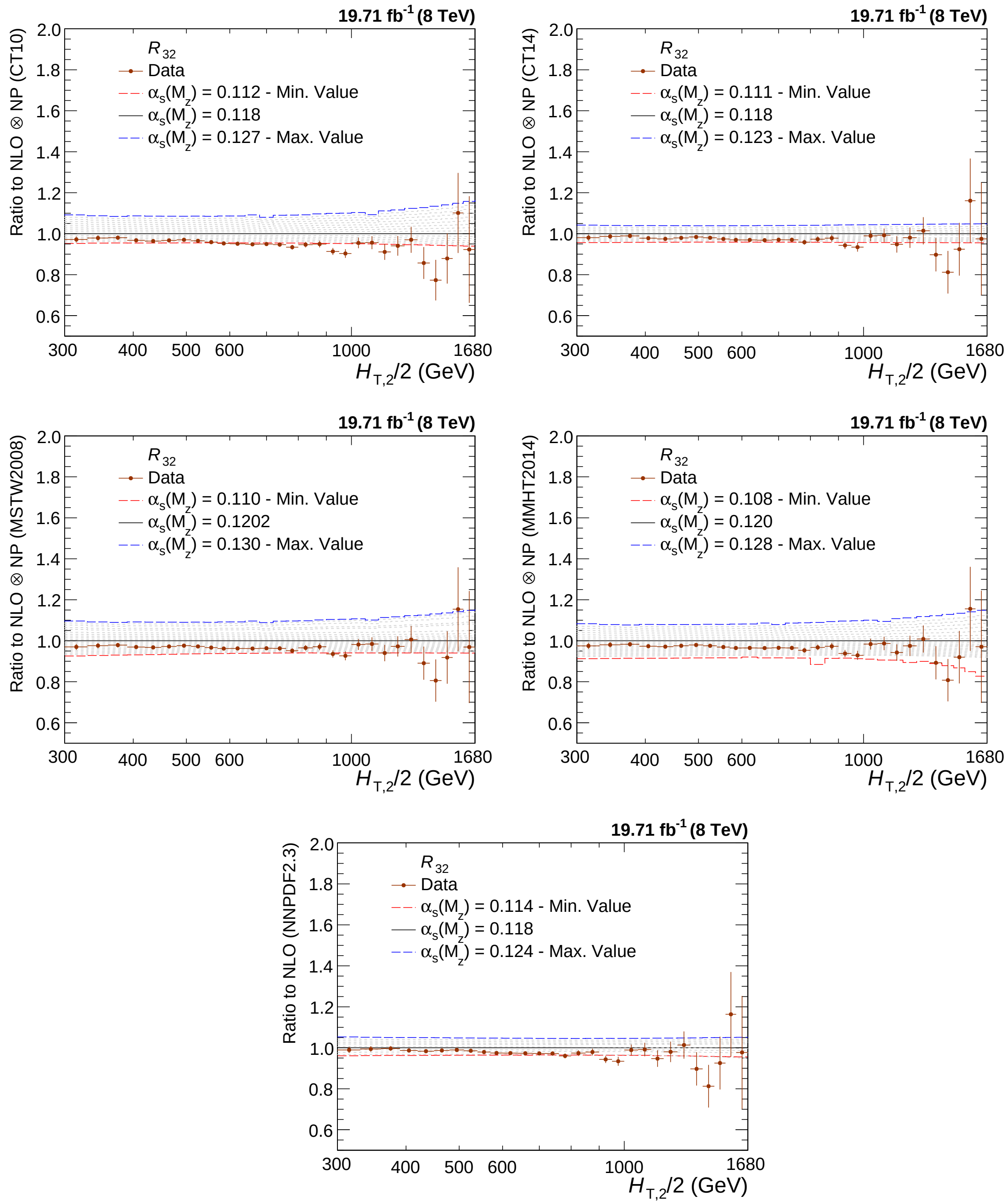

Figure 7.3: Ratio of the cross-section ratio, R_{32} to theory predictions using the CT10 (top left), the CT14 (top right), the MSTW2008 (middle left), the MMHT2014 (middle right) and NNPDF2.3 (bottom) NLO PDF sets for a series of values of $\alpha_s(M_Z)$. The $\alpha_s(M_Z)$ value is varied in the range 0.112-0.127, 0.111-123, 0.110-0.130, 0.108-0.128 and 0.114-0.124 in steps of 0.001 for the CT10, CT14, MSTW2008, MMHT2014 and NNPDF2.3 NLO PDF sets, respectively. The error bars correspond to the total experimental uncertainty. The theory predictions are corrected for non-perturbative (NP) effects.

where M is the vector of the differences between the data (D^i) and the theoretical values (T^i) in each bin i,

$$M^i = D^i - T^i \tag{7.3}$$

and C is the covariance matrix including all experimental uncertainties as described in Sec. 5.6 and some theoretical uncertainties discussed in Sec. 6.2. The covariance matrix $C = C_{\text{exp}} + C_{\text{theo}}$ is defined as the sum of covariances of experimental and theoretical sources of uncertainty as follows :

$$C_{\text{exp}} = \text{Cov}^{\text{ExpStat}} + \sum \text{Cov}^{\text{JEC}} + \text{Cov}^{\text{Unfolding}} + \text{Cov}^{\text{Lumi}} + \text{Cov}^{\text{Residual}} \tag{7.4}$$

$$C_{\text{theo}} = \text{Cov}^{\text{TheoStat}} + \text{Cov}^{\text{NP}} + \text{Cov}^{\text{PDF}} \tag{7.5}$$

where the labelled covariance matrices account for the following effects:

- $\text{Cov}^{\text{ExpStat}}$: statistical uncertainty of the data including correlations introduced by the unfolding
- Cov^{JEC}: the jet energy corrections (JEC) systematic uncertainty
- $\text{Cov}^{\text{Unfolding}}$: the unfolding systematic uncertainty including the resolution (JER) and model dependence
- Cov^{Lumi}: the luminosity uncertainty
- $\text{Cov}^{\text{Residual}}$: a residual uncorrelated systematic uncertainty summarizing individual causes such as small trigger and identification inefficiencies, time dependence of the jet p_{T} resolution, and uncertainty on the trigger prescale factors
- $\text{Cov}^{\text{TheoStat}}$: statistical uncertainty caused by numerical integrations in the cross-section computations

- $\mathrm{Cov}^{\mathrm{NP}}$: the systematic uncertainty of the non-perturbative (NP) corrections
- $\mathrm{Cov}^{\mathrm{PDF}}$: the PDF uncertainties

While taking the differences between theory and data, the treatment of experimental and theoretical systematic uncertainties is crucial. The Unfolding, JEC, Lumi and PDF and NP systematic uncertainties are treated as 100% correlated among $H_{\mathrm{T},2}/2$ bins. If δ_i is the total uncertainty on the differential cross-section, for the i-th $H_{\mathrm{T},2}/2$ bin, for any of these fully correlated sources, then thei, j-th element of the corresponding covariance matrix is given by $\mathrm{COV}_{ij} = \delta_i \times \delta_j$. The JEC, unfolding, and luminosity uncertainties are treated as multiplicative to avoid the statistical bias that arises when estimating uncertainties from data. In fits of the ratio R_{32}, the luminosity and residual uncorrelated uncertainties cancel completely. Partial cancellations between the other sources of uncertainty are taken into account in the fit.

The evaluation of PDF uncertainty depends on the individual PDF set as already discussed in Sec. 6.2.2. The PDF covariance matrix construction varies among different PDF sets. The CT10, CT14, MMHT2014 and MSTW2008 NLO PDF sets employ the eigenvector method to evaluate the PDF uncertainties as explained in Sec. 6.2.2. The number of eigenvectors (N_{ev}) with two PDF members per eigenvector for CT10, CT14, MMHT2014 and MSTW2008 NLO PDF sets are 26, 28, 25 and 20, respectively. The NNPDF2.3 PDF set comes with hundred different replicas (N_{rep}) instead of different eigenvectors, as for CT10 or CT14 PDF sets. The mean uncertainty is calculated as average uncertainty from 100 different replicas. Following the prescription given in [72], the PDF uncertainty is calculated as :

$$(\Delta X)^2 = \frac{1}{N_{rep} - 1} \sum_{k=1}^{N_{rep}} [X_k - \langle X_k \rangle]^2 \tag{7.6}$$

where ΔX is the uncertainty on predicted differential cross-section, X_k is the differential cross-section for k-th replica and $\langle X_k \rangle$ is the average differential cross-section from all the replicas.

Scale uncertainties of the pQCD predictions are taken into account by employing the offset method, i.e. by performing separate fits with varying scale factors as described in the Sec. 6.2.1. The largest upwards and downwards deviations from the default factors are defined as the uncertainty. At NLO such scale variations predominantly lead to smaller cross-sections and also a smaller ratio R_{32} as visible in Fig. 6.5. As a consequence the scale uncertainty in fits is equally asymmetric, where smaller cross-sections or ratios are compensated by an increase in the fitted value for $\alpha_s(M_Z)$.

7.2.2 Fit Results

To determine the value of the strong coupling constant at the scale of the Z boson mass $\alpha_s(M_Z)$, fits to the differential inclusive 2-jet and 3-jet events cross-sections are performed using five different NLO PDF sets : CT10, CT14, MSTW2008, MMHT2014 and NNPDF2.3. The range in $H_{\mathrm{T},2}/2$ is restricted to be between 300 GeV and 1 TeV to avoid the region close to the minimal p_{T} threshold of 150 GeV for each jet at low p_{T} and the onset of electroweak effects at high $H_{\mathrm{T},2}/2$, which are available for the dijet case only. The $\alpha_s(M_Z)$ results obtained from a simultaneous fit to all 19 $H_{\mathrm{T},2}/2$ bins in the above mentioned range are reported in Table 7.1. For comparison, a simultaneous fit to both cross-sections ignoring any correlations, and a fit to the cross-section ratio R_{32}, fully accounting for correlations is also performed and the results are tabulated in Table 7.2. The electroweak effects are assumed to cancel in the ratio as do the luminosity and the uncorrelated uncertainty.

All cross-section fits give compatible values for $\alpha_s(M_Z)$ in the range of 0.115-0.118 whereas for the ratio R_{32} somewhat smaller values are obtained. But for individual cross-sections, χ^2/n_{dof} values are small as compared to the cross-section ratio R_{32}. A possible explanation is an overestimation of the residual uncorrelated uncertainty of 1% that is cancelled for R_{32}. If the fits are repeated with an assumed uncertainty of 0.25% instead, the χ^2/n_{dof} values lie around unity while the $\alpha_s(M_Z)$ values are still compatible with the previous results but with slightly reduced uncertainties.

Table 7.1: Determination of $\alpha_s(M_Z)$ from the inclusive 2-jet and 3-jet event cross-sections using five PDF sets at NLO. Only total uncertainties without scale variations are quoted. The results are obtained from a simultaneous fit to all 19 $H_{\mathrm{T},2}/2$ bins in the restricted range of $0.3 < H_{\mathrm{T},2}/2 < 1.0$ TeV.

PDF set	Inclusive 2-jets			Inclusive 3-jets		
	$\alpha_s(M_Z)$	$\pm\Delta\alpha_s(M_Z)$	χ^2/n_{dof}	$\alpha_s(M_Z)$	$\pm\Delta\alpha_s(M_Z)$	χ^2/n_{dof}
CT10	0.1174	0.0032	3.0/18	0.1169	0.0027	5.4/18
CT14	0.1160	0.0035	3.5/18	0.1159	0.0031	6.1/18
MSTW2008	0.1159	0.0025	5.3/18	0.1161	0.0021	6.7/18
MMHT2014	0.1165	0.0034	5.9/18	0.1166	0.0025	7.1/18
NNPDF2.3	0.1183	0.0025	9.7/18	0.1179	0.0021	9.1/18

Table 7.2: Determination of $\alpha_s(M_Z)$ from the inclusive 2-jet and 3-jet event cross-sections simultaneously and from their ratio R_{32} using five PDF sets at NLO. Only total uncertainties without scale variations are quoted. The results are obtained from a simultaneous fit to all 38 (left) and 19 (right) $H_{\mathrm{T},2}/2$ bins in the restricted range of $0.3 < H_{\mathrm{T},2}/2 < 1.0$ TeV. For comparison, correlations between the two cross-sections are neglected in the simultaneous fit on the left, but fully taken into account in the ratio fit on the right.

PDF set	Inclusive 2- and 3-jets			R_{32}		
	$\alpha_s(M_Z)$	$\pm\Delta\alpha_s(M_Z)$	χ^2/n_{dof}	$\alpha_s(M_Z)$	$\pm\Delta\alpha_s(M_Z)$	χ^2/n_{dof}
CT10	0.1170	0.0026	8.2/37	0.1141	0.0028	19./18
CT14	0.1161	0.0029	9.1/37	0.1139	0.0032	15./18
MSTW2008	0.1161	0.0021	11./37	0.1150	0.0023	21./18
MMHT2014	0.1168	0.0025	11./37	0.1142	0.0022	19./18
NNPDF2.3	0.1188	0.0019	15./37	0.1184	0.0021	12./18

To investigate how the electroweak (EW) corrections affect the fit results for $\alpha_s(M_Z)$, the range in $H_{\mathrm{T},2}/2$ is extended to $0.3 < H_{\mathrm{T},2}/2 < 1.68$ TeV. $\alpha_s(M_Z)$ values are obtained from fits to the inclusive 2-jet event cross-section in this range with or without EW correction factors and the results are presented in Table 7.3. The largest impact is a reduction in χ^2/n_{dof}, which indicates a better agreement when

EW effects are included. In addition, a tendency to slightly smaller $\alpha_s(M_Z)$ values is observed without the EW corrections. For the ratio R_{32}, it is expected that these effects are much reduced.

Table 7.3: Determination of $\alpha_s(M_Z)$ from the inclusive 2-jet event cross-section using five PDF sets at NLO without (left) and with (right) electroweak (EW) corrections. Only total uncertainties without scale variations are quoted. The results are obtained from a simultaneous fit to all 29 $H_{\mathrm{T},2}/2$ bins in the range of $0.3 < H_{\mathrm{T},2}/2 < 1.68$ TeV.

PDF set	without EW			with EW		
	$\alpha_s(M_Z)$	$\pm\Delta\alpha_s(M_Z)$	χ^2/n_{dof}	$\alpha_s(M_Z)$	$\pm\Delta\alpha_s(M_Z)$	χ^2/n_{dof}
CT10	0.1163	0.0034	15./28	0.1165	0.0032	14./28
CT14	0.1137	0.0033	24./28	0.1144	0.0033	17./28
MSTW2008	0.1093	0.0028	27./28	0.1133	0.0023	19./28
MMHT2014	0.1127	0.0032	32./28	0.1141	0.0032	21./28
NNPDF2.3	0.1162	0.0024	31./28	0.1168	0.0024	23./28

From Fig. 7.3 follows that only the PDF sets MSTW2008 and MMHT2014 provide a large enough range in $\alpha_s(M_Z)$ values to ensure fits without extrapolation. The other three PDF sets are at the limit such that reliable fits cannot be performed for all scale settings and/or bins in scale $Q = H_{\mathrm{T},2}/2$. Since many systematic uncertainties cancel completely or partially in the cross-section ratio R_{32} as compared to the individual cross-sections, R_{32} is used mainly to determine the value of $\alpha_s(M_Z)$. Table 7.4 give the complete results for MSTW2008 and MMHT2014 for the full range in $H_{\mathrm{T},2}/2$ of 300 GeV up to 1.68 TeV along with the corresponding components of PDF, scale, NP and total experimental except scale uncertainties are shown. In contrast to fits at NLO using cross-sections where the scale uncertainty recipe usually leads to a very asymmetric behaviour with larger downward uncertainties in the case, this is inverted for the fits to the cross-section ratio R_{32}. The scale uncertainty is the most dominant source of total uncertainty on $\alpha_s(M_Z)$. These values are determined with the central renormalization and factorization scales i.e. $\mu_r = \mu_f = H_{\mathrm{T},2}/2$. The values are also determined for the six scale factor combinations for the two PDF sets MSTW2008 and MMHT2014 ans results are shown in Table 7.5.

The uncertainty decomposition for $\alpha_s(M_Z)$ determined from cross-section ratio R_{32} is performed in four sub-ranges of $H_{\mathrm{T},2}/2$ and the results are shown in Table 7.6. The statistical uncertainty of the NLO computation is negligible in comparison to any of the other sources of uncertainty. Electroweak corrections, significant only at high $H_{\mathrm{T},2}/2$, are assumed to cancel between the numerator and denominator.

Using the MSTW2008 PDF set, which dates from before the LHC start, the strong coupling constant finally is determined to

$$\begin{aligned}\alpha_s(M_Z) &= 0.1150 \pm 0.0010\,(\mathrm{exp}) \pm 0.0013\,(\mathrm{PDF}) \pm 0.0015\,(\mathrm{NP})\,^{+0.0050}_{-0.0000}\,(\mathrm{scale}) \\ &= 0.1150 \pm 0.0023\,(\text{all except scale})\,^{+0.0050}_{-0.0000}\,(\mathrm{scale})\end{aligned} \tag{7.7}$$

The MMHT2014 PDF set, although using LHC jet data to determine the PDF parameters, leads to a very similar result of

$$\begin{aligned}\alpha_s(M_Z) &= 0.1142 \pm 0.0010\,(\mathrm{exp}) \pm 0.0013\,(\mathrm{PDF}) \pm 0.0014\,(\mathrm{NP})\,^{+0.0049}_{-0.0006}\,(\mathrm{scale}) \\ &= 0.1142 \pm 0.0022\,(\text{all except scale})\,^{+0.0049}_{-0.0006}\,(\mathrm{scale})\end{aligned} \tag{7.8}$$

7.3 Running of the Strong Coupling Constant

The value of the strong coupling constant α_S depends on the energy scale Q and it decreases with the increase of scale Q. To study this dependence, the determination of α_S is carried out at different energies. The procedure to extract $\alpha_S(Q)$ is same as the one followed for the $\alpha_s(M_Z)$. To have different energy scales, the fitted $H_{\mathrm{T},2}/2$ range 300 - 1680 GeV is divided into four different sub-ranges as shown by the first column in Table 7.7. Each of the $H_{\mathrm{T},2}/2$ range is associated with a scale Q, which

Table 7.4: Determination of $\alpha_s(M_Z)$ from the ratio R_{32} using the two most compatible PDF sets MSTW2008 and MMHT2014 at NLO along with the corresponding components of PDF, scale, NP and total (except scale) experimental uncertainties. The results are obtained from a simultaneous fit to all 29 $H_{\mathrm{T},2}/2$ bins in the full range of $0.3 < H_{\mathrm{T},2}/2 < 1.68$ TeV.

PDF set	$\alpha_s(M_Z)$	exp	PDF	NP	all exc. scale	scale	χ^2/n_{dof}
MSTW2008	0.1150	±0.0010	±0.0013	±0.0015	±0.0023	${}^{+0.0050}_{-0.0000}$	26./28
MMHT2014	0.1142	±0.0010	±0.0013	±0.0014	±0.0022	${}^{+0.0049}_{-0.0006}$	24./28

Table 7.5: Determination of $\alpha_s(M_Z)$ from the ratio R_{32} in the $H_{\mathrm{T},2}/2$ range from 0.3 up to 1.68 TeV at the central scale and for the six scale factor combinations for the two PDF sets MSTW2008 and MMHT2014.

$\mu_r/H_{\mathrm{T},2}/2$	$\mu_f/H_{\mathrm{T},2}/2$	MSTW2008		MMHT2014	
		$\alpha_s(M_Z)$	χ^2/n_{dof}	$\alpha_s(M_Z)$	χ^2/n_{dof}
1	1	0.1150	26./28	0.1142	24./28
1/2	1/2	0.1165	77./28	0.1160	73./28
2	2	0.1200	18./28	0.1191	18./28
1/2	1	0.1150	53./28	0.1136	48./28
1	1/2	0.1150	30./28	0.1142	28./28
1	2	0.1155	23./28	0.1147	22./28
2	1	0.1180	19./28	0.1175	19./28

Table 7.6: Uncertainty decomposition for $\alpha_s(M_Z)$ from the determination of α_S from the jet event rate R_{32} in bins of $H_{\mathrm{T},2}/2$. The statistical uncertainty of the NLO computation is negligible in comparison to any of the other sources of uncertainty. Electroweak corrections, significant only at high $H_{\mathrm{T},2}/2$, are assumed to cancel between the numerator and denominator.

$H_{\mathrm{T},2}/2$	MSTW2008					MMHT2014				
(GeV)	$\alpha_s(M_Z)$	exp	PDF	NP	scale	$\alpha_s(M_Z)$	exp	PDF	NP	scale
300-420	0.1157	±0.0015	±0.0014	±0.0019	${}^{+0.0053}_{-0.0000}$	0.1158	±0.0014	±0.0010	±0.0019	${}^{+0.0052}_{-0.0000}$
420-600	0.1153	±0.0011	±0.0014	±0.0018	${}^{+0.0057}_{-0.0000}$	0.1154	±0.0011	±0.0012	±0.0017	${}^{+0.0056}_{-0.0000}$
600-1000	0.1134	±0.0013	±0.0016	±0.0019	${}^{+0.0052}_{-0.0000}$	0.1140	±0.0012	±0.0012	±0.0018	${}^{+0.0045}_{-0.0000}$
1000-1680	0.1147	±0.0029	±0.0017	±0.0018	${}^{+0.0063}_{-0.0011}$	0.1154	±0.0025	±0.0014	±0.0015	${}^{+0.0056}_{-0.0011}$
300-1680	0.1150	±0.0010	±0.0013	±0.0015	${}^{+0.0050}_{-0.0000}$	0.1142	±0.0010	±0.0013	±0.0014	${}^{+0.0049}_{-0.0006}$

is the differential cross-section weighted average $H_{\mathrm{T},2}/2$ scale from the inclusive 2-jet calculations and integrated over all the measured $H_{\mathrm{T},2}/2$ bins contributing to that given $H_{\mathrm{T},2}/2$ range. Let N^j_{bin} be the total number of measured $H_{\mathrm{T},2}/2$ bins contributing to the j-th $H_{\mathrm{T},2}/2$ range, then the corresponding scale Q_j, shown in second column of Table 7.7, is calculated as :

$$Q_j = \frac{\sum\limits_{i=1}^{N^j_{bin}} H^i_{\mathrm{T},2}\left[\frac{\mathrm{d}\sigma}{\mathrm{d}(H_{\mathrm{T},2}/2)}\right]^i}{\sum\limits_{i=1}^{N^j_{bin}}\left[\frac{\mathrm{d}\sigma}{\mathrm{d}(H_{\mathrm{T},2}/2)}\right]^i} \tag{7.9}$$

The value of $\alpha_s(M_Z)$ is extracted in each $H_{\mathrm{T},2}/2$ range. These extracted $\alpha_s(M_Z)$ values are evolved to the corresponding values $\alpha_S(Q)$ and are quoted in Table 7.7 along with the extracted $\alpha_s(M_Z)$ values and the total uncertainty. The evolution is performed for five flavours at 2-loop order with the RunDec program [73, 74]. The obtained $\alpha_S(Q)$ points (black solid circles) are shown as a function of scale Q in Fig. 7.4. The black solid line and the yellow uncertainty band are evolved using $\alpha_s(M_Z) = 0.1150 \pm 0.0023$ (all except scale) $^{+0.0050}_{-0.0000}$ (scale) obtained using MSTW2008 NLO PDF set. The world average [75] (dashed line) and results from other measurements of the CMS [1,35,44,63,64], ATLAS [65], D0 [66,67], H1 [68,69], and ZEUS [70] experiments are also imposed. The current measurement is in very good agreement within the uncertainty with other results obtained by previous experiments as well as with the world average value of $\alpha_s(M_Z) = 0.1181 \pm 0.0011$ derived in Ref. [75].

Table 7.7: Evolution of the strong coupling constant between the scale of the Z boson mass and the cross-section averaged $H_{\mathrm{T},2}/2$ scale $\langle Q \rangle$ for the separate determinations in each respective fit range. The evolution is performed for five flavours at 2-loop order with the RunDec program [73, 74].

$H_{\mathrm{T},2}/2$ (GeV)	$\langle Q \rangle$ (GeV)	$\alpha_s(M_Z)$	$\alpha_S(Q)$	No. of data points	χ^2/n_{dof}
300-420	340	$0.1157^{+0.0060}_{-0.0030}$	$0.0969^{+0.0041}_{-0.0021}$	4	2.8/3
420-600	476	$0.1153^{+0.0062}_{-0.0025}$	$0.0928^{+0.0039}_{-0.0016}$	6	6.1/5
600-1000	685	$0.1134^{+0.0059}_{-0.0028}$	$0.0879^{+0.0035}_{-0.0017}$	9	7.1/8
1000-1680	1114	$0.1147^{+0.0074}_{-0.0040}$	$0.0841^{+0.0039}_{-0.0021}$	10	5.4/9

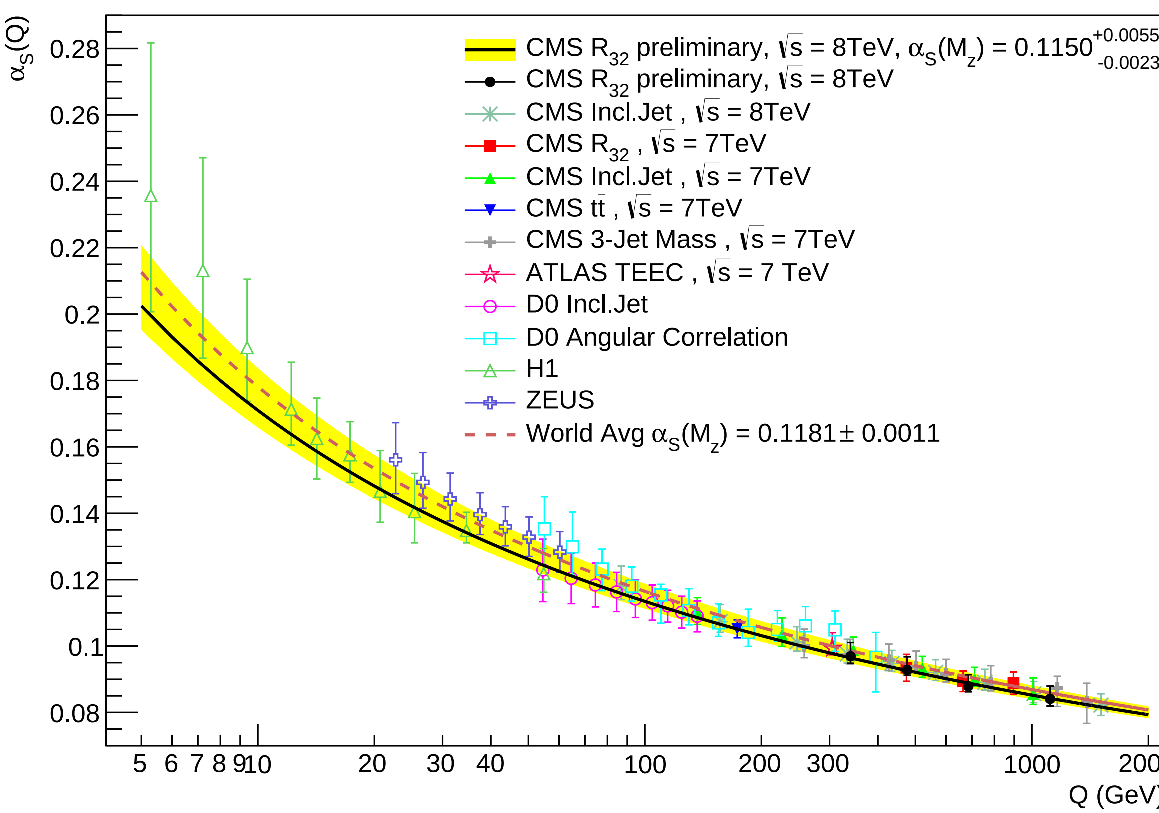

Figure 7.4: The running $\alpha_S(Q)$ as a function of the scale Q is shown as obtained by using the MSTW2008 NLO PDF set. The solid line and the uncertainty band are drawn by evolving the extracted $\alpha_s(M_Z)$ values using the 2-loop 5-flavour renormalization group equations as implemented in RunDec [73, 74]. The dashed line represents the evolution of the world average [75] and the black circles correspond to the $\alpha_S(Q)$ determinations presented in Table 7.7. Results from other measurements of CMS [1, 35, 44, 63, 64], ATLAS [65], D0 [66, 67], H1 [68, 69], and ZEUS [70] are superimposed.

Chapter 8

Summary

Inclusive multijet production cross-section measured precisely in terms of jet transverse momentum is one of the important observables in understanding physics at hadron colliders. It provides the essential information about the structure of parton through parton distribution functions (PDFs) and the precise measurement of the strong coupling constant α_S. The value of the strong coupling constant at the scale of the Z boson mass $\alpha_s(M_Z)$ can be determined using cross-section ratio instead of individual cross-sections because many uncertainties of theoretical and experimental origin cancel between numerator and denominator which reduces the dependence on PDFs, renormalization and factorization scales, luminosity etc.

In this thesis, a measurement of the inclusive 2-jet and 3-jet event cross-sections as well as the cross-section ratio R_{32} has been presented. The data sample has been collected from proton-proton collisions recorded with the CMS detector at a centre-of-mass energy of 8 TeV and corresponds to an integrated luminosity of $19.7\,\mathrm{fb}^{-1}$. The jets are reconstructed with the anti-k$_t$ clustering algorithm for a jet size parameter R = 0.7. The inclusive 2-jet and 3-jet event cross-sections are measured differentially as a function of the average transverse momentum of the two leading jets, referred as $H_{\mathrm{T},2}/2$. The ratio R_{32} is obtained by dividing the differential cross-sections of inclusive 3-jet events to that of inclusive 2-jet one in each bin of $H_{\mathrm{T},2}/2$. An appropriate selection criteria has been designed for choosing the best events for analysis. The measurements are performed at a central rapidity of $|y| < 2.5$ in a range of $0.3 < H_{\mathrm{T},2}/2 < 2.0\,\mathrm{TeV}$ for inclusive 2-jet event cross-sections and $0.3 < H_{\mathrm{T},2}/2 < 1.68\,\mathrm{TeV}$ for inclusive 3-jet event cross-sections and ratio R_{32}.

The measured cross-sections after correcting for detector effects by using an iterative unfolding procedure are compared to the perturbative QCD predictions computed, using NLOJET++ program, at next-to-leading order (NLO) accuracy and complemented with non-perturbative (NP) corrections that are important at low $H_{\mathrm{T},2}/2$. The data are found to be well described by NLO calculations. The upwards trend observed in the inclusive 2-jet and 3-jet data at high $H_{\mathrm{T},2}/2$ in comparison to the prediction at NLO QCD, is explained by the onset of electroweak (EW) corrections in the 2-jet case. For the 3-jet event cross-sections these corrections have not yet been computed yet. In the 3-jet to 2-jet cross-section ratio R_{32}, the EW corrections are assumed to cancel. In fact, NLO QCD provides an adequate description of R_{32} in the accessible range of $H_{\mathrm{T},2}/2$. In contrast, leading order (LO) tree-level Monte Carlo (MC) predictions obtained using MADGRAPH5 event generator interfaced to PYTHIA6 exhibit significant deviations. The sources of experimental and theoretical uncertainties are studied in details. The experimental uncertainty ranges from 4 to 32% for inclusive 2-jet event cross-sections, from 4 to 28% for 3-jet event cross-sections and from 1 to 28% for cross-section ratio R_{32}. It is dominated by the uncertainty due to the jet energy corrections (JEC) at lower $H_{\mathrm{T},2}/2$ values and by statistical uncertainty at higher $H_{\mathrm{T},2}/2$ values. The theoretical uncertainty ranges from 3 to 30% and 5 to 34% for inclusive 2-jet and 3-jet event cross-sections respectively and from 3 to 11% for ratio R_{32}. The PDF uncertainty derived with the CT10-NLO PDF set is the dominant source of theoretical uncertainty.

The inclusive multijet cross-sections being proportional to the powers of the strong coupling constant α_S ($\sigma_{\text{n-jet}} \propto \alpha_S^{\text{n}}$) are used to extract the value of the strong coupling constant at the scale of the Z boson mass $\alpha_s(M_Z)$. In cross-section ratio R_{32} which proportional to α_S, many uncertainties and PDF dependencies largely cancel and hence becomes the better tool to extract the value of $\alpha_s(M_Z)$. In this thesis, a fit of the ratio of the inclusive 3-jet event cross section to that of 2-jet, R_{32} in the range $0.3 < H_{\text{T},2}/2 < 1.68\,\text{TeV}$ using the MSTW2008 PDF set gives :

$$\begin{aligned}\alpha_s(M_Z) &= 0.1150\ \pm 0.0010\,(\text{exp})\ \pm 0.0013\,(\text{PDF})\ \pm 0.0015\,(\text{NP})\,{}^{+0.0050}_{-0.0000}\,(\text{scale})\\ &= 0.1150\ \pm 0.0023\,(\text{all except scale})\,{}^{+0.0050}_{-0.0000}\,(\text{scale})\end{aligned}$$

Very similar results are obtained using the MMHT2014 PDF set which gives :

$$\begin{aligned}\alpha_s(M_Z) &= 0.1142\ \pm 0.0010\,(\text{exp})\ \pm 0.0013\,(\text{PDF})\ \pm 0.0014\,(\text{NP})\,{}^{+0.0049}_{-0.0006}\,(\text{scale})\\ &= 0.1142\ \pm 0.0022\,(\text{all except scale})\,{}^{+0.0049}_{-0.0006}\,(\text{scale})\end{aligned}$$

The equally compatible values of $\alpha_s(M_Z)$ are determined with separate fits to the inclusive 2-jet and 3-jet event cross-sections provided the range in $H_{\text{T},2}/2$ is restricted to $0.3 < H_{\text{T},2}/2 < 1.0\,\text{TeV}$. The extracted $\alpha_s(M_Z)$ values in sub-ranges of $H_{\text{T},2}/2$ are evolved to corresponding $\alpha_S(Q)$ along with the error bars at different scales Q. The current measurement of $\alpha_s(M_Z)$ and the running of $\alpha_S(Q)$ as a function of Q is in well agreement within uncertainties with the world average value of $\alpha_s(M_Z) = 0.1181 \pm 0.0011$ [75] and already existing determinations performed by the CMS and other experiments.

The inclusion of the EW corrections in inclusive 2-jet event cross-sections become relevant at $H_{\text{T},2}/2$ beyond 1 TeV. Their availability for 3-jet one and hence cross-section ratio R_{32} can improve the precision of the measurement of $\alpha_s(M_Z)$. Also as the theoretical calculations will be available for inclusive 4-jet event cross-sections, the various cross-section ratios such as $R_{43} \propto \alpha_S^1$ and $R_{42} \propto \alpha_S^2$ can be measured to extract the value of the strong coupling constant more precisely. Currently LHC is running at high center-of-mass energy of 13 TeV delivering a higher instantaneous luminosity and this makes possible to access the extended phase space and perform the measurements with more accuracy.

Appendix A

A.1 Cross-section Ratio, R_{32}

Table A.1: Differential cross-sections ($\times\ 10^{-3}$(pb/GeV)) and cross-section ratio R_{32} at detector level in each bin of $H_{\mathrm{T},2}/2$, along with statistical uncertainty (in %).

Bin	2-jet cross-section	Stat. unc.	3-jet cross-section	Stat. unc.	Ratio R_{32}	Stat. unc.
300 - 330	29772.726	0.211	2640.629	0.707	0.089	$^{+0.665}_{-0.661}$
330 - 360	16792.917	0.231	1773.485	0.704	0.106	$^{+0.523}_{-0.521}$
360 - 390	9889.326	0.182	1176.544	0.526	0.119	$^{+0.485}_{-0.483}$
390 - 420	5976.777	0.179	778.034	0.492	0.130	$^{+0.206}_{-0.206}$
420 - 450	3731.760	0.067	522.624	0.180	0.140	$^{+0.167}_{-0.167}$
450 - 480	2398.741	0.084	357.622	0.217	0.149	$^{+0.201}_{-0.200}$
480 - 510	1570.192	0.104	246.051	0.262	0.157	$^{+0.241}_{-0.241}$
510 - 540	1048.665	0.127	171.080	0.314	0.163	$^{+0.288}_{-0.287}$
540 - 570	713.042	0.154	119.566	0.376	0.168	$^{+0.344}_{-0.343}$
570 - 600	490.776	0.186	84.798	0.447	0.173	$^{+0.407}_{-0.406}$
600 - 640	325.046	0.198	57.463	0.470	0.177	$^{+0.427}_{-0.426}$
640 - 680	205.727	0.248	37.282	0.583	0.181	$^{+0.529}_{-0.527}$
680 - 720	133.674	0.308	24.859	0.714	0.186	$^{+0.646}_{-0.643}$
720 - 760	87.911	0.380	16.560	0.875	0.188	$^{+0.791}_{-0.786}$
760 - 800	58.657	0.465	11.056	1.071	0.188	$^{+0.968}_{-0.961}$
800 - 850	38.106	0.516	7.318	1.178	0.192	$^{+1.063}_{-1.054}$
850 - 900	23.587	0.656	4.600	1.485	0.195	$^{+1.339}_{-1.326}$
900 - 950	15.130	0.819	2.896	1.872	0.191	$^{+1.694}_{-1.672}$
950 - 1000	9.696	1.023	1.812	2.366	0.187	$^{+2.151}_{-2.116}$
1000 - 1060	6.026	1.185	1.186	2.670	0.197	$^{+2.414}_{-2.371}$
1060 - 1120	3.668	1.518	0.716	3.436	0.195	$^{+3.118}_{-3.046}$
1120 - 1180	2.327	1.906	0.437	4.398	0.188	$^{+4.024}_{-3.903}$
1180 - 1250	1.419	2.260	0.265	5.227	0.187	$^{+4.798}_{-4.627}$
1250 - 1320	0.853	2.915	0.165	6.623	0.194	$^{+6.080}_{-5.811}$
1320 - 1390	0.477	3.898	0.080	9.492	0.169	$^{+8.951}_{-8.355}$
1390 - 1460	0.263	5.249	0.042	13.131	0.160	$^{+12.619}_{-11.449}$
1460 - 1530	0.192	6.143	0.029	15.811	0.151	$^{+15.437}_{-13.698}$
1530 - 1600	0.104	8.362	0.021	18.570	0.203	$^{+17.571}_{-15.536}$
1600 - 1680	0.060	10.314	0.009	26.726	0.149	$^{+27.132}_{-22.170}$

A.2 Individual Sources of Jet Energy Correction Uncertainties

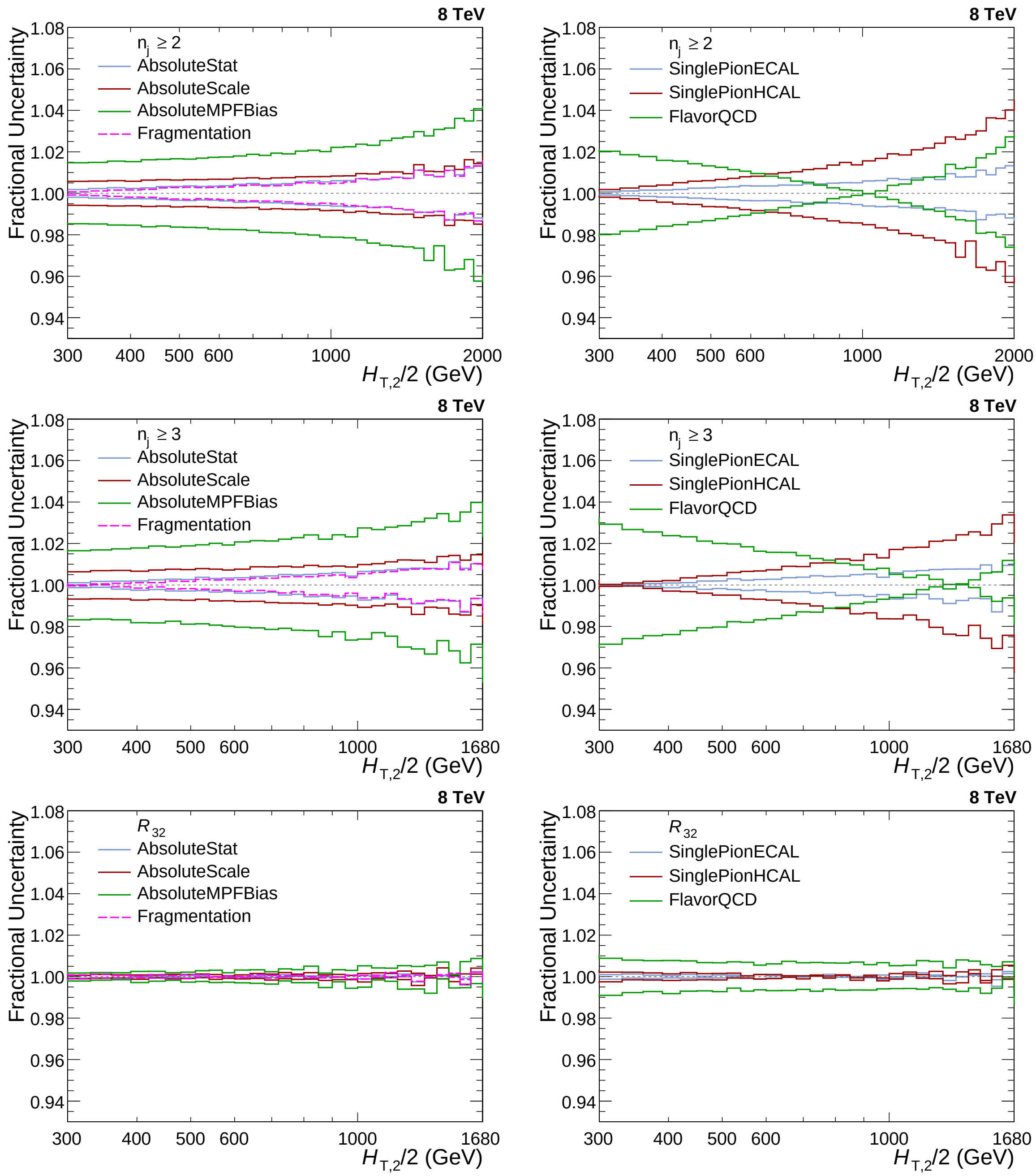

Figure A.1: The fractional jet energy correction (JEC) uncertainties from individual sources are shown for inclusive 2-jet (top) and 3-jet events cross-sections (middle); and cross-section ratio R_{32} (bottom). On left, JEC uncertainties are evaluated from AbsoluteStat (blue), AbsoluteScale (red), AbsoluteMPFBias (green) and Fragmentation (pink) sources whereas on right, these are evaluated from SinglePionECAL (blue), SinglePionHCAL (red) and FlavorQCD (green) sources.

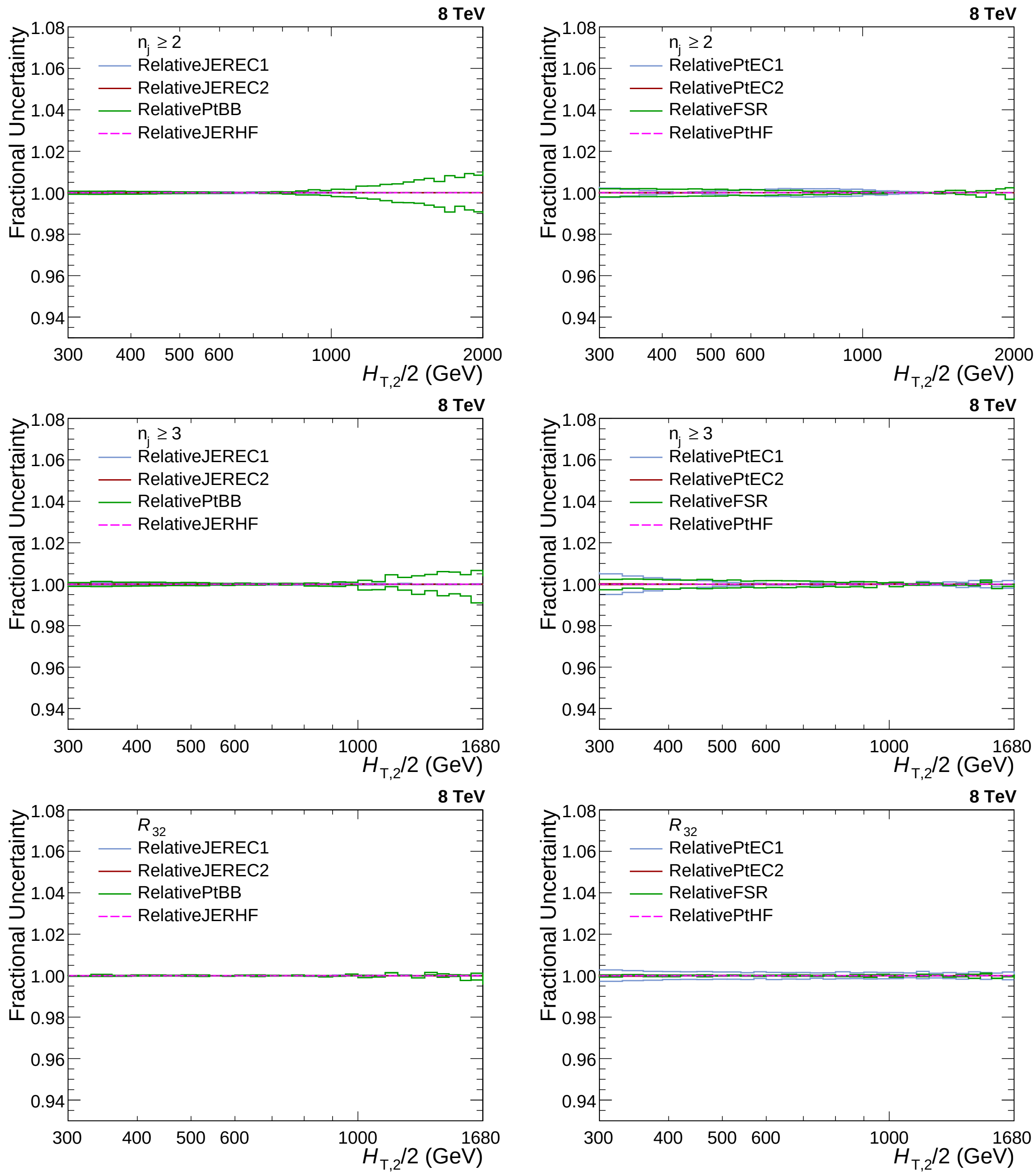

Figure A.2: The fractional jet energy correction (JEC) uncertainties from individual sources are shown for inclusive 2-jet (top) and 3-jet events cross-sections (middle); and cross-section ratio R_{32} (bottom). On left, JEC uncertainties are evaluated from RelativeJEREC1 (blue), RelativeJEREC2 (red), RelativePtBB (green) and RelativeJERHF (pink) sources whereas on right, these are evaluated from RelativePtEC1 (blue), RelativePtEC2 (red), RelativePFSR (green) and RelativePtHF (pink) sources.

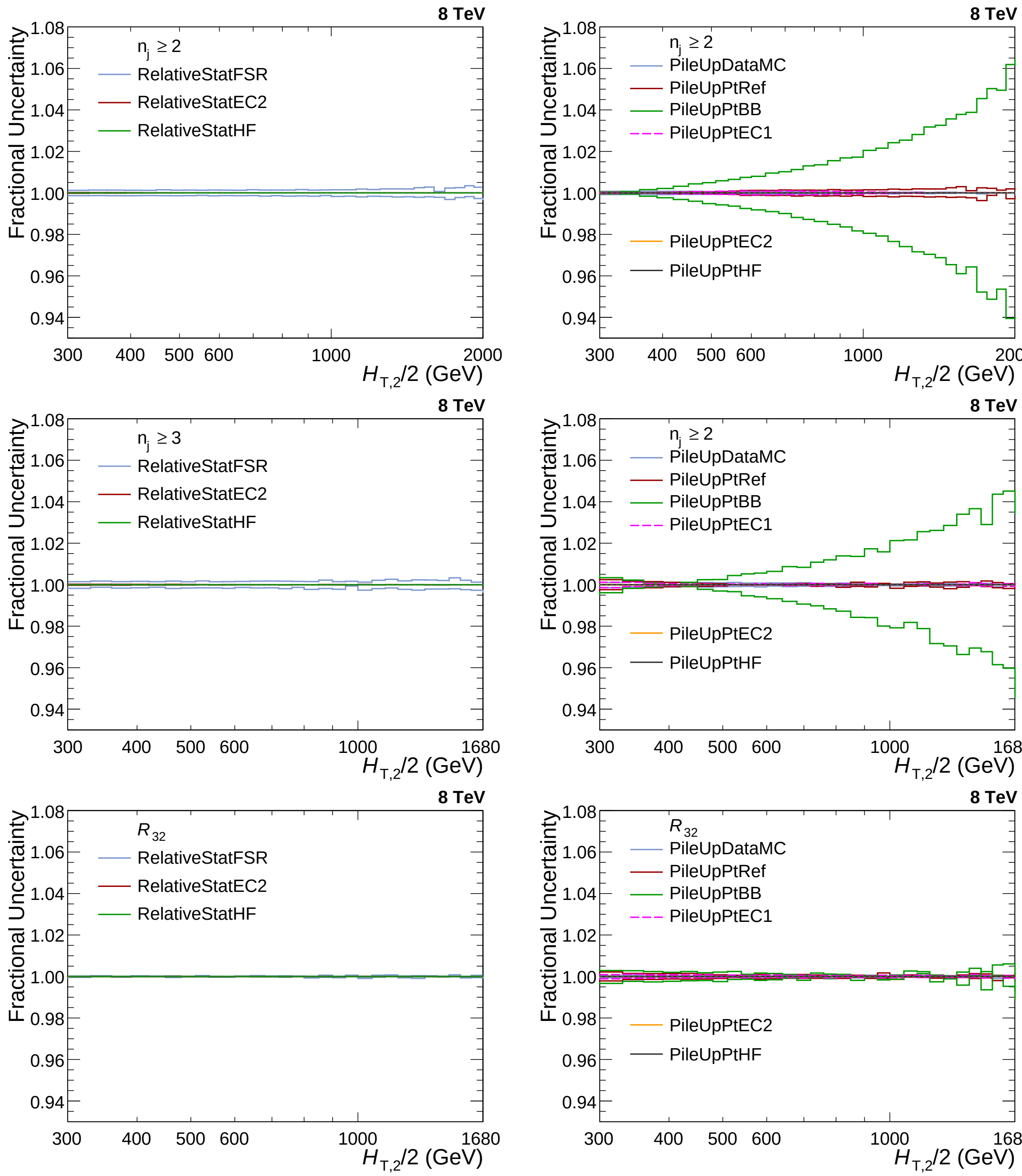

Figure A.3: The fractional jet energy correction (JEC) uncertainties from individual sources are shown for inclusive 2-jet (top) and 3-jet events cross-sections (middle); and cross-section ratio R_{32} (bottom). On left, JEC uncertainties are evaluated from RelativeStatFSR (blue), RelativeStatEC2 (red) and RelativeStatHF (green) sources whereas on right, these are evaluated from PileUpDataMC (blue), PileUpPtRef (red), PileUpPtBB (green), PileUpPtEC1 (pink), PileUpPtEC2 (orange) and PileUpPtHF (black) sources.

A.3 Experimental Uncertainties

Table A.2: Experimental uncertainties (in %), from all sources as well as the total uncertainty, affecting the cross-section measurement in each bin of $H_{\mathrm{T},2}/2$ for inclusive 2-jet events.

Bin	Statistical	JEC	Unfolding	Lumi	Residual	Total
300 - 330	0.242	$^{+2.612}_{-2.565}$	$^{+0.948}_{-0.928}$	2.6	1.0	$^{+3.942}_{-3.906}$
330 - 360	0.258	$^{+2.507}_{-2.473}$	$^{+0.976}_{-0.969}$	2.6	1.0	$^{+3.882}_{-3.858}$
360 - 390	0.202	$^{+2.504}_{-2.465}$	$^{+0.779}_{-0.783}$	2.6	1.0	$^{+3.831}_{-3.807}$
390 - 420	0.193	$^{+2.363}_{-2.381}$	$^{+0.905}_{-0.904}$	2.6	1.0	$^{+3.768}_{-3.780}$
420 - 450	0.084	$^{+2.448}_{-2.422}$	$^{+0.904}_{-0.895}$	2.6	1.0	$^{+3.818}_{-3.799}$
450 - 480	0.096	$^{+2.440}_{-2.352}$	$^{+0.797}_{-0.795}$	2.6	1.0	$^{+3.789}_{-3.733}$
480 - 510	0.107	$^{+2.427}_{-2.406}$	$^{+0.728}_{-0.715}$	2.6	1.0	$^{+3.767}_{-3.751}$
510 - 540	0.128	$^{+2.425}_{-2.395}$	$^{+0.835}_{-0.862}$	2.6	1.0	$^{+3.789}_{-3.775}$
540 - 570	0.154	$^{+2.425}_{-2.376}$	$^{+0.687}_{-0.674}$	2.6	1.0	$^{+3.760}_{-3.726}$
570 - 600	0.180	$^{+2.497}_{-2.474}$	$^{+0.839}_{-0.827}$	2.6	1.0	$^{+3.838}_{-3.820}$
600 - 640	0.209	$^{+2.495}_{-2.491}$	$^{+0.744}_{-0.743}$	2.6	1.0	$^{+3.819}_{-3.816}$
640 - 680	0.264	$^{+2.582}_{-2.545}$	$^{+0.912}_{-0.912}$	2.6	1.0	$^{+3.915}_{-3.891}$
680 - 720	0.320	$^{+2.691}_{-2.574}$	$^{+0.763}_{-0.756}$	2.6	1.0	$^{+3.961}_{-3.880}$
720 - 760	0.387	$^{+2.690}_{-2.755}$	$^{+0.705}_{-0.712}$	2.6	1.0	$^{+3.955}_{-4.001}$
760 - 800	0.465	$^{+2.858}_{-2.846}$	$^{+0.859}_{-0.846}$	2.6	1.0	$^{+4.109}_{-4.098}$
800 - 850	0.548	$^{+2.889}_{-2.913}$	$^{+0.783}_{-0.787}$	2.6	1.0	$^{+4.126}_{-4.143}$
850 - 900	0.698	$^{+3.145}_{-3.102}$	$^{+0.961}_{-0.958}$	2.6	1.0	$^{+4.366}_{-4.334}$
900 - 950	0.847	$^{+3.298}_{-3.233}$	$^{+0.828}_{-0.829}$	2.6	1.0	$^{+4.476}_{-4.429}$
950 - 1000	1.041	$^{+3.291}_{-3.330}$	$^{+0.895}_{-0.872}$	2.6	1.0	$^{+4.525}_{-4.549}$
1000 - 1060	1.268	$^{+3.598}_{-3.569}$	$^{+0.945}_{-0.956}$	2.6	1.0	$^{+4.817}_{-4.798}$
1060 - 1120	1.611	$^{+3.759}_{-3.756}$	$^{+0.970}_{-0.967}$	2.6	1.0	$^{+5.043}_{-5.040}$
1120 - 1180	1.985	$^{+4.154}_{-4.053}$	$^{+1.089}_{-1.080}$	2.6	1.0	$^{+5.490}_{-5.413}$
1180 - 1250	2.406	$^{+4.251}_{-4.313}$	$^{+1.062}_{-1.070}$	2.6	1.0	$^{+5.722}_{-5.770}$
1250 - 1320	3.101	$^{+4.696}_{-4.624}$	$^{+1.151}_{-1.144}$	2.6	1.0	$^{+6.384}_{-6.330}$
1320 - 1390	4.157	$^{+4.934}_{-4.979}$	$^{+1.343}_{-1.341}$	2.6	1.0	$^{+7.155}_{-7.186}$
1390 - 1460	5.270	$^{+5.148}_{-5.104}$	$^{+1.185}_{-1.177}$	2.6	1.0	$^{+7.965}_{-7.936}$
1460 - 1530	6.360	$^{+5.890}_{-5.652}$	$^{+1.405}_{-1.406}$	2.6	1.0	$^{+9.213}_{-9.063}$
1530 - 1600	8.183	$^{+5.924}_{-6.311}$	$^{+1.598}_{-1.590}$	2.6	1.0	$^{+10.601}_{-10.821}$
1600 - 1680	10.630	$^{+5.969}_{-5.655}$	$^{+1.607}_{-1.592}$	2.6	1.0	$^{+12.608}_{-12.461}$
1680 - 1760	13.864	$^{+7.245}_{-7.603}$	$^{+1.821}_{-1.839}$	2.6	1.0	$^{+15.993}_{-16.161}$
1760 - 1840	18.192	$^{+7.781}_{-7.820}$	$^{+1.902}_{-1.906}$	2.6	1.0	$^{+20.071}_{-20.087}$
1840 - 1920	22.612	$^{+7.647}_{-7.537}$	$^{+1.588}_{-1.590}$	2.6	1.0	$^{+24.085}_{-24.050}$
1920 - 2000	29.530	$^{+9.199}_{-9.469}$	$^{+1.511}_{-1.505}$	2.6	1.0	$^{+31.092}_{-31.172}$

Table A.3: Experimental uncertainties (in %), from all sources as well as the total uncertainty, affecting the cross-section measurement in each bin of $H_{\mathrm{T},2}/2$ for inclusive 3-jet events.

Bin	**Statistical**	**JEC**	**Unfolding**	**Lumi**	**Residual**	**Total**
300 - 330	0.796	$^{+3.503}_{-3.475}$	$^{+0.564}_{-0.552}$	2.6	1.0	$^{+4.581}_{-4.558}$
330 - 360	0.781	$^{+3.303}_{-3.186}$	$^{+0.640}_{-0.633}$	2.6	1.0	$^{+4.437}_{-4.350}$
360 - 390	0.583	$^{+3.221}_{-3.094}$	$^{+0.490}_{-0.496}$	2.6	1.0	$^{+4.326}_{-4.233}$
390 - 420	0.531	$^{+3.092}_{-3.149}$	$^{+0.584}_{-0.584}$	2.6	1.0	$^{+4.236}_{-4.278}$
420 - 450	0.224	$^{+3.125}_{-2.996}$	$^{+0.604}_{-0.592}$	2.6	1.0	$^{+4.236}_{-4.140}$
450 - 480	0.248	$^{+2.984}_{-2.890}$	$^{+0.531}_{-0.528}$	2.6	1.0	$^{+4.124}_{-4.056}$
480 - 510	0.269	$^{+2.937}_{-2.963}$	$^{+0.511}_{-0.512}$	2.6	1.0	$^{+4.089}_{-4.108}$
510 - 540	0.318	$^{+3.021}_{-2.797}$	$^{+0.592}_{-0.612}$	2.6	1.0	$^{+4.164}_{-4.007}$
540 - 570	0.375	$^{+2.999}_{-2.935}$	$^{+0.506}_{-0.500}$	2.6	1.0	$^{+4.141}_{-4.094}$
570 - 600	0.434	$^{+2.824}_{-2.906}$	$^{+0.646}_{-0.620}$	2.6	1.0	$^{+4.042}_{-4.096}$
600 - 640	0.497	$^{+2.952}_{-2.956}$	$^{+0.598}_{-0.604}$	2.6	1.0	$^{+4.133}_{-4.136}$
640 - 680	0.617	$^{+3.111}_{-3.001}$	$^{+0.777}_{-0.786}$	2.6	1.0	$^{+4.292}_{-4.215}$
680 - 720	0.739	$^{+3.067}_{-2.984}$	$^{+0.642}_{-0.611}$	2.6	1.0	$^{+4.257}_{-4.194}$
720 - 760	0.895	$^{+3.185}_{-3.111}$	$^{+0.595}_{-0.607}$	2.6	1.0	$^{+4.366}_{-4.313}$
760 - 800	1.068	$^{+3.231}_{-3.166}$	$^{+0.763}_{-0.774}$	2.6	1.0	$^{+4.464}_{-4.419}$
800 - 850	1.250	$^{+3.427}_{-3.295}$	$^{+0.674}_{-0.687}$	2.6	1.0	$^{+4.639}_{-4.544}$
850 - 900	1.578	$^{+3.364}_{-3.540}$	$^{+0.903}_{-0.898}$	2.6	1.0	$^{+4.731}_{-4.857}$
900 - 950	1.961	$^{+3.594}_{-3.524}$	$^{+0.792}_{-0.793}$	2.6	1.0	$^{+5.015}_{-4.965}$
950 - 1000	2.420	$^{+3.603}_{-3.783}$	$^{+0.846}_{-0.843}$	2.6	1.0	$^{+5.226}_{-5.351}$
1000 - 1060	2.844	$^{+4.164}_{-4.116}$	$^{+0.916}_{-0.940}$	2.6	1.0	$^{+5.834}_{-5.803}$
1060 - 1120	3.647	$^{+4.038}_{-3.815}$	$^{+0.963}_{-0.957}$	2.6	1.0	$^{+6.188}_{-6.044}$
1120 - 1180	4.607	$^{+4.278}_{-4.183}$	$^{+1.084}_{-1.087}$	2.6	1.0	$^{+6.961}_{-6.904}$
1180 - 1250	5.532	$^{+4.894}_{-4.771}$	$^{+1.074}_{-1.069}$	2.6	1.0	$^{+7.967}_{-7.891}$
1250 - 1320	7.141	$^{+5.144}_{-5.273}$	$^{+1.222}_{-1.217}$	2.6	1.0	$^{+9.312}_{-9.383}$
1320 - 1390	10.207	$^{+5.542}_{-5.642}$	$^{+1.414}_{-1.428}$	2.6	1.0	$^{+12.027}_{-12.076}$
1390 - 1460	13.831	$^{+5.630}_{-5.265}$	$^{+1.257}_{-1.256}$	2.6	1.0	$^{+15.242}_{-15.111}$
1460 - 1530	15.578	$^{+5.576}_{-5.491}$	$^{+1.546}_{-1.551}$	2.6	1.0	$^{+16.850}_{-16.822}$
1530 - 1600	18.729	$^{+6.409}_{-7.019}$	$^{+1.718}_{-1.716}$	2.6	1.0	$^{+20.063}_{-20.266}$
1600 - 1680	26.465	$^{+7.017}_{-6.255}$	$^{+1.775}_{-1.765}$	2.6	1.0	$^{+27.578}_{-27.393}$

Table A.4: Experimental uncertainties (in %), from all sources as well as the total uncertainty, affecting the measurement of cross-section ratio R_{32}, in each bin of $H_{\mathrm{T},2}/2$.

Bin	**Statistical**	**JEC**	**Unfolding**	**Total**
300 - 330	0.741	$^{+1.059}_{-1.097}$	$^{+0.754}_{-0.751}$	$^{+1.496}_{-1.522}$
330 - 360	0.587	$^{+0.954}_{-0.923}$	$^{+0.685}_{-0.689}$	$^{+1.313}_{-1.292}$
360 - 390	0.519	$^{+0.902}_{-0.855}$	$^{+0.594}_{-0.593}$	$^{+1.199}_{-1.163}$
390 - 420	0.236	$^{+0.907}_{-0.952}$	$^{+0.439}_{-0.438}$	$^{+1.035}_{-1.074}$
420 - 450	0.192	$^{+0.900}_{-0.835}$	$^{+0.360}_{-0.361}$	$^{+0.988}_{-0.930}$
450 - 480	0.209	$^{+0.788}_{-0.802}$	$^{+0.307}_{-0.308}$	$^{+0.872}_{-0.884}$
480 - 510	0.245	$^{+0.795}_{-0.867}$	$^{+0.254}_{-0.235}$	$^{+0.870}_{-0.931}$
510 - 540	0.287	$^{+0.852}_{-0.682}$	$^{+0.264}_{-0.268}$	$^{+0.937}_{-0.787}$
540 - 570	0.326	$^{+0.807}_{-0.803}$	$^{+0.193}_{-0.189}$	$^{+0.891}_{-0.887}$
570 - 600	0.397	$^{+0.656}_{-0.774}$	$^{+0.199}_{-0.219}$	$^{+0.792}_{-0.898}$
600 - 640	0.447	$^{+0.763}_{-0.797}$	$^{+0.150}_{-0.154}$	$^{+0.897}_{-0.926}$
640 - 680	0.573	$^{+0.861}_{-0.781}$	$^{+0.153}_{-0.140}$	$^{+1.045}_{-0.979}$
680 - 720	0.663	$^{+0.766}_{-0.787}$	$^{+0.147}_{-0.164}$	$^{+1.024}_{-1.042}$
720 - 760	0.774	$^{+0.842}_{-0.769}$	$^{+0.118}_{-0.118}$	$^{+1.149}_{-1.097}$
760 - 800	0.970	$^{+0.800}_{-0.729}$	$^{+0.115}_{-0.096}$	$^{+1.263}_{-1.218}$
800 - 850	1.116	$^{+0.873}_{-0.775}$	$^{+0.115}_{-0.104}$	$^{+1.422}_{-1.363}$
850 - 900	1.436	$^{+0.770}_{-0.896}$	$^{+0.069}_{-0.069}$	$^{+1.631}_{-1.694}$
900 - 950	1.716	$^{+0.704}_{-0.752}$	$^{+0.050}_{-0.051}$	$^{+1.855}_{-1.874}$
950 - 1000	2.156	$^{+0.824}_{-0.897}$	$^{+0.089}_{-0.045}$	$^{+2.310}_{-2.336}$
1000 - 1060	2.554	$^{+0.812}_{-0.870}$	$^{+0.045}_{-0.040}$	$^{+2.680}_{-2.698}$
1060 - 1120	3.244	$^{+0.792}_{-0.658}$	$^{+0.018}_{-0.027}$	$^{+3.339}_{-3.310}$
1120 - 1180	4.121	$^{+0.985}_{-0.757}$	$^{+0.025}_{-0.043}$	$^{+4.237}_{-4.191}$
1180 - 1250	4.990	$^{+1.031}_{-0.848}$	$^{+0.023}_{-0.041}$	$^{+5.095}_{-5.062}$
1250 - 1320	6.456	$^{+0.750}_{-1.087}$	$^{+0.079}_{-0.079}$	$^{+6.500}_{-6.548}$
1320 - 1390	8.990	$^{+1.112}_{-1.144}$	$^{+0.080}_{-0.099}$	$^{+9.059}_{-9.063}$
1390 - 1460	12.699	$^{+1.157}_{-0.815}$	$^{+0.076}_{-0.078}$	$^{+12.751}_{-12.725}$
1460 - 1530	13.926	$^{+0.768}_{-1.235}$	$^{+0.143}_{-0.145}$	$^{+13.948}_{-13.981}$
1530 - 1600	16.903	$^{+1.050}_{-1.258}$	$^{+0.120}_{-0.127}$	$^{+16.936}_{-16.950}$
1600 - 1680	28.070	$^{+1.471}_{-0.859}$	$^{+0.178}_{-0.177}$	$^{+28.109}_{-28.084}$

A.4 Theoretical Uncertainties

Table A.5: Theoretical uncertainties (in %) calculating using CT10-NLO PDF set from all sources as well as the total uncertainty, affecting the cross-section measurement in each bin of $H_{\mathrm{T},2}/2$ for inclusive 2-jet events.

Bin	Scale	PDF	NP	Total
300 - 330	$^{+0.942}_{-6.149}$	$^{+3.566}_{-3.090}$	0.825	$^{+3.780}_{-6.931}$
330 - 360	$^{+1.035}_{-6.289}$	$^{+3.906}_{-3.342}$	0.736	$^{+4.107}_{-7.159}$
360 - 390	$^{+1.159}_{-6.438}$	$^{+4.232}_{-3.573}$	0.696	$^{+4.442}_{-7.396}$
390 - 420	$^{+1.220}_{-6.536}$	$^{+4.551}_{-3.794}$	0.723	$^{+4.767}_{-7.592}$
420 - 450	$^{+1.326}_{-6.660}$	$^{+4.857}_{-3.997}$	0.745	$^{+5.089}_{-7.802}$
450 - 480	$^{+1.421}_{-6.776}$	$^{+5.153}_{-4.186}$	0.765	$^{+5.399}_{-8.001}$
480 - 510	$^{+1.512}_{-6.888}$	$^{+5.444}_{-4.365}$	0.782	$^{+5.704}_{-8.192}$
510 - 540	$^{+1.566}_{-6.967}$	$^{+5.721}_{-4.527}$	0.797	$^{+5.984}_{-8.347}$
540 - 570	$^{+1.666}_{-7.082}$	$^{+6.000}_{-4.682}$	0.810	$^{+6.279}_{-8.528}$
570 - 600	$^{+1.731}_{-7.172}$	$^{+6.269}_{-4.825}$	0.822	$^{+6.555}_{-8.683}$
600 - 640	$^{+1.805}_{-7.271}$	$^{+6.597}_{-4.979}$	0.833	$^{+6.890}_{-8.852}$
640 - 680	$^{+1.930}_{-7.416}$	$^{+6.978}_{-5.143}$	0.845	$^{+7.289}_{-9.064}$
680 - 720	$^{+2.007}_{-7.527}$	$^{+7.364}_{-5.295}$	0.856	$^{+7.680}_{-9.243}$
720 - 760	$^{+2.113}_{-7.663}$	$^{+7.749}_{-5.437}$	0.865	$^{+8.078}_{-9.436}$
760 - 800	$^{+2.196}_{-7.781}$	$^{+8.140}_{-5.569}$	0.873	$^{+8.476}_{-9.609}$
800 - 850	$^{+2.323}_{-7.945}$	$^{+8.573}_{-5.706}$	0.881	$^{+8.926}_{-9.822}$
850 - 900	$^{+2.389}_{-8.062}$	$^{+9.082}_{-5.863}$	0.889	$^{+9.433}_{-10.008}$
900 - 950	$^{+2.499}_{-8.227}$	$^{+9.600}_{-6.018}$	0.896	$^{+9.961}_{-10.232}$
950 - 1000	$^{+2.631}_{-8.402}$	$^{+10.134}_{-6.166}$	0.902	$^{+10.509}_{-10.460}$
1000 - 1060	$^{+2.738}_{-8.569}$	$^{+10.747}_{-6.343}$	0.908	$^{+11.127}_{-10.700}$
1060 - 1120	$^{+2.853}_{-8.751}$	$^{+11.431}_{-6.526}$	0.914	$^{+11.817}_{-10.955}$
1120 - 1180	$^{+2.992}_{-8.970}$	$^{+12.183}_{-6.727}$	0.919	$^{+12.579}_{-11.250}$
1180 - 1250	$^{+3.135}_{-9.194}$	$^{+13.019}_{-6.944}$	0.924	$^{+13.423}_{-11.558}$
1250 - 1320	$^{+3.324}_{-9.469}$	$^{+14.004}_{-7.189}$	0.929	$^{+14.423}_{-11.925}$
1320 - 1390	$^{+3.434}_{-9.677}$	$^{+15.080}_{-7.444}$	0.933	$^{+15.494}_{-12.244}$
1390 - 1460	$^{+3.629}_{-9.976}$	$^{+16.223}_{-7.700}$	0.937	$^{+16.650}_{-12.637}$
1460 - 1530	$^{+3.760}_{-10.224}$	$^{+17.505}_{-7.980}$	0.940	$^{+17.929}_{-13.004}$
1530 - 1600	$^{+3.894}_{-10.471}$	$^{+18.891}_{-8.258}$	0.943	$^{+19.311}_{-13.368}$
1600 - 1680	$^{+4.107}_{-10.813}$	$^{+20.496}_{-8.560}$	0.946	$^{+20.925}_{-13.824}$
1680 - 1760	$^{+4.421}_{-11.101}$	$^{+22.481}_{-8.905}$	0.949	$^{+22.931}_{-14.263}$
1760 - 1840	$^{+4.921}_{-11.461}$	$^{+24.654}_{-9.251}$	0.951	$^{+25.158}_{-14.760}$
1840 - 1920	$^{+5.404}_{-11.813}$	$^{+27.143}_{-9.607}$	0.953	$^{+27.692}_{-15.256}$
1920 - 2000	$^{+5.867}_{-12.154}$	$^{+29.986}_{-9.973}$	0.955	$^{+30.570}_{-15.751}$

Table A.6: Theoretical uncertainties (in %) calculating using CT10-NLO PDF set from all sources as well as the total uncertainty, affecting the cross-section measurement in each bin of $H_{\mathrm{T},2}/2$ for inclusive 3-jet events.

Bin	**Scale**	**PDF**	**NP**	**Total**
300 - 330	$^{+0.539}_{-8.294}$	$^{+5.716}_{-4.657}$	1.692	$^{+5.986}_{-9.662}$
330 - 360	$^{+0.550}_{-8.577}$	$^{+5.977}_{-4.779}$	1.516	$^{+6.191}_{-9.935}$
360 - 390	$^{+0.599}_{-8.709}$	$^{+6.187}_{-4.987}$	1.363	$^{+6.363}_{-10.128}$
390 - 420	$^{+0.719}_{-8.948}$	$^{+6.751}_{-5.223}$	1.228	$^{+6.900}_{-10.433}$
420 - 450	$^{+0.799}_{-9.145}$	$^{+7.031}_{-5.395}$	1.110	$^{+7.162}_{-10.676}$
450 - 480	$^{+0.847}_{-9.247}$	$^{+7.404}_{-5.578}$	1.005	$^{+7.520}_{-10.845}$
480 - 510	$^{+0.847}_{-9.294}$	$^{+7.837}_{-5.717}$	0.937	$^{+7.938}_{-10.951}$
510 - 540	$^{+0.922}_{-9.436}$	$^{+8.198}_{-5.884}$	0.921	$^{+8.301}_{-11.158}$
540 - 570	$^{+0.974}_{-9.566}$	$^{+8.529}_{-6.000}$	0.904	$^{+8.632}_{-11.328}$
570 - 600	$^{+1.086}_{-9.786}$	$^{+8.970}_{-6.156}$	0.886	$^{+9.079}_{-11.595}$
600 - 640	$^{+1.107}_{-9.852}$	$^{+9.402}_{-6.297}$	0.866	$^{+9.506}_{-11.724}$
640 - 680	$^{+1.278}_{-10.101}$	$^{+10.310}_{-6.526}$	0.842	$^{+10.423}_{-12.055}$
680 - 720	$^{+1.384}_{-10.342}$	$^{+9.682}_{-6.618}$	0.820	$^{+9.815}_{-12.305}$
720 - 760	$^{+1.415}_{-10.404}$	$^{+11.051}_{-6.826}$	0.798	$^{+11.170}_{-12.469}$
760 - 800	$^{+1.547}_{-10.615}$	$^{+11.565}_{-7.009}$	0.777	$^{+11.694}_{-12.744}$
800 - 850	$^{+1.679}_{-10.804}$	$^{+12.242}_{-7.185}$	0.755	$^{+12.379}_{-12.997}$
850 - 900	$^{+2.085}_{-11.134}$	$^{+13.097}_{-7.461}$	0.731	$^{+13.282}_{-13.422}$
900 - 950	$^{+2.475}_{-11.432}$	$^{+13.889}_{-7.703}$	0.709	$^{+14.125}_{-13.804}$
950 - 1000	$^{+2.655}_{-11.608}$	$^{+14.614}_{-7.915}$	0.688	$^{+14.869}_{-14.066}$
1000 - 1060	$^{+3.025}_{-11.926}$	$^{+15.576}_{-8.173}$	0.667	$^{+15.881}_{-14.473}$
1060 - 1120	$^{+3.299}_{-12.189}$	$^{+14.250}_{-8.441}$	0.645	$^{+14.641}_{-14.840}$
1120 - 1180	$^{+3.741}_{-12.584}$	$^{+17.984}_{-8.787}$	0.625	$^{+18.380}_{-15.361}$
1180 - 1250	$^{+3.969}_{-12.843}$	$^{+19.324}_{-9.127}$	0.625	$^{+19.737}_{-15.768}$
1250 - 1320	$^{+4.663}_{-13.452}$	$^{+21.246}_{-9.517}$	0.642	$^{+21.761}_{-16.490}$
1320 - 1390	$^{+4.878}_{-13.702}$	$^{+22.884}_{-9.899}$	0.657	$^{+23.407}_{-16.916}$
1390 - 1460	$^{+5.242}_{-14.095}$	$^{+24.854}_{-10.332}$	0.670	$^{+25.410}_{-17.489}$
1460 - 1530	$^{+5.582}_{-14.464}$	$^{+27.170}_{-10.733}$	0.682	$^{+27.746}_{-18.024}$
1530 - 1600	$^{+6.003}_{-14.907}$	$^{+29.741}_{-11.165}$	0.692	$^{+30.349}_{-18.637}$
1600 - 1680	$^{+6.503}_{-15.418}$	$^{+32.855}_{-11.617}$	0.702	$^{+33.500}_{-19.317}$

Table A.7: Theoretical uncertainties (in %) calculating using CT10-NLO PDF set from all sources as well as the total uncertainty, affecting the measurement of cross-section ratio R_{32}, in each bin of $H_{\mathrm{T},2}/2$.

Bin	**Scale**	**PDF**	**NP**	**Total**
300 - 330	$^{+0.038}_{-7.203}$	$^{+2.458}_{-3.463}$	0.822	$^{+2.592}_{-8.035}$
330 - 360	$^{+0.027}_{-6.626}$	$^{+2.317}_{-3.378}$	0.734	$^{+2.431}_{-7.474}$
360 - 390	$^{+0.024}_{-6.449}$	$^{+2.149}_{-3.367}$	0.656	$^{+2.247}_{-7.304}$
390 - 420	$^{+0.084}_{-5.894}$	$^{+2.411}_{-3.383}$	0.586	$^{+2.482}_{-6.821}$
420 - 450	$^{+0.113}_{-5.532}$	$^{+2.345}_{-3.362}$	0.523	$^{+2.405}_{-6.494}$
450 - 480	$^{+0.109}_{-5.409}$	$^{+2.390}_{-3.357}$	0.467	$^{+2.438}_{-6.383}$
480 - 510	$^{+0.073}_{-5.442}$	$^{+2.506}_{-3.327}$	0.416	$^{+2.541}_{-6.392}$
510 - 540	$^{+0.107}_{-5.168}$	$^{+2.559}_{-3.326}$	0.371	$^{+2.588}_{-6.157}$
540 - 570	$^{+0.112}_{-5.010}$	$^{+2.586}_{-3.292}$	0.330	$^{+2.609}_{-6.004}$
570 - 600	$^{+0.163}_{-4.576}$	$^{+2.729}_{-3.292}$	0.292	$^{+2.750}_{-5.645}$
600 - 640	$^{+0.146}_{-4.565}$	$^{+2.824}_{-3.270}$	0.253	$^{+2.839}_{-5.621}$
640 - 680	$^{+0.198}_{-4.163}$	$^{+3.368}_{-3.298}$	0.236	$^{+3.382}_{-5.316}$
680 - 720	$^{+0.155}_{-3.754}$	$^{+2.352}_{-3.247}$	0.227	$^{+2.368}_{-4.968}$
720 - 760	$^{+0.196}_{-3.842}$	$^{+3.267}_{-3.268}$	0.219	$^{+3.280}_{-5.049}$
760 - 800	$^{+0.126}_{-3.523}$	$^{+3.366}_{-3.272}$	0.212	$^{+3.375}_{-4.813}$
800 - 850	$^{+0.110}_{-3.368}$	$^{+3.596}_{-3.261}$	0.206	$^{+3.604}_{-4.693}$
850 - 900	$^{+0.048}_{-3.351}$	$^{+3.909}_{-3.309}$	0.200	$^{+3.915}_{-4.714}$
900 - 950	$^{+0.116}_{-3.504}$	$^{+4.148}_{-3.334}$	0.196	$^{+4.154}_{-4.841}$
950 - 1000	$^{+0.127}_{-3.511}$	$^{+4.300}_{-3.335}$	0.192	$^{+4.306}_{-4.846}$
1000 - 1060	$^{+0.282}_{-3.683}$	$^{+4.604}_{-3.357}$	0.204	$^{+4.617}_{-4.988}$
1060 - 1120	$^{+0.436}_{-3.779}$	$^{+3.079}_{-3.375}$	0.224	$^{+3.118}_{-5.071}$
1120 - 1180	$^{+0.732}_{-3.982}$	$^{+5.430}_{-3.452}$	0.241	$^{+5.485}_{-5.276}$
1180 - 1250	$^{+0.813}_{-4.031}$	$^{+5.835}_{-3.511}$	0.258	$^{+5.897}_{-5.352}$
1250 - 1320	$^{+1.303}_{-4.414}$	$^{+6.626}_{-3.591}$	0.275	$^{+6.759}_{-5.697}$
1320 - 1390	$^{+1.403}_{-4.471}$	$^{+7.036}_{-3.659}$	0.290	$^{+7.180}_{-5.785}$
1390 - 1460	$^{+1.564}_{-4.590}$	$^{+7.657}_{-3.778}$	0.304	$^{+7.822}_{-5.953}$
1460 - 1530	$^{+1.765}_{-4.738}$	$^{+8.438}_{-3.853}$	0.316	$^{+8.626}_{-6.115}$
1530 - 1600	$^{+2.040}_{-4.972}$	$^{+9.306}_{-3.962}$	0.328	$^{+9.532}_{-6.366}$
1600 - 1680	$^{+2.313}_{-5.179}$	$^{+10.381}_{-4.075}$	0.339	$^{+10.641}_{-6.599}$

Bibliography

[1] S. Chatrchyan *et al.*, "Measurement of the ratio of the inclusive 3-jet cross section to the inclusive 2-jet cross section in pp collisions at $\sqrt{s} = 7$ TeV and first determination of the strong coupling constant in the TeV range," *Eur. Phys. J.*, vol. C73, no. 10, p. 2604, 2013.

[2] L. Evans and P. Bryant, "LHC Machine," *JINST*, vol. 3, p. S08001, 2008.

[3] S. Myers and E. Picasso, "The design, construction and commissioning of the cern large electron–positron collider," *Contemporary Physics*, vol. 31, no. 6, pp. 387–403, 1990.

[4] K. Aamodt *et al.*, "The ALICE experiment at the CERN LHC," *JINST*, vol. 3, p. S08002, 2008.

[5] G. Aad *et al.*, "The ATLAS Experiment at the CERN Large Hadron Collider," *JINST*, vol. 3, p. S08003, 2008.

[6] S. Chatrchyan *et al.*, "The CMS Experiment at the CERN LHC," *JINST*, vol. 3, p. S08004, 2008.

[7] G. L. Bayatian *et al.*, "CMS Physics," 2006.

[8] G. L. Bayatian *et al.*, "CMS technical design report, volume II: Physics performance," *J. Phys.*, vol. G34, no. 6, pp. 995–1579, 2007.

[9] A. A. Alves, Jr. *et al.*, “The LHCb Detector at the LHC,” *JINST*, vol. 3, p. S08005, 2008.

[10] O. Adriani *et al.*, “The LHCf detector at the CERN Large Hadron Collider,” *JINST*, vol. 3, p. S08006, 2008.

[11] G. Anelli *et al.*, “The TOTEM experiment at the CERN Large Hadron Collider,” *JINST*, vol. 3, p. S08007, 2008.

[12] C. Collaboration, “CMS Luminosity Based on Pixel Cluster Counting - Summer 2013 Update,” 2013.

[13] S. van der Meer, “Calibration of the Effective Beam Height in the ISR,” 1968.

[14] P. Adzic *et al.*, “Energy resolution of the barrel of the CMS electromagnetic calorimeter,” *JINST*, vol. 2, p. P04004, 2007.

[15] S. Chatrchyan *et al.*, “Performance of the CMS Hadron Calorimeter with Cosmic Ray Muons and LHC Beam Data,” *JINST*, vol. 5, p. T03012, 2010.

[16] T. Schörner-Sadenius, ed., *The Large Hadron Collider*. Berlin: Springer, 2015.

[17] “Particle-Flow Event Reconstruction in CMS and Performance for Jets, Taus, and MET,” 2009.

[18] “Commissioning of the Particle-flow Event Reconstruction with the first LHC collisions recorded in the CMS detector,” 2010.

[19] W. Adam, B. Mangano, T. Speer, and T. Todorov, “Track reconstruction in the CMS tracker,” 2005.

[20] J. Alwall, M. Herquet, F. Maltoni, O. Mattelaer, and T. Stelzer, “MadGraph 5 : Going Beyond,” *JHEP*, vol. 06, p. 128, 2011.

[21] T. Sjostrand, S. Mrenna, and P. Z. Skands, “PYTHIA 6.4 Physics and Manual,” *JHEP*, vol. 05, p. 026, 2006.

[22] J. Alwall *et al.*, "A Standard format for Les Houches event files," *Comput. Phys. Commun.*, vol. 176, pp. 300–304, 2007.

[23] C. J. Clopper and E. S. Pearson, "The use of confidence or fiducial limits illustrated in the case of the binomial," *Biometrika*, vol. 26, no. 4, pp. 404–413, 1934.

[24] C. Collaboration, "Jet Performance in pp Collisions at 7 TeV," 2010.

[25] C. Collaboration, "Jet Identification at 8 TeV." `https://twiki.cern.ch/twiki/bin/viewauth/CMS/JetID`, 2012. (accessed on 2017-10-31).

[26] C. Collaboration, "Jet Energy Resolution at 8 TeV." `https://twiki.cern.ch/twiki/bin/viewauth/CMS/JetResolution`, 2012. (accessed on 2016-01-22).

[27] C. Collaboration, "Jet Energy Resolution in CMS at sqrt(s)=7 TeV," 2011.

[28] G. D'Agostini, "A Multidimensional unfolding method based on Bayes' theorem," *Nucl. Instrum. Meth.*, vol. A362, pp. 487–498, 1995.

[29] G. D'Agostini, "Improved iterative Bayesian unfolding," 2010.

[30] T. Adye, "Unfolding algorithms and tests using RooUnfold," in *Proceedings, PHYSTAT 2011 Workshop on Statistical Issues Related to Discovery Claims in Search Experiments and Unfolding, CERN,Geneva, Switzerland 17-20 January 2011*, (Geneva), pp. 313–318, CERN, CERN, 2011.

[31] S. Chatrchyan *et al.*, "Measurement of the Inclusive Jet Cross Section in *pp* Collisions at $\sqrt{s} = 7$ TeV," *Phys. Rev. Lett.*, vol. 107, p. 132001, 2011.

[32] V. Khachatryan *et al.*, "Jet energy scale and resolution in the CMS experiment in pp collisions at 8 TeV," *JINST*, vol. 12, no. 02, p. P02014, 2017.

[33] C. Collaboration, "Jet energy scale uncertainty sources." https://twiki.cern.ch/twiki/bin/viewauth/CMS/JECUncertaintySources, 2012. (accessed on 2017-10-31).

[34] S. Chatrchyan *et al.*, "Measurements of differential jet cross sections in proton-proton collisions at $\sqrt{s} = 7$ TeV with the CMS detector," *Phys. Rev.*, vol. D87, no. 11, p. 112002, 2013. [Erratum: Phys. Rev.D87,no.11,119902(2013)].

[35] V. Khachatryan *et al.*, "Measurement and QCD analysis of double-differential inclusive jet cross sections in pp collisions at $\sqrt{s} = 8$ TeV and cross section ratios to 2.76 and 7 TeV," *JHEP*, vol. 03, p. 156, 2017.

[36] Z. Nagy, "Three jet cross-sections in hadron hadron collisions at next-to-leading order," *Phys. Rev. Lett.*, vol. 88, p. 122003, 2002.

[37] Z. Nagy, "Next-to-leading order calculation of three jet observables in hadron hadron collision," *Phys. Rev.*, vol. D68, p. 094002, 2003.

[38] T. Kluge, K. Rabbertz, and M. Wobisch, "FastNLO: Fast pQCD calculations for PDF fits," in *Deep inelastic scattering. Proceedings, 14th International Workshop, DIS 2006, Tsukuba, Japan, April 20-24, 2006*, pp. 483–486, 2006.

[39] D. Britzger, K. Rabbertz, F. Stober, and M. Wobisch, "New features in version 2 of the fastNLO project," in *Proceedings, 20th International Workshop on Deep-Inelastic Scattering and Related Subjects (DIS 2012): Bonn, Germany, March 26-30, 2012*, pp. 217–221, 2012.

[40] M. R. Whalley, D. Bourilkov, and R. C. Group, "The Les Houches accord PDFs (LHAPDF) and LHAGLUE," in *HERA and the LHC: A Workshop on the implications of HERA for LHC physics. Proceedings, Part B*, pp. 575–581, 2005.

[41] A. Buckley, J. Ferrando, S. Lloyd, K. Nordström, B. Page, M. Rüfenacht, M. Schönherr, and G. Watt, "LHAPDF6: parton density access in the LHC precision era," *Eur. Phys. J.*, vol. C75, p. 132, 2015.

[42] G. Aad *et al.*, "Measurement of the inclusive jet cross section in pp collisions at sqrt(s)=2.76 TeV and comparison to the inclusive jet cross section at sqrt(s)=7 TeV using the ATLAS detector," *Eur. Phys. J.*, vol. C73, no. 8, p. 2509, 2013.

[43] G. Aad *et al.*, "Measurement of the inclusive jet cross-section in proton-proton collisions at $\sqrt{s} = 7$ TeV using 4.5 fb^{-1} of data with the ATLAS detector," *JHEP*, vol. 02, p. 153, 2015. [Erratum: JHEP09,141(2015)].

[44] V. Khachatryan *et al.*, "Measurement of the inclusive 3-jet production differential cross section in proton–proton collisions at 7 TeV and determination of the strong coupling constant in the TeV range," *Eur. Phys. J.*, vol. C75, no. 5, p. 186, 2015.

[45] V. Khachatryan *et al.*, "Measurement of the inclusive jet cross section in pp collisions at $\sqrt{s} = 2.76\,\mathrm{TeV}$," *Eur. Phys. J.*, vol. C76, no. 5, p. 265, 2016.

[46] S. Alekhin, J. Blumlein, and S. Moch, "Parton Distribution Functions and Benchmark Cross Sections at NNLO," *Phys. Rev.*, vol. D86, p. 054009, 2012.

[47] H.-L. Lai, M. Guzzi, J. Huston, Z. Li, P. M. Nadolsky, J. Pumplin, and C. P. Yuan, "New parton distributions for collider physics," *Phys. Rev.*, vol. D82, p. 074024, 2010.

[48] A. D. Martin, W. J. Stirling, R. S. Thorne, and G. Watt, "Parton distributions for the LHC," *Eur. Phys. J.*, vol. C63, pp. 189–285, 2009.

[49] A. D. Martin, W. J. Stirling, R. S. Thorne, and G. Watt, "Uncertainties on alpha(S) in global PDF analyses and implications for predicted hadronic cross sections," *Eur. Phys. J.*, vol. C64, pp. 653–680, 2009.

[50] R. D. Ball *et al.*, "Parton distributions with LHC data," *Nucl. Phys.*, vol. B867, pp. 244–289, 2013.

[51] S. Dulat, T.-J. Hou, J. Gao, M. Guzzi, J. Huston, P. Nadolsky, J. Pumplin, C. Schmidt, D. Stump, and C. P. Yuan, "New parton distribution functions from a global analysis of quantum chromodynamics," *Phys. Rev.*, vol. D93, no. 3, p. 033006, 2016.

[52] H. Abramowicz *et al.*, "Combination of measurements of inclusive deep inelastic $e^{\pm}p$ scattering cross sections and QCD analysis of HERA data," *Eur. Phys. J.*, vol. C75, no. 12, p. 580, 2015.

[53] L. A. Harland-Lang, A. D. Martin, P. Motylinski, and R. S. Thorne, "Parton distributions in the LHC era: MMHT 2014 PDFs," *Eur. Phys. J.*, vol. C75, no. 5, p. 204, 2015.

[54] R. D. Ball *et al.*, "Parton distributions for the LHC Run II," *JHEP*, vol. 04, p. 040, 2015.

[55] M. Bahr *et al.*, "Herwig++ Physics and Manual," *Eur. Phys. J.*, vol. C58, pp. 639–707, 2008.

[56] P. Nason, "A New method for combining NLO QCD with shower Monte Carlo algorithms," *JHEP*, vol. 11, p. 040, 2004.

[57] S. Frixione, P. Nason, and C. Oleari, "Matching NLO QCD computations with Parton Shower simulations: the POWHEG method," *JHEP*, vol. 11, p. 070, 2007.

[58] S. Alioli, K. Hamilton, P. Nason, C. Oleari, and E. Re, "Jet pair production in POWHEG," *JHEP*, vol. 04, p. 081, 2011.

[59] V. Khachatryan *et al.*, "Event generator tunes obtained from underlying event and multiparton scattering measurements," *Eur. Phys. J.*, vol. C76, no. 3, p. 155, 2016.

[60] W. Hollik *et al.*, "Electroweak physics," *Acta Phys. Polon.*, vol. B35, pp. 2533–2555, 2004.

[61] S. Dittmaier, A. Huss, and C. Speckner, "Weak radiative corrections to dijet production at hadron colliders," *JHEP*, vol. 11, p. 095, 2012.

[62] J. Pumplin, D. R. Stump, J. Huston, H. L. Lai, P. M. Nadolsky, and W. K. Tung, "New generation of parton distributions with uncertainties from global QCD analysis," *JHEP*, vol. 07, p. 012, 2002.

[63] S. Chatrchyan *et al.*, "Determination of the top-quark pole mass and strong coupling constant from the t t-bar production cross section in pp collisions at $\sqrt{s} = 7$ TeV," *Phys. Lett.*, vol. B728, pp. 496–517, 2014. [Erratum: Phys. Lett.B738,526(2014)].

[64] V. Khachatryan *et al.*, "Constraints on parton distribution functions and extraction of the strong coupling constant from the inclusive jet cross section in pp collisions at $\sqrt{s} = 7$ TeV," *Eur. Phys. J.*, vol. C75, no. 6, p. 288, 2015.

[65] G. Aad *et al.*, "Measurement of transverse energy-energy correlations in multi-jet events in pp collisions at $\sqrt{s} = 7$ TeV using the ATLAS detector and determination of the strong coupling constant $\alpha_{\rm s}(m_Z)$," *Phys. Lett.*, vol. B750, pp. 427–447, 2015.

[66] V. M. Abazov *et al.*, "Determination of the strong coupling constant from the inclusive jet cross section in $p\bar{p}$ collisions at sqrt(s)=1.96 TeV," *Phys. Rev.*, vol. D80, p. 111107, 2009.

[67] V. M. Abazov *et al.*, “Measurement of angular correlations of jets at $\sqrt{s} = 1.96$ TeV and determination of the strong coupling at high momentum transfers,” *Phys. Lett.*, vol. B718, pp. 56–63, 2012.

[68] V. Andreev *et al.*, “Measurement of multijet production in *ep* collisions at high Q^2 and determination of the strong coupling α_s,” *Eur. Phys. J.*, vol. C75, no. 2, p. 65, 2015.

[69] V. Andreev *et al.*, “Measurement of Jet Production Cross Sections in Deep-inelastic ep Scattering at HERA,” *Eur. Phys. J.*, vol. C77, no. 4, p. 215, 2017.

[70] H. Abramowicz *et al.*, “Inclusive-jet photoproduction at HERA and determination of alphas,” *Nucl. Phys.*, vol. B864, pp. 1–37, 2012.

[71] T. Affolder *et al.*, “Measurement of the strong coupling constant from inclusive jet production at the Tevatron $\bar{p}p$ collider,” *Phys. Rev. Lett.*, vol. 88, p. 042001, 2002.

[72] R. D. Ball, L. Del Debbio, S. Forte, A. Guffanti, J. I. Latorre, J. Rojo, and M. Ubiali, “A first unbiased global NLO determination of parton distributions and their uncertainties,” *Nucl. Phys.*, vol. B838, pp. 136–206, 2010.

[73] K. G. Chetyrkin, J. H. Kuhn, and M. Steinhauser, “RunDec: A Mathematica package for running and decoupling of the strong coupling and quark masses,” *Comput. Phys. Commun.*, vol. 133, pp. 43–65, 2000.

[74] B. Schmidt and M. Steinhauser, “CRunDec: a C++ package for running and decoupling of the strong coupling and quark masses,” *Comput. Phys. Commun.*, vol. 183, pp. 1845–1848, 2012.

[75] C. Patrignani *et al.*, “Review of Particle Physics,” *Chin. Phys.*, vol. C40, no. 10, p. 100001, 2016.

Selected

Reprints